MASTERARBEIT

Titel der Masterarbeit

The Cretaceous glauconitic sandstones of Abu Tartur, Egypt

Verfasserin

Bakkalaurea Brigitte Pestitschek

angestrebter akademischer Grad

Master of Science (MSc)

Wien, 2010

Studienkennzahl lt. Studienblatt:	A 066 815
Studienrichtung lt. Studienblatt:	Erdwissenschaften
Betreuerin / Betreuer:	Ao. Univ.-Prof. Mag. Dr. Susanne Gier

Contents

List of figures

List of tables

Abstract

The Abu Tartur mine is located in the Western Desert of Egypt, 50 km west of El Kharga City. Geologically, the Abu Tartur plateau is built by a sequence of Upper Cretaceous (Campanian – Maastrichtian) phosphorites, black shales and glauconitic sandstones. The phosphate deposits are of great economic importance and have been mined since their discovery in 1967.

Outcrop sections were measured, sampled, sedimentologically characterized and described. One specific glauconite layer was investigated mineralogically and chemically in detail and compared to a subsurface sample from the mine.

Two depositional regimes can be interpreted based on sedimentary architecture and structures: 1) a deeper-water hemipelagic environment, where phosphorites and organic carbon-rich shales were deposited and 2) a shallower, prograding higher energy shelf environment with glauconite. From a sequence stratigraphic perspective 1) was deposited during the transgressive systems tract and the early highstand while 2) was deposited during the remaining highstand and a lowstand prograding wedge (Glenn & Arthur, 1990).

Petrographic and SEM investigations show that the glauconite grains are of autochthonous origin. XRF, EMPA and thin-section analyses show that the glauconite grains from the outcrop differ significantly in their chemical composition, morphology and color from the grains of the mine sample. The fresh glauconite are enriched in Fe_2O_3 and K_2O compared to the surface samples.

XRD analyses of the clay fraction of the six outcrop samples and the mine sample show that the grains consist of illite(glauconite)/smectite mixed-layers, with more illite layers (80 %) in the mine sample.

The charge distribution diagram muscovite-pyrophyllite-celadonite shows a clear trend from smectitic glauconite to illitic glauconite, the mine sample plots exactly in the field for glauconites.

All these features indicate that the surface samples are strongly altered by weathering and that glauconite progressively transforms into iron-rich illte/smectite mixed layers and then into smectites. For any chemical and mineralogical characterization of glauconites at surface, these weathering effects have to be taken into consideration.

Kurzfassung

Die Abu Tartur Mine befindet sich in der Western Desert, 50 km westlich der Stadt El Kharga in Ägypten. Geologisch wird das Abu Tartur Plateau hauptsächlich von oberkretazischen (Campan – Maastricht) Phosphoriten, welche wirtschaftlich genutzt werden, Schwarzschiefern und Glaukoniten aufgebaut. Die Phosphat-haltigen Ablagerungen sind von großem wirtschaftlichen Interesse und werden seit ihrer Entdeckung im Jahr 1967 genutzt.

Ein Profil der Sedimentabfolge wurde aufgenommen, sedimentologisch beschrieben, charakterisiert, und die einzelnen Schichten beprobt. Weiters wurde eine spezielle Glaukonitlage detailliert mineralogisch und chemisch untersucht und mit einer Glaukonitprobe aus der Mine verglichen.

Aufgrund der Sedimentabfolge konnten zwei Ablagerungsbereiche interpretiert werden: 1) ein hemipelagisches Environment im Tiefwasser, wo Phosphorite und an organischem Kohlenstoff-reiche Tone abgelagert wurden und 2) ein flacheres, höher energetisches Schelf-Environment mit der Ablagerung von Glaukoniten. Von einer sequenzstratigraphischen Perspektive: 1) wurde während eines Transgressiven Systemtrakts (TST) und eines frühen Hochstands (HST) abgelagert und 2) während des mittlerern und späten Meerespiegel-Hochstands und eines Niedrigstand progradierenden Fächers (Glenn & Arthur, 1990).

Petrologische und rasterelektronenmikroskopische Untersuchungen verdeutlichen die authochtone Bildung der Glaukonitkörner. Mittels Röntgendiffraktometrie (XRD), Mikrosondenmessungen und Dünnschliffanalysen wurden chemische, morphologische und farbliche Unterschiede der Oberflächenproben AT 31 bis AT 36 und der frischen Minenprobe festgestellt. Die frischen Glaukonitkörner der Minenprobe sind, verglichen mit den Oberflächenproben, reich an Fe_2O_3 und K_2O. Dies veranschaulicht, dass die Oberflächenproben starker Verwitterung ausgesetzt wurden. XRD Analysen der <2 µm Fraktionen der Proben zeigen, dass die Glaukonitkörner aus Illit (Glaukonit)/Smektit-Wechsellagerungsmineralen bestehen. In der Minenprobe ist der Anteil der Illitlagen im Wechsellagerungsmineral jedoch höher (80%) als in den Oberflächenproben (52%).

Das Ladungsdiagramm Muskovit-Pyrophyllit-Seladonit zeigt einen klaren Trend von smektitischem Glaukonit zu illitischem Glaukonit. Die Minenprobe plottet exakt im Glaukonitfeld.

Die Ergebnisse verdeutlichen, dass die Oberflächenproben durch die Verwitterung stark verändert sind. Glaukonit verändert sich durch die Verwitterung kontinuierlich von einem illitähnlichen Mineral zu einem Fe-reichen Illit/Smektit Wechsellagerungsmineral und schließlich zu Smektit.

Für alle chemischen und mineralogischen Untersuchungen an glaukonitischen Oberflächenproben müssen diese starken Verwitterungseffekte berücksichtigt werden.

1. Introduction

The Abu Tartur mine is located 650 km southwest of Cairo, Egypt, in the Western Desert (Figs. 1.1, 1.2) at 25°25´ north and 30°05´ east. The sediments in the mine are Upper Cretaceous (Campanian – Maastrichtian) phosphorites, black shales and glauconitic sandstones belonging to the widespread shallow-marine deposits of the Duwi Formation. This formation underlies the Lower Maastrichtian to Upper Paleocene Dakhla shale and overlies the Lower Campanian Quseir Formation. Lithologically, it consists of phosphate beds interbedded with black and gray claystone, sandstone, siltstone and glauconite beds (Sediek & Amer, 2001). The contact between the Duwi and Dakhla formations marks the Campanian-Maastrichtian boundary and is dated at about 71 Ma (Tantawy et al., 2001).

The Abu Tartur Plateau has attracted the attention of several geologists since the discovery of significant phosphate deposits in the Duwi Formation in 1967 (Sediek & Amer, 2001).

These Upper Cretaceous marine sediments have been of intense economic interest because of the phosphate-rich deposits of the Duwi Formation that form part of an extensive Middle Eastern - North African phosphate province (Tantawy et al., 2001). This province accounts for the greatest accumulation of marine phosphorites known, possibly in excess of 70 billion metric tons of phosphate rocks (Glenn & Arthur, 1990). The phosphate resources in Egypt alone have been estimated to exceed 3 billion metric tons (Notholt, 1985).
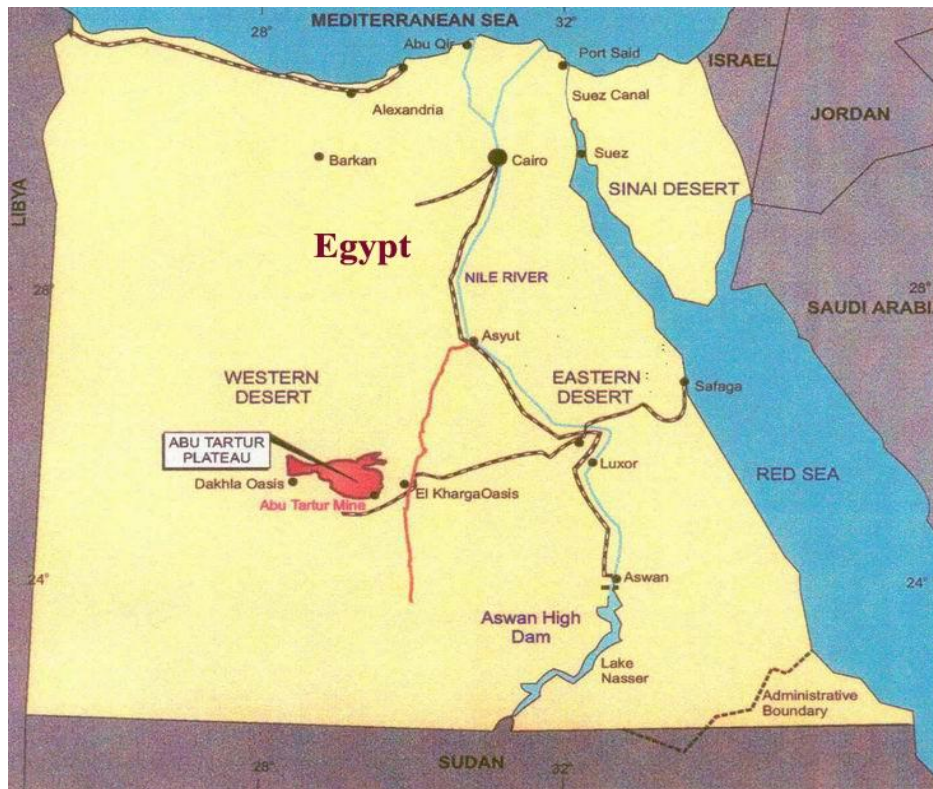
Fig. 1.1: Geographic map of Egypt, Abu Tartur Plateau is highlighted
(www.abutarturphosphate.gov.eg).

Fig. 1.2: Geographic map of Egypt (earth.google.com), Abu Tartur mine is indicated.
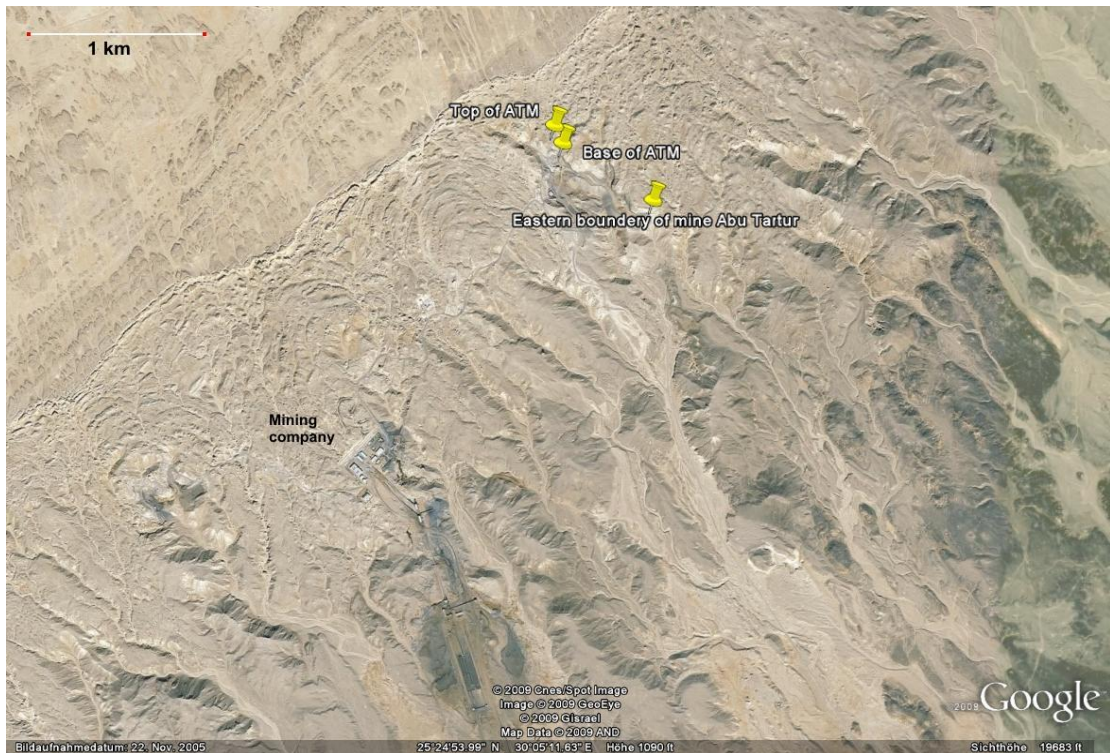
Fig. 1.3: The Abu Tartur mine, Egypt (earth.google.com), ATM= studied section.

The Abu Tartur phosphate project is considered to be one of the biggest mining projects in the world (Figs. 1.1,1.2 and 1.4)).

Fig. 1.4: The Abu Tartur mine, Egypt.

One of the main objectives of this study was to measure and sample a section for depositional environment analyses. Twenty-one samples of profile ATM (Figs. 1.3, 6.1

and 6.2)) including black shales, phosphorites, claystones and glauconitic sandstones, have been examined sedimentologically and geochemically. The results have been interpreted to characterize the depositional and diagenetic development of the complex sedimentary assemblages.

The other focus of this study was set on the mineralogical and geochemical composition and on the diagenesis of one specific glauconite layer. The outcrop glauconitic sandstones of the sedimentary layer and a glauconite subsurface sample from the mine were compared to determine possible differences in the diagenetic evolution and post-diagenetic effects.

The aim of this thesis is to reconstruct the depositional environment and physico-chemical conditions that prevailed on the Egyptian shelf during the Late Cretaceous in general and more specifically in the Abu Tartur area.

2. Geological setting

The Upper Cretaceous - Lower Tertiary sedimentary rocks in central and southern Egypt are characterized by a gradual facies differentiation into three main types: Nile Valley, Garra El-Arbain and Farafra. These facies are present in three different basins within the marginal trough on the northern flank of the African shield. The basins were delineated by exhumed pre-late Cretaceous undulating surfaces. The Nile valley facies extends from the Red Sea Coast in the east to Kharga Oasis in the west. The Garra-El Arbain facies is recorded in the area west and south of Aswan and also south of Kharga Oasis along Darb El-Arbain. The Farafra Oasis is in the heart of the Egyptian Western Desert, 300 km west of the Nile at Assiut. The Abu Tartur plateau is located in the Nile Valley facies (Issawi, 1972; Fig. 2.1).

GEOLOGICAL MAP OF EGYPT
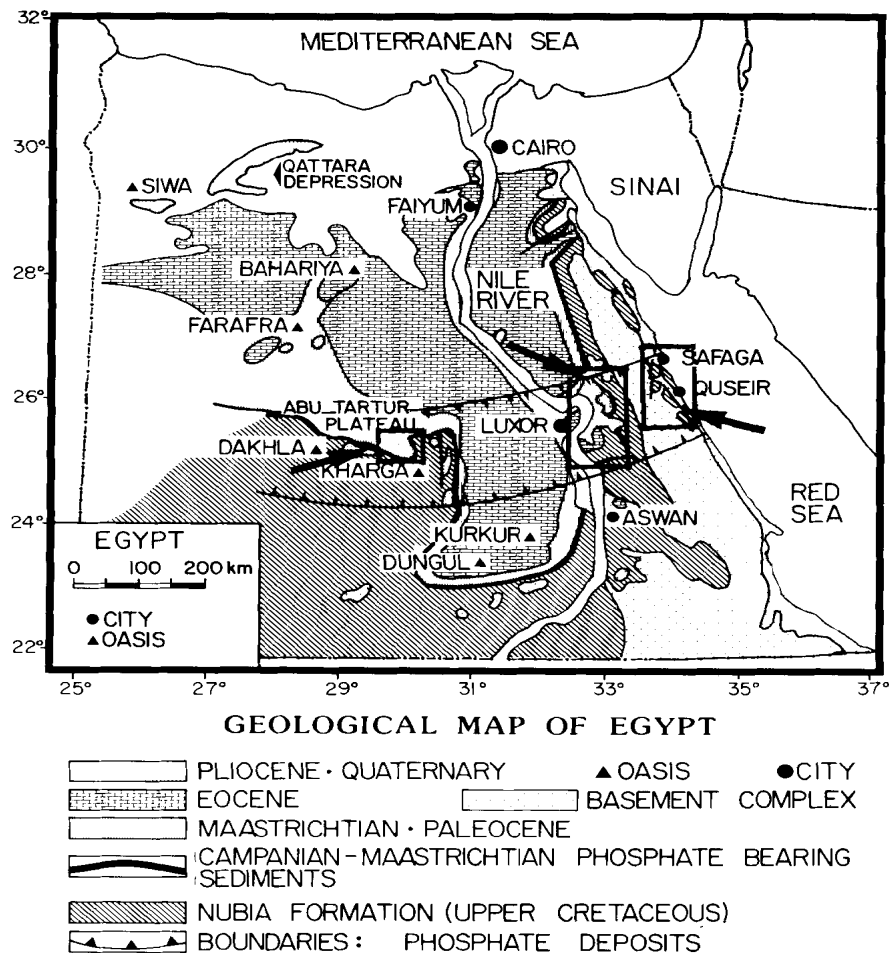
Fig. 2.1: Geological map of central Egypt and location of the Campanian - Maastrichtian sedimentary rocks, Glenn & Arthur (1990).

In the Eastern Desert the Upper Cretaceous - Lower Tertiary formations crop out on both sides of the crystalline basement ridge along the Red Sea. Towards the west, this sedimentary cover forms a plateau and joins the Western Desert Plateau across the Nile. These rocks extend from the Sudan-Egypt border (lat. 22-29°N). Several topographic depressions, prominent scarps and extensive plateaus are present. The Upper Cretaceous - Lower Tertiary rocks exposed along the Red Sea Coast in the east, Kharga Oasis in the west and in the Nile Valley have gross lithologic similarities which indicate deposition within one basin. The rocks of the Nile facies are differentiated into several units – from base to top - Nubia (Taref Sandstone and Variegated (=Quseir) Shale members), Duwi, Dakhla, Tarawan, Esna and Thebes formations (Issawi, 1972). These different units of the Nile facies of the Eastern Desert, Egypt are shown in Fig. 2.2.
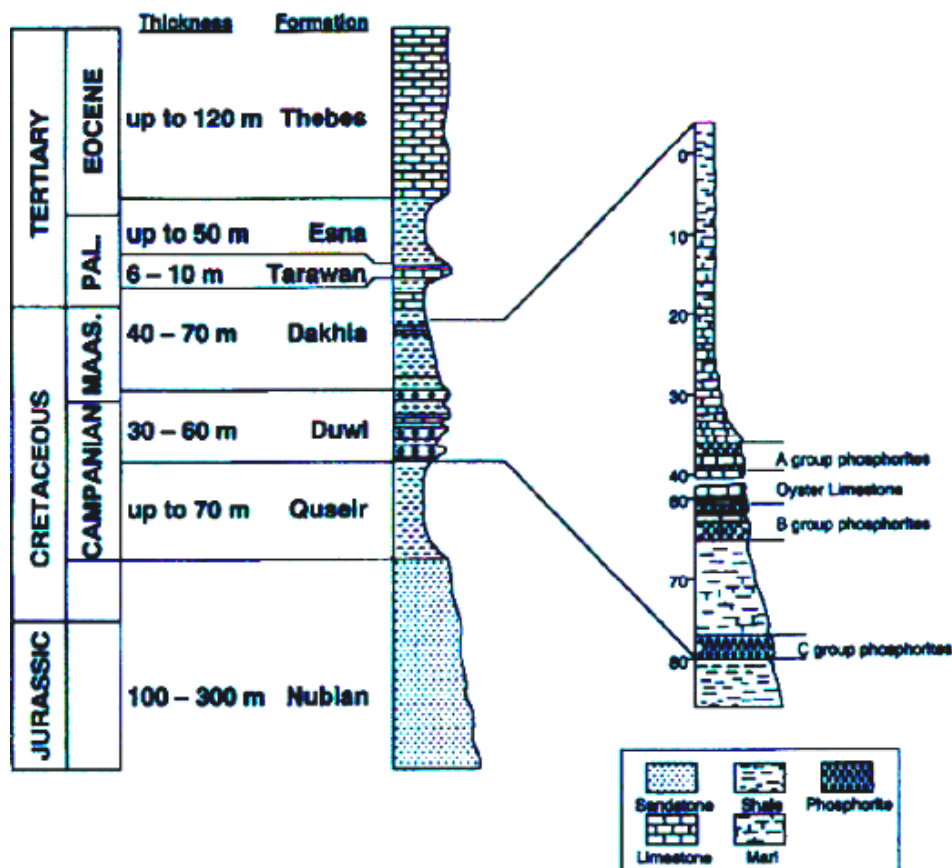
Fig. 2.2: Idealized stratigraphic section for the Eastern Desert of Egypt (Robinson & Engel, 1993).

The Western Desert sequence along the Abu Tartur plateau represents sediments that were confined by a pre-existing depression enclosed by the Dakhla (northwest) and Kharga (southeast) uplifts (Wassef, 1977; Van Houten et al., 1984).

The Kharga-Dakhla area (Fig. 1.1), which until the Late Maastrichtian, had the same facies prevailing in both Kharga and Dakhla Oases, seems to have developed in Landenian time a new facies similar to those of the Garra-El Arbain facies. The new facies, the Abu Tartur Formation, was caused by bulging of the area and the development of reefs. This is indicated by the major unconformity (Hermina, 1967) at the top of the Maastrichtian in contrast to the conformable relation between the Maastrichtian and the Paleocene in both Kharga Oasis (Awad and Ghobrial, 1965) and Dakhla Oasis (Hermina et al., 1961; Said, 1962).

The rocks of the Duwi Formation are of Late Campanian to earliest Maastrichtian age. The Duwi group represents the first onset of fully marine conditions in Egypt accompanying the major Late Cretaceous marine transgression of this region. With few exceptions these sediments were deposited in shallow epeiric seas which flanked the southern margin of the Tethyan trough. They were deposited in a generally east-west trending belt spanning the middle latitudes of Egypt (Glenn & Arthur, 1990).

The strata overlie Lower to Middle Campanian marginal marine to shallow-marine shales of the (Quseir) Variegated Shale Formation (also known as the Mut Formation; Said, 1962; Klitzsch et al., 1979; Ward & McDonald, 1979; Hendriks et al., 1984, Van Houten et al., 1984) and underlie deeper-water marine marls and chalks of the Maastrichtian Dakhla Formation (Said, 1962; Mansour & Khallaf, 1979; Mansour, Youssef & El Younsi, 1979; Hendriks et al., 1984; Soliman, Habib & Ahmed, 1986). A marked regional and local variation in the lithofacies of the Duwi Formation between the Red Sea, Nile Valley and Western Desert areas is noticed (Fig. 2.3).
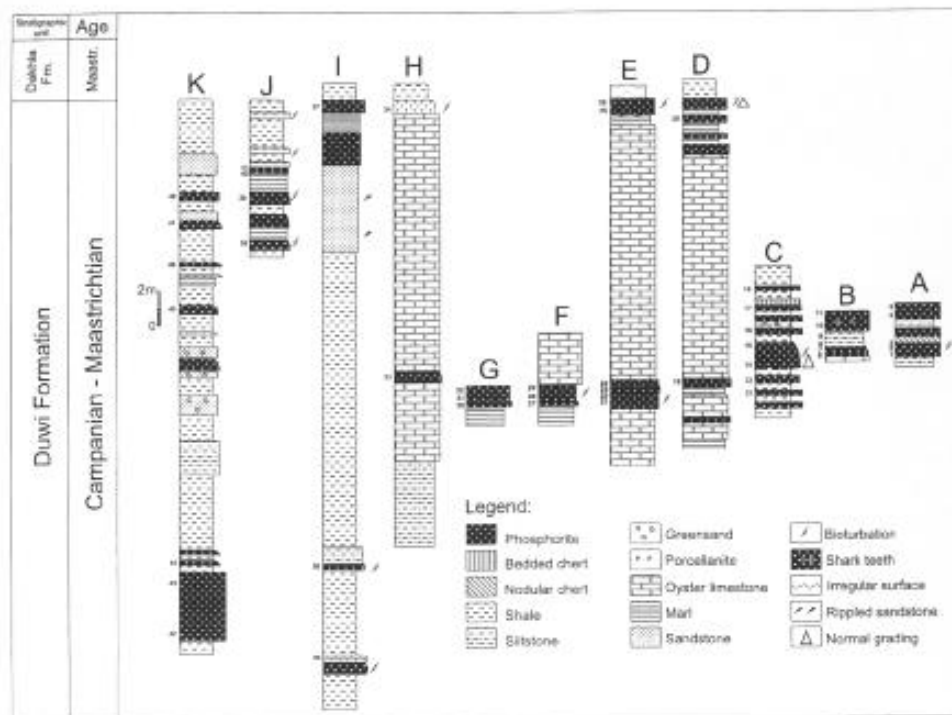
Fig. 2: Measured columnar sections.

Fig. 2.3: Measured sections of the Duwi Formation from Ahmed & Kurzweil, 2002. A – km 13 Safaga – Quena, B – Wadi Queh, C – north Yunis, D – Yunis, E – G. Anz (Galal Mine), F – Um Resifa, G – Zug El Bohar, H – Atshan, I – G. Qreiya, J – Abu Sabun, K – Abu Tartur.

2.1. Tectonic evolution

In the Late Triassic to Early Jurassic, the supercontinent Pangea began to break up with the initiation of opening of the Atlantic and Neotethys. By Cenomanian times, opening of the North and South Atlantic continued and the Neotethys began to close (Baudin, 1995).

From the Late Triassic to the Cenomanian North Africa was dominated by an extensional regime associated with the opening of the central Atlantic (Oyarzun et al., 1997). Around Cenomanian to Turonian times a general change from extension to compression occurred in North Africa, which was related to the closing of the Neotethys and the onset of North Atlantic rifting. This resulted in the inversion of the former rift grabens from the preceding extensional phase. 'Alpine' deformation intensified during

the Tertiary, leading to the formation of the Atlas Fold and Thrustbelt (Lüning et al., 2004).

During the Late Cretaceous, the structural differentiation of the Northeast African Plate increased, leading to the onset of the Red Sea rifting which caused the progressive uplift in the southern part of Egypt and a dextral strike-slip fault along the pre-existing ENE striking faults (Klitzsch, 1986).

Although tectonic activity contributed to erosion in the Western Desert, major eustatic sea-level changes may have been the primary controlling factors for widespread erosion and hiatuses (Tantawy et al., 2001).

2.2. Palaeogeography and Palaeoclimate

During the Late Cretaceous the African continent rotated counterclockwise and moved towards Asia, resulting in a gradual closing of the Neotethys (Condie, 1975; Le Pichon et al., 1976; Fig. 2.4). Also during this time a broad downwarping of the northeast margin of Africa occurred, causing a major transgression that covered portions of northeast Africa (Robinson & Engel, 1993).
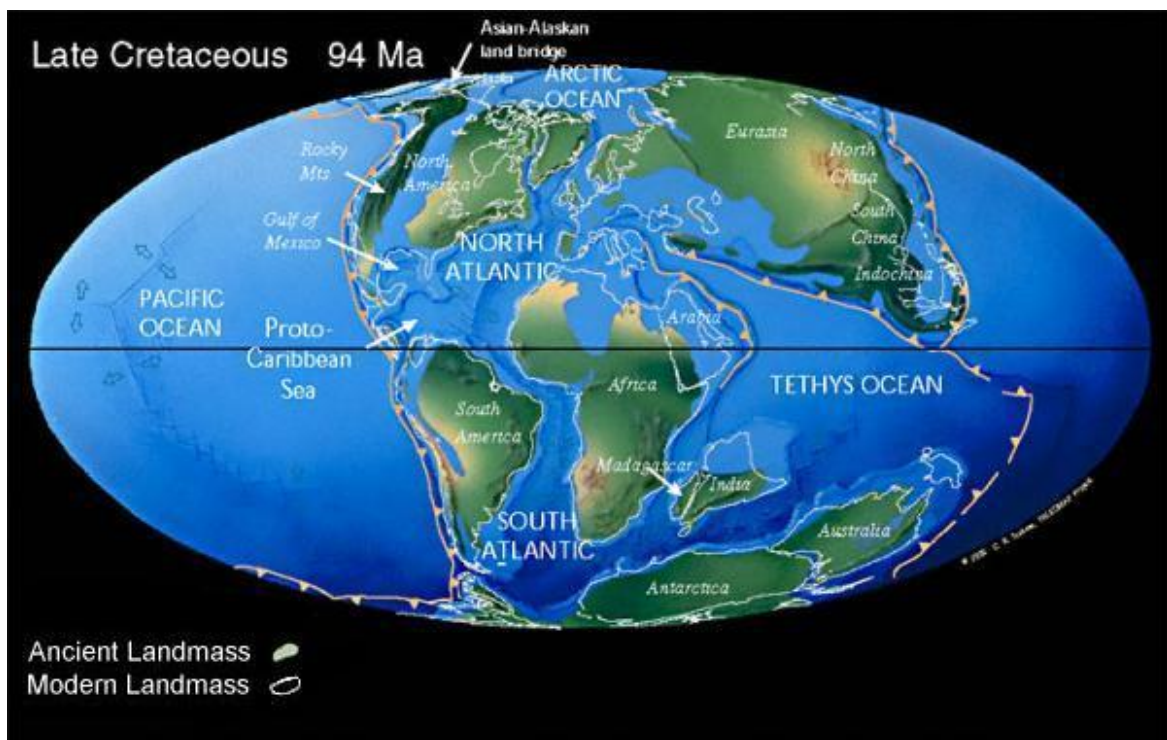
Fig. 2.4: Palaeogeography during the Late Cretaceous (www.scotese.com).

The transgression of the Tethys over Egypt in the Late Cretaceous started early in the Cenomanian. During the Campanian much of the country was covered by a generally shallow sea (Issawi, 1972). In central and southern Egypt a clastic-marine to continental section was deposited during the Campanian (Nakkady, 1951). During the Early Maastrichtian, favorable conditions for the deposition of phosphate beds of the Duwi Formation were present in the area extending from Quseir-Safaga on the Red Sea Coast to Dakhla Oasis in the far west. The end of the Maastrichtian is characterized by a regressive phase in most of Egypt (Issawi, 1972).

During the Late Cretaceous, Egypt was in a nearly equatorial position (Smith et al., 1982) (Fig. 2.4). The climate during the Campanian – Maastrichtian was very humid and warm, as confirmed by the palynology of the Dakhla Formation (Schrank, 1984).

The Upper Cretaceous - Lower Tertiary sediments of Egypt were deposited along the outer margin of the African shield (Klemme, 1958). Shallow-water sediments were deposited in the marginal trough close to the shield, but pass into deep-water sediments along the axis of the trough in northern Egypt. Structural movements shaped the configuration of the trough during different stages of the Late Cretaceous to Early Tertiary (Issawi, 1972).

Sediment deposition was predominantly cyclic, consisting of alternating sandstone/shale cycles with non-fossiliferous shales deposited during sea-level highstands in inner neritic to lagoonal environments characterized by euryhaline, dysaerobic or low oxygen conditions (Tantawy et al., 2001). The Campanian - Maastrichtian period is characterized by a series of marine anoxic phases associated with widespread organic matter, burial and black shale deposition (Schlanger & Jenkyns, 1976).

3. Samples

3.1. Macroscopic description of the glauconitic sandstones

In the following the six glauconitic sandstone samples AT 31 to AT 36 from layer 16 (Figs 3.1 and 3.2) and the mine sample are described macroscopically (Fig. 3.3 – Fig. 3.9):

Fig. 3.1: Profile ATM, layer 16.
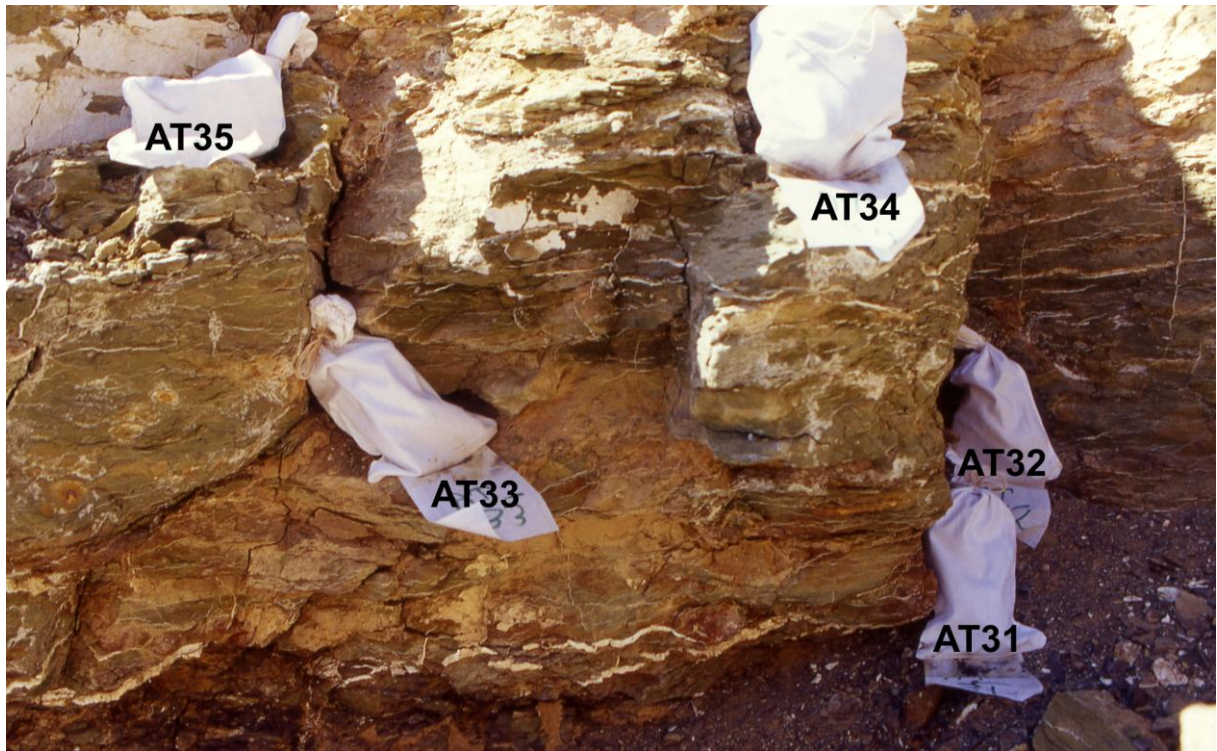
Fig. 3.2: Layer 16 with samples AT 31 to AT 35.

Sample AT 31 (Fig. 3.3) is a light greenish, medium-grained glauconitic sandstone. The sample shows reddish-brownish strongly weathered patches on the surface. There are thin fractures (1-2 mm) filled with gypsum and gypsum patches on the surface of the glauconite sample.

2cm
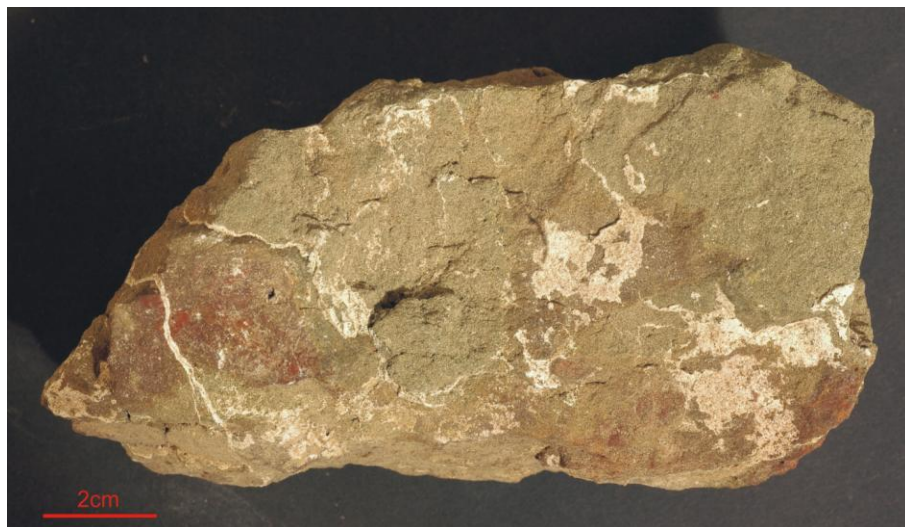
Fig. 3.3: AT 31, base of layer 16.

AT 32 (Fig. 3.4) is a light yellowish- greenish, medium-grained glauconitic sandstone. The glauconite sample contains gypsum-filled fractures.

Fig. 3.4: Sample AT 32.

Sample AT 33 (Fig. 3.5) is a greenish, medium-grained glauconitic sandstone with thin gypsum-filled fractures (mm- range).

Fig. 3.5: Sample AT 33.

AT 34 (Fig. 3.6) is a light greenish to greenish, medium-grained glauconitic sandstone with gypsum-filled fractures (mm- range).

Fig. 3.6: Sample AT 34.

AT 35 (Fig. 3.7) is a light greenish to greenish, medium-grained glauconitic sandstone with gypsum-filled fractures (mm- range) and patches of gypsum on the surface.
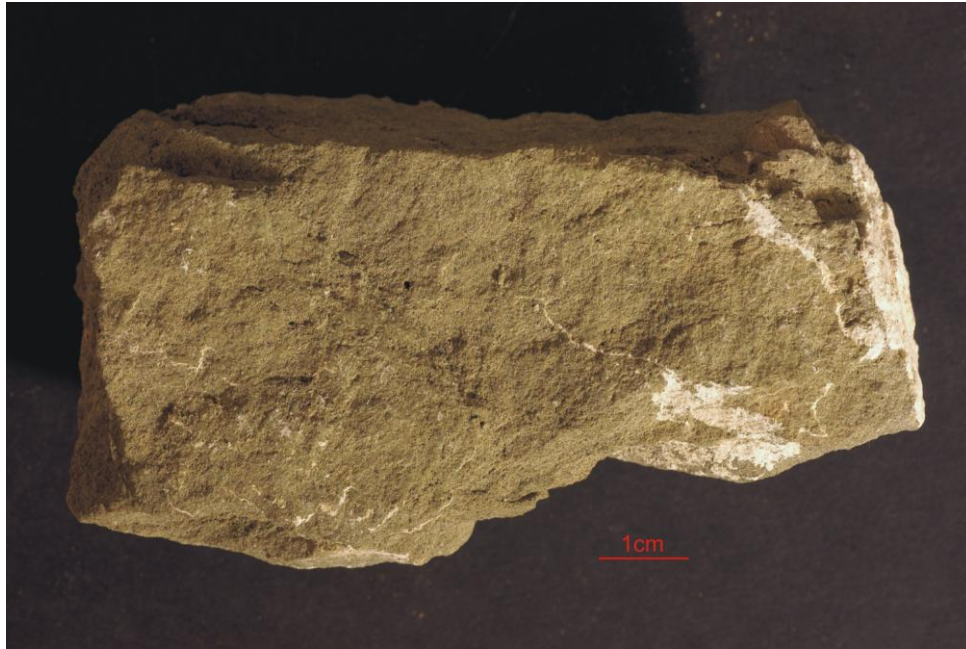
Fig. 3.7: Sample AT 35.

AT 36 (Fig. 3.8) is a greenish, medium- grained glauconitic sandstone with patches of gypsum on the surface.

Fig. 3.8: Sample AT 36, top of layer 16.

The mine sample (Fig. 3.9) is a bluish to dark greenish medium-grained glauconitic sandstone. The color is very intense and thin mudstone layers occur within the sample. The depth and the horizon of the sample are unknown.

Fig. 3.9: Mine sample (depth and horizon are unknown).

3.2. Samples from other layers of profile ATM

ATM 0: black shale

ATM 1: black shale with glauconite

ATM 2: glauconite with thin mudstone layers

ATM 3: glauconite

ATM 4: nodular glauconite

ATM 5: black shale

ATM 6: black shale with glauconite

ATM 10: black shale

ATM 11: coarse phosphorite

ATM 12: glauconite

ATM 14: claystone

4. Glauconitization and sedimentary environments

4.1. Glauconitization

According to Odin and Matter (1981), glauconites are mixed-layer minerals composed of smectite and glauconitic mica. They are potassium-rich dioctahedral phyllosilicates that generally appear in form of rounded grains.

- Glauconite or glauconitic mica represents an iron- and potassium-rich 10 Å illite-type mineral, with characteristics of evolved glauconite (Fe_2O_3 >20 %, K_2O >4 %). It predominates in Paleozoic glauconite peloids but also occurs in Mesozoic and Cenozoic grains.

- Glauconitic smectite forms a mixed-layered mineral group consisting of varying proportions of smectitic-, glauconitic- and sometimes illitic-type layers. It characterizes most of the Mesozoic and Cenozoic glauconite granules (Chamley, 1989).

Glauconite forms green pellets, either rounded or retaining the form of bioclasts: sponge spicules, foraminiferal shells, faecal pellets etc. It is a low-temperature dioctahedral mica that forms at the sediment-seawater interface and hardly grows after burial at shallow depth. As discussed in the literature, glauconite is of marine origin (Meunier, 2004). The glauconitic facies is widespread on present-day continental shelves from 50° S to 65° N and is in particularly abundant on the upper slope and outer shelf between 200 and 300 m water depth (Odin & Matter, 1981). But the green pellets also occur down to 500 m water depth, mostly on topographic heights characterized by little terrigenous supply, strong bottom currents and suitable substrates (microfossils, faecal pellets). Glauconite is especially abundant at the shelf-slope transition, where bottom currents prevent fast sedimentation by winnowing fine terrigenous particles. Most glauconite deposits correlate with hiatuses or very slow sedimentation rates (Chamley, 1989).

At water depths of more than 500 m, the green grains are usually interpreted as perigenic being transported downslope (Odin and Fullagar, 1988). Shallower than 60 m, glauconite is either absent or reworked from ancient rocks. The question of the possible formation of glauconite in deep- sea sediments is still hardly investigated.

Glauconite occurs in surface sediments deposited on continental shelves and topographic highs of all oceans except in the high northern and southern latitudes. The

glauconitization process is related to the chemical diffusion of the elements naturally in solution in water with those directly solubilised in the pore waters of the microenvironment (Meunier, 2004).

Planktonic and benthic marine organisms provide the organic matter whose presence is decisive element in determining the chemical properties at the microenvironment scale (<1 mm). Glauconite is formed by chemical exchanges between solid debris and seawater at the microsystem scale (Meunier, 2004).

The role of micro-organisms for the formation of glauconite must be taken into consideration. In this respect, it is worth mentioning that Geptner et al. (1994) and Geptner and Ivanovskaya (1998, 2000) reported the participation of bacteria in the glauconite formation in modern and ancient sediments.

The intensity and rapidity of glauconitization strongly depends on the nature and size of initial substrates (siliceous, biogenic etc.), (Giresse et al, 1980).

Glauconite deposits frequently correlate with transgressive sequences in the geologic record. Transgressive conditions favor extensive greening processes because shallower substrates become successively available, the sea-level rise causes a decrease in terrigenous input and prevents rapid burying that would stop the green clay development. The microenvironment, responsible for glauconite genesis, is unquestionably restricted and chemically concentrated since open-marine, especially shallow marine conditions do not significantly modify terrigenous minerals. The confined conditions necessary for chemical exchanges must not be too strong, since greening does not develop in chemically too closed systems (e.g. buried systems) and renewal of ions is necessary for granule growth (Chamley, 1989).

4.1.1. Genesis of glauconite

Three main mechanisms have been published to explain the formation of glauconite granules.

(1) The layer lattice theory (Burst, 1958a and b; Hower, 1961) is based on the transformation of a degraded 2:1 layer silicate lattice (TOT clay) into an iron- and potassium-rich 2:1 layer silicate of the illite group. This is supposed to occur under reducing conditions.

(2) The epigenetic substitution theory (Ehlmann et al., 1963) considers that glauconite layers form through solution of preexisting minerals, by adding ions present in sea water.

(3) The precipitation-dissolution-recrystallization theory (Odin, 1975; Odin & Matter, 1981; Ireland et al., 1983) involves successive processes leading to a true neo-formation, and therefore implies independence between the nature of substrate and the new iron-rich clay minerals.

Recent studies have confirmed the precipitation-dissolution-recrystallization theory (Chamley, 1989). Odin and Matter (1981) have published seven observations incompatible with the layer lattice theory.

The chemical evolution of green clay granules stops either after a long exposure at the sediment surface (10^5- 10^6 years) or after significant burial (Chamley, 1989).

Typical abundances for the major cations present in glauconite are summarized in Table 3.1.

Table 3.1: Chemical composition of glauconitic green grains (after Odin, 1988).

Oxide	Usual contents	Deviating results
SiO_2	47.5 to 50.0%	a few higher values indicate quartz admixture
Al_2O_3	3.5 to 11%	some values up to 15%
Fe_2O_3	19 to 25%	higher values when oxidized
MgO	2 to 5%	
K_2O	3 to 9%	lower values when substrate abundant

Low K_2O content in glauconitic material is also related to the composition of the parental glauconite mineral phase as well as to destabilization of glauconite (Hassan & El-Shall, 2004).

Glauconitic minerals have low Al/Fe ratios, high Fe^{3+}/Fe^{2+} ratios and high Fe/Mg ratios compared to other clay minerals with the same structure (Odin, 1988).

With progressive replacement of the initial substrates and subsequent evolution, the grains become increasingly green and have a higher specific gravity and magnetic susceptibility. According to scanning electron microscope observations, the evolution from nascent (smectitic) minerals to highly-evolved (micaceous) minerals takes place by a recrystallization process (Odin & Matter, 1981).

4.1.2. Environment of glauconitization

The presence of pores is essential for the genesis of glauconite. The formation requires sea-water introduced in the substrates. A restricted environment is necessary for the glauconitization process. Verdissement (glauconitization) requires a restricted microenvironment different from that in sea-water. A key factor in the glauconitization process is the presence of a semi-restricted microenvironment where ions may enter and leave, but where ion-exchange is not too fast. Ions come from sea-water, but also from interstitial fluids in the sediment and possibly from the substrate itself. Conditions with temperatures below 15°C and pH around 8 are favorable. The Eh conditions are at the oxidation-reduction boundary which allows iron to be mobilized as Fe^{2+} from the environment and stabilized mainly as Fe^{3+} in the crystal structure (Odin and Fullagar, 1988). Although generally containing Fe^{3+}-ions, glauconite is sometimes associated with pyrite because of the reducing properties of organic matter (Meunier, 2004). The general environment is to be open sea-water (Odin and Fullagar, 1988).

4.1.3. Habits of glauconite

The morphology of glauconite described in the literature is quite diverse. Cayeux (1916), Millot (1964) and Triplehorn (1966, 1967) tried to classify this heterogeneity.

Four main factors influence the habit of glauconite:

1) the presence of a prerequisite material which has undergone verdissement (=substrate)

2) the presence, origin and size of the pores in which the authigenic phases form

3) the size of the substrate

4) the stage of evolution of the glauconitized material

Two main categories of habit can be distinguished: a granular and a film habit (Odin & Fullagar, 1988).

Four main groups of granular habits have been proposed by Odin (1975) and Odin and Matter (1981):
- Internal moulds
- Faecal pellets
- Replacement of carbonate or silicate bioclasts
- Coating and replacement of mineral and rock grains

Two varieties of thin layer of green clay (film) have been observed in nature. A green film is often present on hardgrounds or on large carbonate bioclasts such as mollusc shells. The thickness of the green film is related to the extent of alteration (e.g. a few millimeters for silica-rich material and up to 1 cm or more for more reactive constituents, especially carbonates).

The second variety of the film habit occurs as extensive surfaces, often more than 1 km^2 in area. These surfaces are usually present in carbonate sediments.

There is a third possible variety of glauconitization which has sometimes been called diffuse habit. The glauconitic clay develops in decimeter or meter thick layers giving a green color to the entire formation (Odin & Fullagar, 1988).

The most common habit is the granular one. This is due to the fact that the green clay develops within a substrate which is usually granular itself. Glauconite apparently develops either by filling pores or by replacement of grains.

The common feature for all groups is a substrate within authigenic clay genesis is sheltered. The variety is caused by nature, size and stage of evolution of the substrate.

Not all substrates are equally favorable for glauconitization. The nature and size of the substrates appear to be interrelated with the observed stage of evolution in a given sediment (Odin, 1988).

Odin and Matter (1981) and Odin (1988) suggest that the mechanism of glauconitization consists of four successive stages (Fig. 4.1), which follow one another at the sediment-water interface if suitable conditions persist.
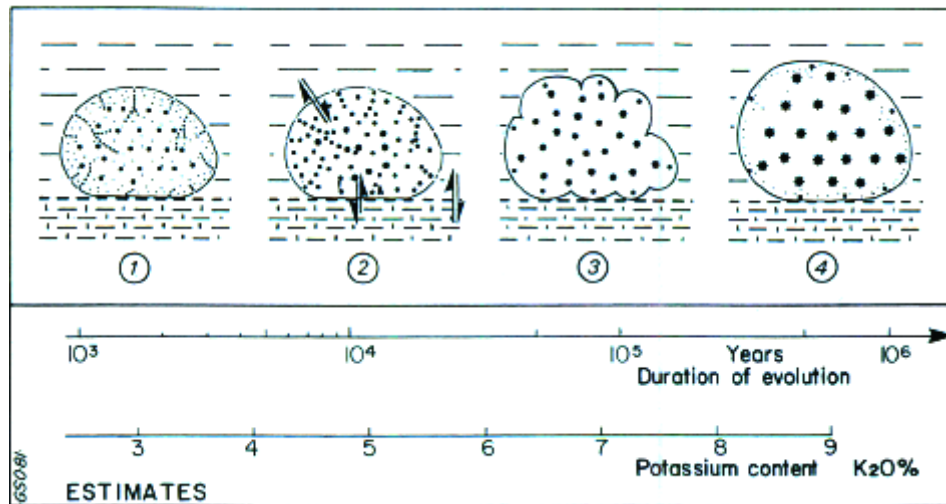
Fig. 4.1: Stages of evolution (Odin, 1988)

1. The nascent stage corresponds to the first development of iron-rich glauconitic minerals at the expense of detrital material. The K_2O content ranges between 2 and 4%. The first stage is strongly dependent on porosity that allows ion migration and chemical reactions.

2. The slightly evolved stage is characterized by the near disappearance of detrital minerals and the presence of pores that are progressively filled with authigenic clays containing between 4 and 6% K_2O.

3. The evolved stage results from a series of successive recrystallizations, tending to obliterate the initial structure. The clay growth occurs preferentially and more rapidly in the central zone of the grains, which causes an increase of the initial volume and the formation of cracks in the outer zone. The K_2O content ranges from 6 to 8%.

4. The highly evolved stage corresponds to the filling of cracks with authigenic minerals, producing smooth outlines. The K_2O content exceeds 8% of the total granule (Chamley, 1989).

Even if the general scheme presented above is correct at a given time, every point within a grain would not have reached the same stage of evolution. The mixture of different stages of evolution in a sediment is indicated by the light- and dark-green colors.

4.1.4. Post-genesis components of glauconite

Following genesis in contact with sea-water, early burial induces recrystallization resulting in a better crystallographical ordering of the clay structure. This evolution can be considered as part of the general process of glauconitization.

A type of alteration common on the present-day sea-bottom and also present in older sediments, results in the association of phosphate and glauconite. Although the general environment and the microenvironment of the paragenesis are different, there are many similarities (Odin and Létolle, 1980). Glauconitized phosphate and phosphatized glauconite are common. Both facies form during a hiatus in sedimentation. If the hiatus is long enough, some slight modification of the environment induces a change in the paragenesis (Odin and Fullagar, 1988).

4.1.5. Weathering of glauconite

In the first stages of weathering the external boundaries of these grains become fuzzy and a greenish alteroplasma forms. The latter becomes increasingly red as weathering intensifies. Electron microprobe analyses show that Fe and K contents gradually decrease in clay minerals. K is leached out from the rock by percolating waters while the Fe goes out of phyllosilicates to precipate as an independent phase (Fe-oxyhydroxides). Glauconite progressively transforms into iron-rich iliite/smectite mixed layers and then into smectites (Meunier, 2004).

The weathering sequence is opposite to that of the sediment glauconitization (Hower, 1961; Velde, 1976) indicating that the formation of glauconite is a reversible process at earth surface conditions (Meunier, 2004).

4.2. Sedimentary environments for the genesis of glauconite, phosphorites and black shales in Abu Tartur

Glauconite

Predominantly, glauconite evolves in open marine environment with a low terrigenous sedimentation rate. As mentioned before, glauconitization takes place at shallow water depth near the sediment-seawater interface (Porrenga, 1967).

The large quantity of the green grains suggests a high supply of K and detrital Fe in the micro-environment. After Ahmed and Kurzweil (2002), dissolution of diatoms led to the supersaturation of the pore water with silica, forming the glauconite of the Abu Tartur area. The diatom assemblages indicate restricted marine conditions.

According to Amorosi (1995), glauconite can occur in most depositional sequences but is generally most common in sediments of the transgressive system tract (TST) where it tends to show an upward increase in concentration and compositional maturity. The glauconite content decreases in the highstand system tract (HST) and is generally of low to moderate compositional maturity. In condensed sections very high concentrations of glauconite occur compared to the over- and underlying sediments. The relative sea level rise must have been rapid to promote the very low sedimentation rates conducive to glauconite formation (Amorosi, 1995).

Phosphorite

Phosphate is forming at the water-sediment interface within a confined microenvironment. To allow phosphate nodules growth, pore waters must be saturated with P and Ca and depleted in Mg. A weakly reducing environment provides the right conditions for phosphatization. The formation of glauconite depletes Mg from the sea floor environment and aids the precipitation of phosphate as nodules. Oceanic upwelling conditions, exhumation and burial coupled with alternating oxic to suboxic conditions is proposed as overall scenario (Marshall-Neill & Ruffell, 2004).

Black Shales

Sediek and Amer (2001) interpreted Abu Tartur black shales to be deposited under reducing conditions in a quiet (low energetic), alkaline marine setting.

According to Glenn and Arthur (1990) Western Desert shales exhibit lower C_{org} contents and HI values than Eastern Desert shales thus implying stronger terrigenous influence, sediment dilution and perhaps more oxidizing bottom conditions.

5. Methods

5.1. Measuring the profile ATM

During the field trip in March/April 2009 the profile ATM (Abu Tartur Middle) was measured, sampled and sedimentologically characterized. The profile lies in NE – SW direction in the Abu Tartur mine of Egypt. Thirty-six sediment layers were differentiated, beginning with massive black shales at the base and ending with light sandstones on top of the profile (Fig. 5.1).

Each layer was investigated macroscopically and described in detail. The lithology, grain size, color and thickness of each sedimentary sequence were determined.

Twenty samples were collected from different layers. The main interest was focused on six glauconitic sandstones samples of layer 16 (Fig. 5.1).

Fig. 5.1: Profile ATM, Abu Tartur mine.

5.2. Thin-section microscopy

To study the petrology of seven glauconitic sandstones (AT 31 – AT 36 and mine), thin-sections were prepared and investigated with a polarization microscope.

5.3. X-ray diffraction (XRD)

This method is applied to determine the qualitative and the semi-quantitative mineralogical composition. All measurements were made with a PANalytical X'Pert Pro diffratometer (CuKα- radiation (40kV, 40mA), step size 0.0167, 5 s per step) at the University of Vienna.

All 21 bulk samples were analyzed and the seven (AT 31 – AT 36 and mine) samples were additionally saturated with ethylenglycol and measured.

The <2 μm fraction from the six glauconitic sandstones samples and one black shale sample were investigated to determine the clay mineralogy. For the preparation, 8 mg of the fraction were dispersed in 1 ml of distilled water and applied on a small glass slide.

5.4. Clay mineral analysis

The clay fractions (<2 μm fraction) of six glauconitic sandstones and one black shale were obtained by sedimentation in Atterberg cylinders.

The samples were carefully crushed with a hammer to a grain size of approximately 1 mm. Then they were mixed with 15% H_2O_2 (hydrogen peroxide) for several days to remove all organic material. Afterwards, the samples were dispersed for 3 minutes with a 400W ultra-sonic stick. The suspensions were filled in Atterberg cylinders to separate the clay fractions. After the suspension achieved stability, Na-tripolyphosphat was added to prevent flocculation of the material.

The sedimentation time of 24 hours and 33 minutes was calculated using the formula of Stokes (1845). After this period, the <2 μm fraction is still in suspension. The suspension was drained and dried at 60 °C in an oven. After that, the < 2μm fraction was homogenized in an agate-mortar.

For Mg respectively K saturation, 50 mg of each sample were weighted in small plastic tubes and filled with $MgCl_2$- or KCl-solution (suspension 1mg/ml). After shaking over night, the suspensions were centrifuged and washed. Then they were applied on small glass slides, air dried and analyzed.

The Mg-saturated <2 µm samples were further saturated with glycerol (Gly) to differentiate between smectite and vermiculite. The potassium-saturated <2 µm samples were further saturated with ethylene-glycol (EG).

Additionally, the samples were heated to 550°C and analyzed.

5.5. X-ray fluorescence (XRF)

Wavelength-dispersive X-ray fluorescence spectrometry (WDXRF) is a non- destructive analytical technique used to identify and determine the concentrations of elements in samples. XRF is capable of measuring all elements from beryllium to uranium and beyond.

For preparation, the samples were ignited at 1050°C in an oven for 120 min to determine the LOI (Loss on Ignition). This is necessary, because volatile compounds like crystalline water, sulfur and chlorine are (partially) lost during the fusion process. Afterwards, 0.55 g of the powdered sample, 5.5 g flux (Spectromelt A12) and 800 mg ammonium bromide (to remove from the cup) were mixed together and melted in a Pt/Au crucible, producing a glass-like bead.

The beads were measured with an Axios – sequential high power X-ray fluorescence spectrometry (Dual-Multi-Channel-Analyzer, 20-60 kV, 10-100 mA). These analyses were carried out at the Technische Prüfanstalt (TPA) – Gesellschaft für Qualitätssicherung und Innovation GMBH.

5.6. Electron microprobe (EMP)

The quantitative chemical analyses of the glauconite grains were done with the microprobe CAMECA SX-100 (HV: 15 kV, IBeam: 20 nA), which is equipped with four wavelength-dispersive (WDX) and one energy-dispersive (EDX) spectrometer.

The thin-sections were coated with carbon before measuring.

5.7. Scanning electron microscope (SEM)

The scanning electron microscope was used to investigate the morphology and the surface of the glauconite grains. The images were made with LEO 1450 EP equipped with an energy dispersive X-ray spectrometer.

The cubic samples (about 1x1x1 cm) were coated with a film of gold, to attain conductivity on the surface and to avoid charging of the samples.

6. Results

6.1. Profile ATM

The section ATM consists of black shales, phosphorites, glauconitic sandstones and (sandy) claystone layers (Figs. 6.1, 6.2).
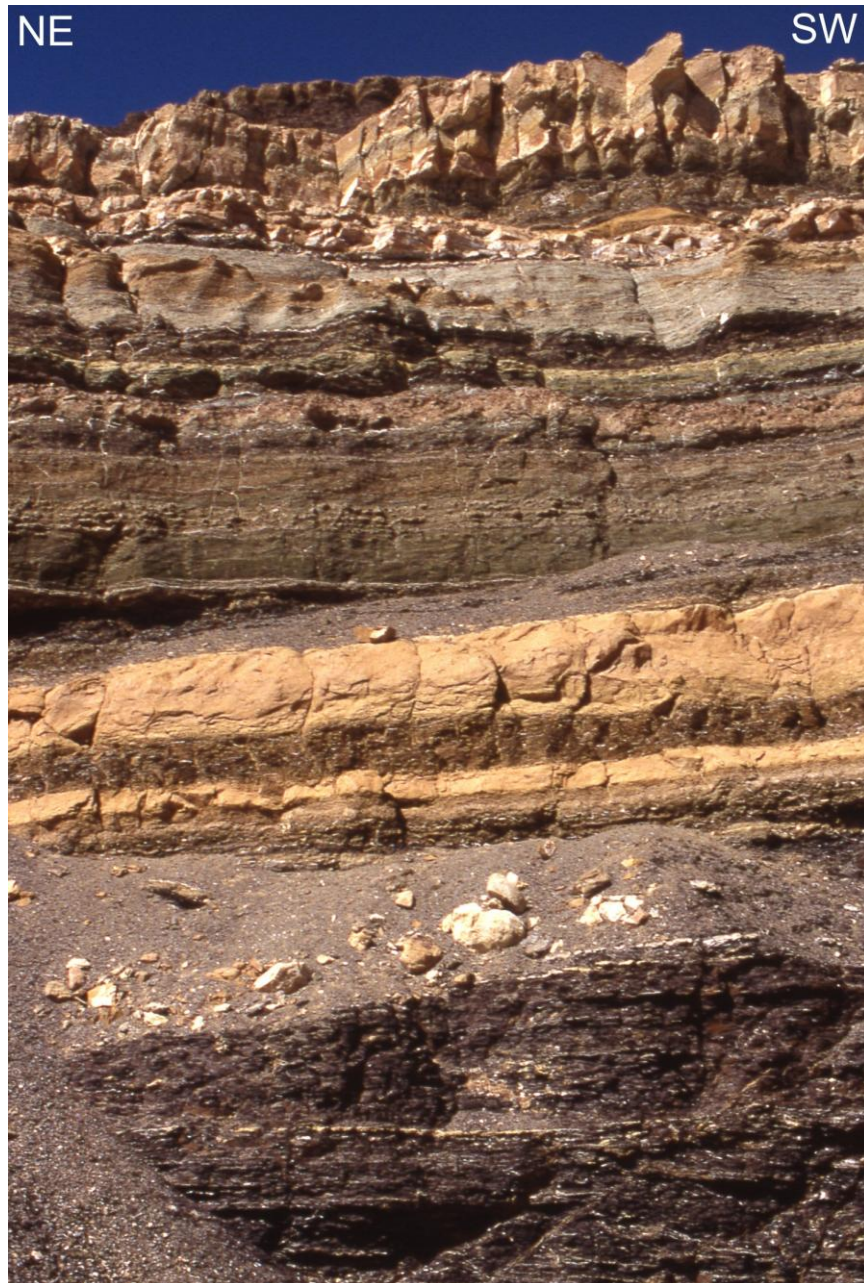
Fig. 6.1: Picture of profile ATM, for position see Fig. 1.3.

Profile ATM
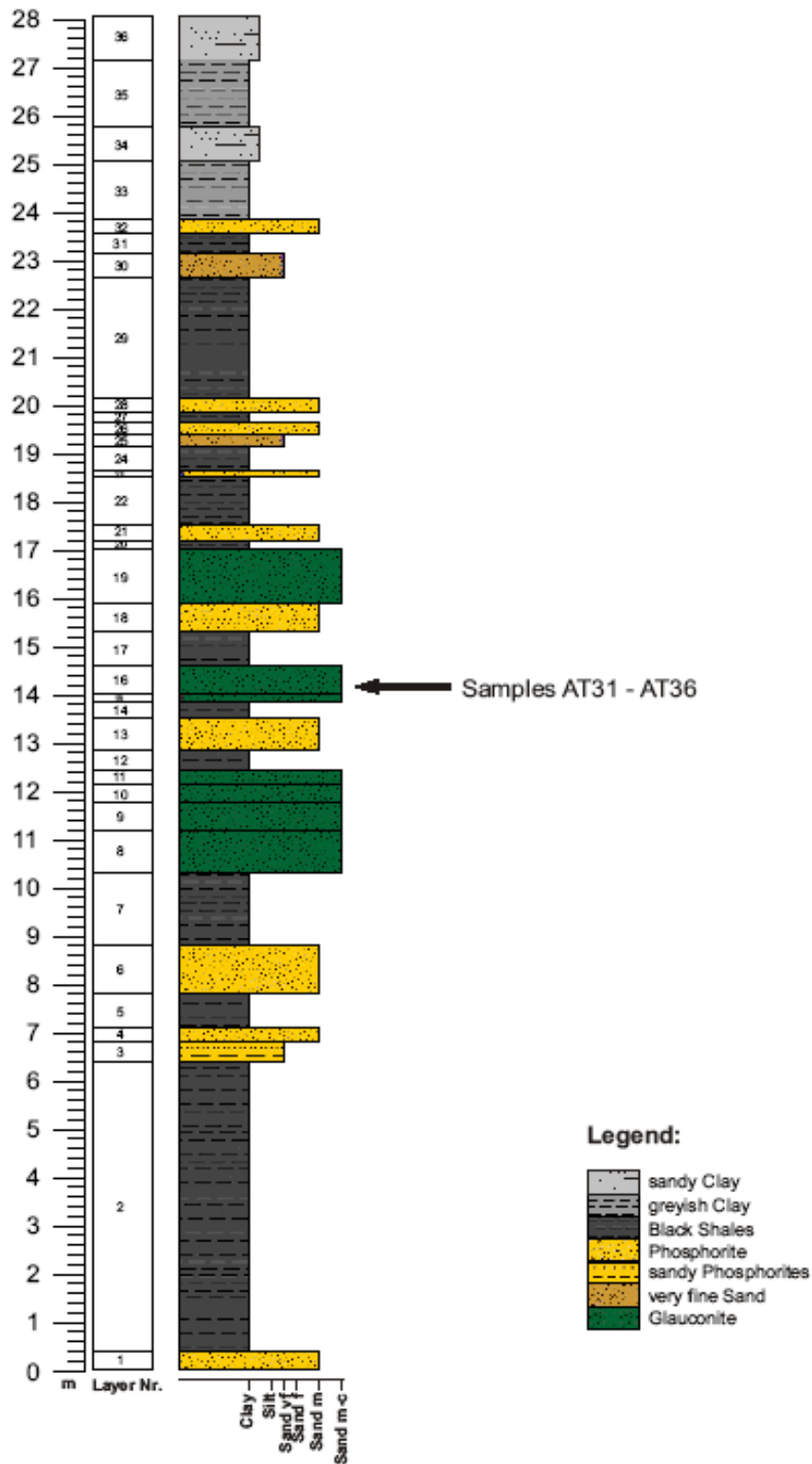
Fig. 6.2: Measured profile ATM

6.1.1. Description of profile ATM

Layer 36: 90 cm, fine sandy clay, sample: ATM 16

Layer 35: 140 cm, grayish clay, laminated, than massive, samples: ATM 14, ATM 15

Layer 34: 70 cm, fine sandy clay

Layer 33: 120 cm, grayish and greenish shales, gray – green - gray

Layer 32: 30 cm, phosphorites

Layer 31: 40 cm, black shales

Layer 30: 50 cm, very fine sand

Layer 29: 250 cm, black shales

Layer 28: 30 cm, phosphorites, coarse sand grain size

Layer 27: 20 cm, black shales

Layer 26: 25 cm, phosphorites with fine – coarse gravel, fine – medium-grained sand, slumping structure (1m), slumping: fine sand (silty, clayey)

Layer 25: 25 cm, sand, fine sand grain size, eventually rich of phosphorites

Layer 24: 50 cm, black shales

Layer 23: 15 cm, phosphorites, fine – medium-grained sand

Layer 22: 100 cm, black shales

Layer 21: 30 cm, phosphorites, fine – medium-grained sand

Layer 20: 20 cm, black shales

Layer 19: 110 cm, very massive glauconite, upward more clayey, first 10 cm less nodular with gravel, fining upward, fine – medium-grained sand, samples: ATM 12, ATM 13, ATM 13a

Layer 18: 60 cm, coarse phosphorites, transition zone to layer 17: lower 10 cm more greenish, different cement, high amount of gypsum in lower phosphorites, fine sand grain size, sample: ATM 11

Layer 17: 70 cm, black shales with nodular glauconite, sample: ATM 10

Layer 16: 60 cm, massive glauconite, medium-grained sand, sample: ATM 8, ATM 9 and AT 31-37

Layer 15: 15 cm, base of glauconite layer, fining upward, fine – medium-grained sand

Layer 14: 35 cm, black shales, transition zone to layer 15 green - black

Layer 13: 65 cm, sandy phosphorites, more nodular than lower phosphorites, sample: ATM 7

Layer 12: 40 cm, black shales, top with up to 5 cm big nodular glauconite, samples: ATM 5, ATM 6, ATM 6a

Layer 11: 30 cm, nodular glauconitic sandstone, sample: ATM 4

Layer 10: 40 cm, glauconitic sandstone, sample: ATM 3

Layer 9: 55 cm, glauconitic sandstone with sand – silt nodules (around 5 cm), well rounded → transported

Layer 8: 90 cm, glauconitic sandstone with mudstone layers (around 5 mm), laminated without nodules, sample: ATM 2

Layer 7: 150 cm, black shales

Layer 6: 100 cm, phosphorites, reddish – yellowish, sample: ATM 1

Layer 5: 70 cm, black shales

Layer 4: 30 cm, phosphorites, fine – medium-grained sand

Layer 3: 40 cm, transition zone: sandy phosphorites + black shales

Layer 2: minimum 600 cm, black shales, sample: ATM 0

Layer 1: 400 cm, phosphorites, fine – medium-grained sand (milled)

6.2. Petrology of the glauconitic sandstones

6.2.1. Description of thin-sections AT 31 to AT 36 and mine

The samples AT 31 to AT 36 (Fig. 6.3) and the mine sample can be classified as glauconitic wackes to glauconitic sandstones. Framework grains are predominantely glauconite grains and trace amounts of fine grained quartz grains. Glauconite grains range in grain size from 100 µm to 500 µm. In general, the grains smaller than about 100 µm in diameter are less evolved than larger ones. All sandstone samples are well to moderately sorted, well-rounded and grain supported. The grains show point-, long-, and concavo-convex contacts. The main glauconite morphologies are ovoidal, spheroidal or lobate.

Glauconite has an intense green or brownish-green color in plane polarized light (PPL), the grains are aggregates of many small crystals. Glauconite has a moderate birefringence, but interference colors are difficult to observe because they are masked by the intense natural color of the mineral.

The framework grains are engulfed in a brownish to reddish argillaceous matrix. Both, the glauconite grains and the matrix are cut by small, gypsum cemented fractures. The glauconite grains are partially weathered (maybe in some cases chloritized).
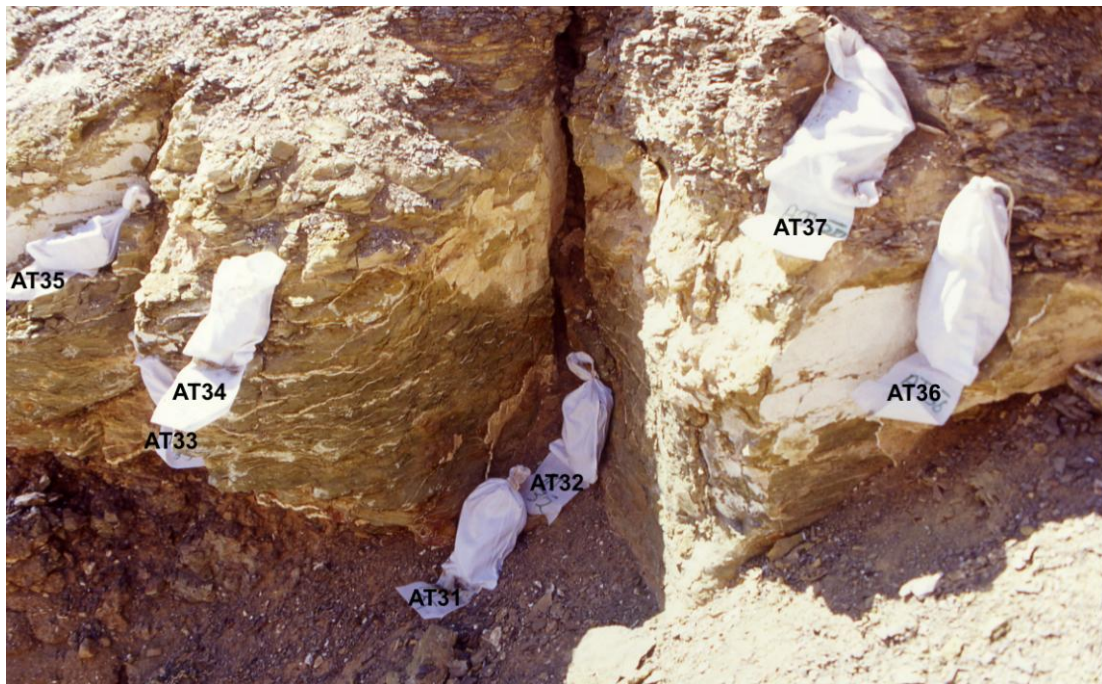
Fig. 6.3: Samples AT 31 (base) to sample AT 36 (top) from glauconite layer 16.

Sample: AT 31

Position: Base of layer 16, Fig. 6.3

Description of glauconite grains:

Glauconite grains are mainly between 100 µm and 300 µm in diameter. Subordinately, grains up to 600 µm in diameter are observed. The brownish-green to (a few) dark green pellets show different stages of evolution (Fig. 6.5). Generally, coarse grains show cracks in the outermost zone. A few dark green grains are cracked to the centre. The centre, intermediate and outermost zone of the grains show differences in color. The grains show point-, long-, and concavo-convex contacts. There are fractures filled with gypsum cement which cut through the grains and the groundmass (Fig. 6.4).

Stage of evolution (After Odin, 1988):

The potassium content of seven glauconite grains analyzed with EMP is between 5.32% and 6.91% therefore the stage of evolution is slightly-evolved to evolved.

Description of matrix:

Reddish-brown to dark brown clayey matrix.

Fig. 6.4: Picture of thin-section AT 31 showing green glauconite grains and with gypsum cemented fracture, cross polarized light (XPL).
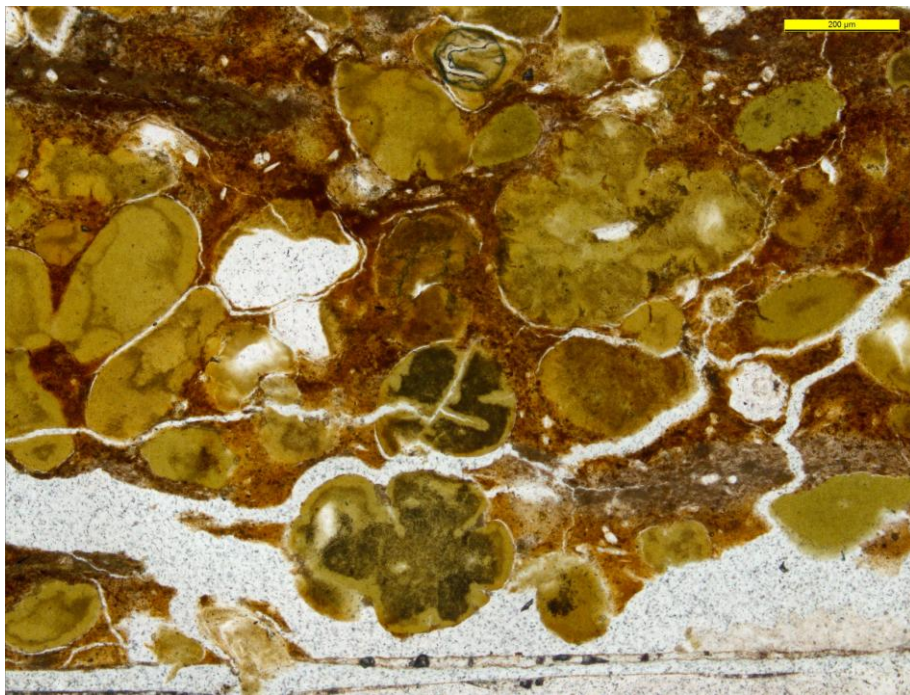
Fig. 6.5: Thin-section picture of sample AT 31 showing different stages of evolution of glauconite grains, plane polarized light (PPL).

Sample: AT 32

Position: Layer 16, Fig. 6.3

Description of glauconite grains:
The grains are pale green to brown in color. The sample is mainly grain supported, with some matrix supported areas (burrows?). The grains show differences in color in the centre, intermediate- and outermost zone. This observation is not grain size dependent. Glauconite grains also show shrinkage structures, because during evolution the grains undergo an increase and later shrinkage of the initial volume (Chamley, 1989; Fig. 6.7). The grains show point-, long-, and concavo-convex contacts.

Stage of evolution (After Odin, 1988):
The potassium content of seven glauconite grains measured with EMP is between 5.31% and 6.30% therefore the stage of evolution is slightly-evolved to evolved*.*

Description of matrix:
Brown to dark-brown clayey matrix (Fig. 6.6).
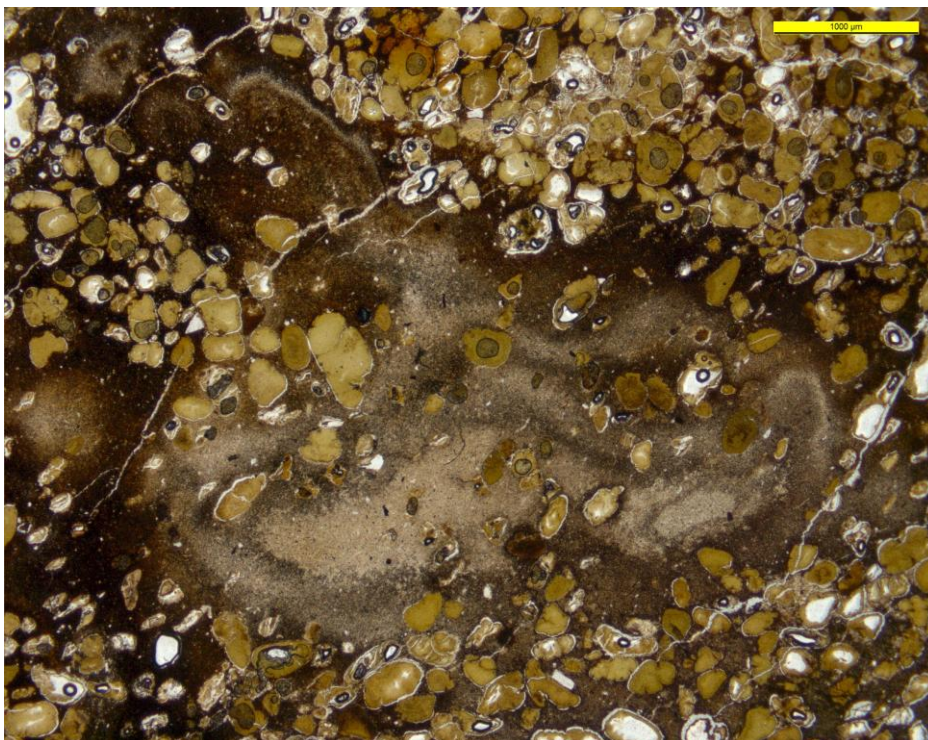
Fig. 6.6: Thin-section picture of sample AT 32 showing light green and brownish pellets in an argillaceous matrix (burrow?), (PPL).
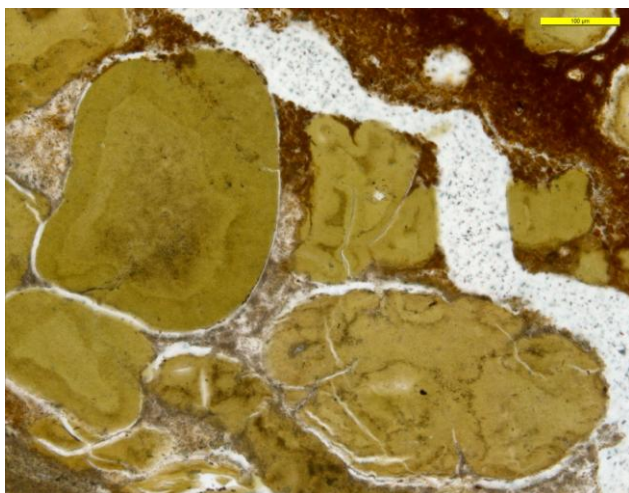
Fig. 6.7: Thin-section picture of sample AT 32 showing a fracture, shrinkage structures and differences in color of the pellets (PPL).

Sample: AT 33

Position: Layer 16, Fig. 6.3

Description of glauconite grains:

AT 33 shows light green and brownish, weathered glauconite grains. The sample is grain supported with long- and concavo-convex contacts (Fig. 6.8, Fig. 6.9). This sample is more compacted compared to samples AT 31 and AT 32 and has less matrix between the glauconite grains.

Stage of evolution (After Odin, 1988):

The potassium content of seven glauconite grains measured with EMP is between 5.01% and 6.55% therefore the stage of evolution is slightly-evolved to evolved.

Description of matrix:

Brown to dark-brown clayey matrix
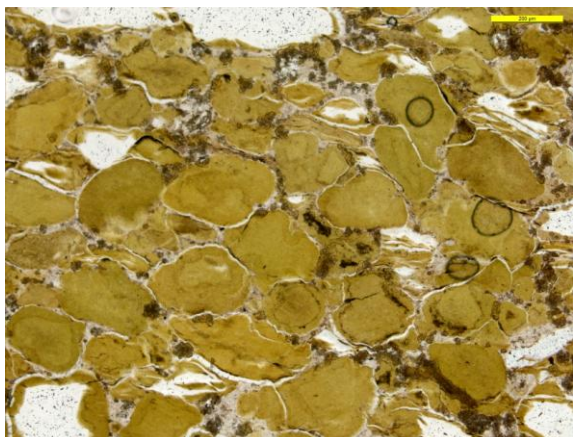
Fig. 6.8: Thin-section picture of sample AT 33 showing grain supported, compacted glauconite sandstone (PPL).

Fig. 6.9: Thin-section picture of sample AT 33 showing long contacts between the glauconite grains and a gypsum cemented fracture (PPL).

Sample: AT 34

Position: Layer 16, Fig. 6.3

Description of glauconite grains:

Thin-section picture AT 34 shows medium-grained glauconites. The sample is grain supported and the grains exhibit shrinkage structures and cracks up to the centre of the grain (Fig. 6.10). They are mostly dark green to (dark) brown in the centre and light green in the marginal zone. The clay growth occurs preferentially and more rapidly in the central zone of the grains, which causes an increase of the initial volume and the formation of cracks in the outer zone (Chamley, 1989, Fig. 6.11). The glauconites show point-, long- and concavo-convex contacts.

Stage of evolution (After Odin, 1988):

The potassium content of seven glauconite grains measured with EMP is between 4.18% and 5.22% therefore the stage of evolution is slightly-evolved.

Description of matrix:

Brown to dark-brown clayey matrix
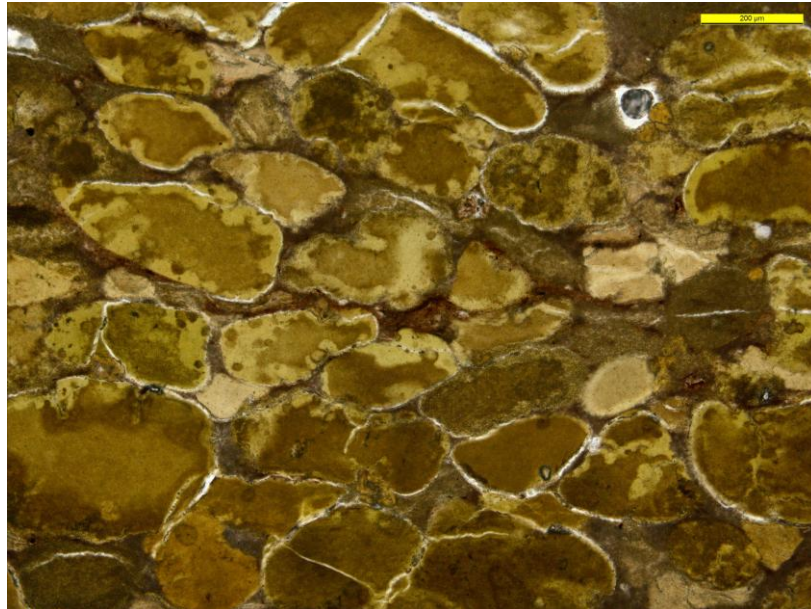
Fig. 6.10: Thin-section picture of sample AT 34 showing glauconite grains with dark-green to brown clayey central zones and shrinkage structures (PPL).
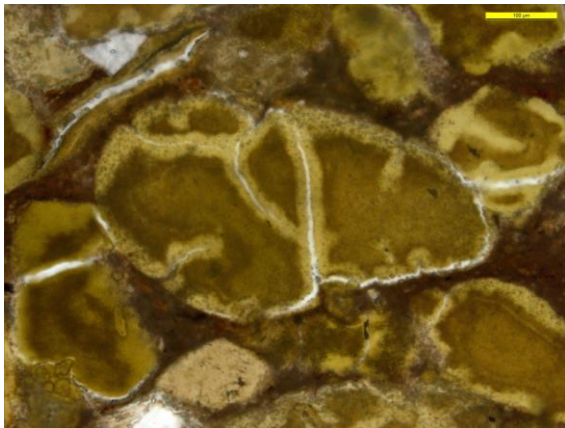
Fig. 6.11: Thin-section picture of sample AT 34 showing deep cracks cutting through the entire grain. The outermost zone of the grain shows a much lighter color than the centre (PPL).

Sample: AT 35

Position: Layer 16, Fig. 6.3

Description of glauconite grains:

Thin-section AT 35 shows greenish to brownish medium-grained glauconites (Fig. 6.12, Fig. 6.13). The grains are more compacted and oriented than in the other samples. AT 35 is grain supported and the grains are well-sorted and well-rounded. Some of the darker grains show zonal differences in color (Fig. 6.14).

Stage of evolution (After Odin, 1988):

The potassium content of seven glauconite grains measured with EMP is between 3.90% and 5.20% therefore the stage of evolution is slightly-evolved.

Description of matrix:

Brown to dark-brown clayey matrix (Fig. 6.13)
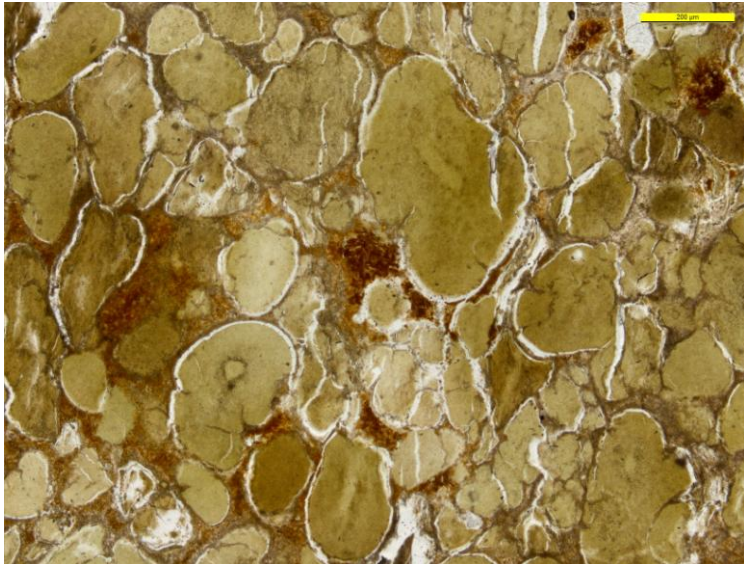
Fig. 6.12: Thin-section picture of sample AT 35 showing medium-grained, lobate glauconite grains. The glauconites show long-, point- and concavo-convex contacts (PPL).
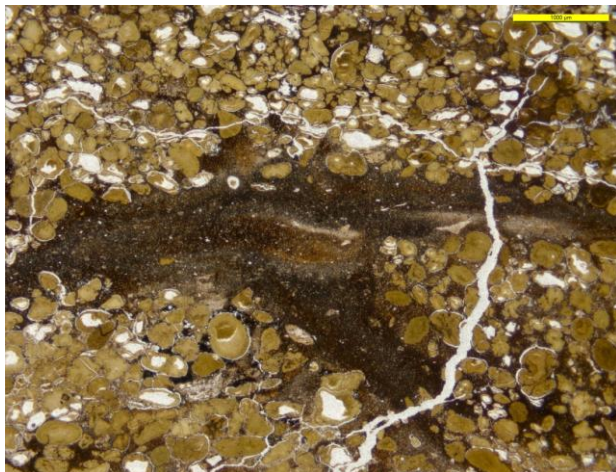
Fig. 6.13: Thin-section picture of sample AT 35 showing fractures cutting through grains and clayey ground-mass. Patch of clayey ground mass in centre of picture may originate from bioturbation (PPL).
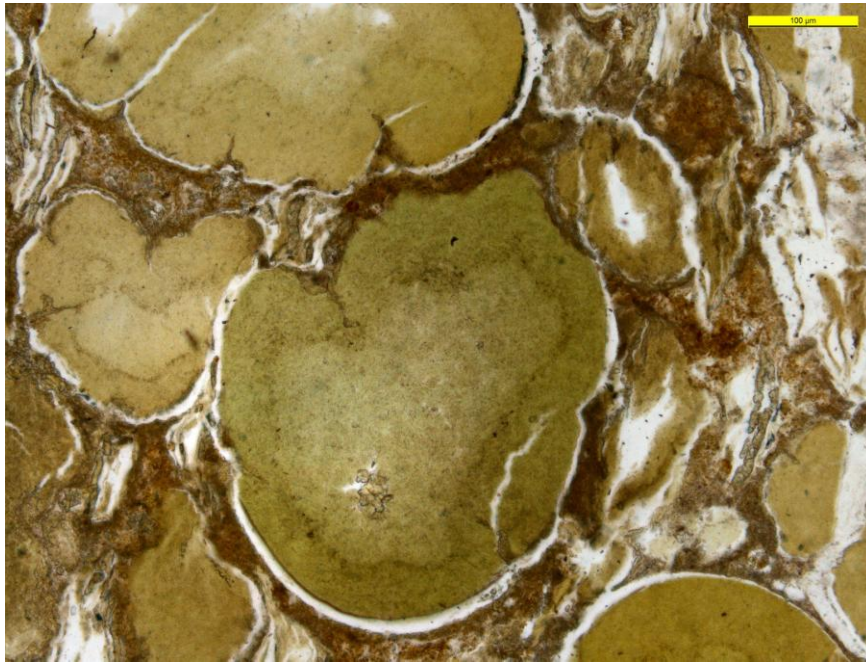
Fig. 6.14: Thin-section picture of sample AT 35 showing that the glauconite exhibit cracks, a light centre, dark green intermediate and green outermost zone (PPL).

Sample: AT 36

Position: Layer 16, Fig. 6.3

Description of glauconite grains:

AT 36 shows pale brown, brown and green glauconite grains. They are between 100 µm and 600 µm in diameter. Some grains show cracks in the outer zone (Fig. 6.15) and some are completely cut by cracks (Fig. 5.16). The grains are lighter in color compared with samples AT 31 to AT 35. The glauconite grains are irregular in shape.

Stage of evolution (After Odin, 1988):

The potassium content of seven glauconite grains measured with EMP is between 1.70% and 5.10% therefore the stage of evolution is nascent to slightly evolved.

Description of matrix:

Dark-brown clayey matrix.
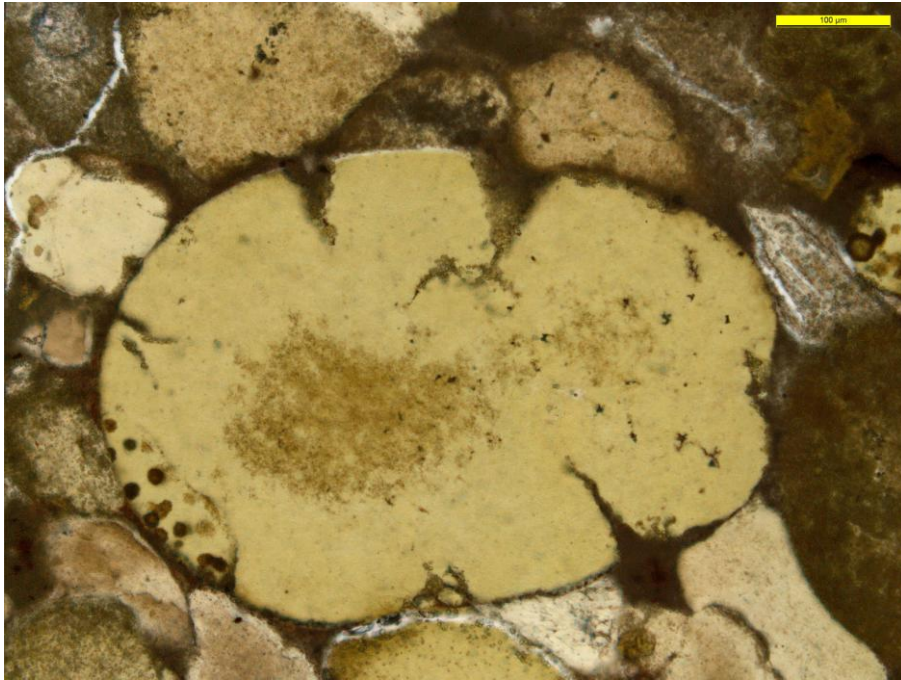
Fig. 6.15: Thin-section picture of sample AT 36 showing a glauconite grain with cracks in the outer zone (PPL).

Fig. 6.16: Thin-section picture of sample AT 36 showing pale brownish to brownish glauconite grains with cracks (PPL).

Sample: mine

Position:

Depth and horizon are unknown. The sample was chosen to study fresh, unweathered glauconites and compare them with surface samples from layer 16.

Description of glauconite grains:

The mine sample contains light to dark green and brown glauconite grains (Fig. 6.17). They are between 100 µm and 400 µm in diameter. The grains are well rounded, well sorted and show concavo-convex- and long-contacts. The thin-section shows a grain-supported glauconite sandstone (Fig. 6.18 and Fig. 6.19). The grains are compacted and show specific orientation (Fig. 6.17). Cracked glauconite grains occur subordinately. Zonated grains show a thin rim of lighter color (Fig. 6.20 and Fig. 6.21).

Stage of evolution (After Odin, 1988):

The potassium content of seven glauconite grains measured with EMP is between 5.36% and 7.24% therefore the stage of evolution is slightly-evolved to evolved.

Description of matrix:

Green to brown clayey matrix.

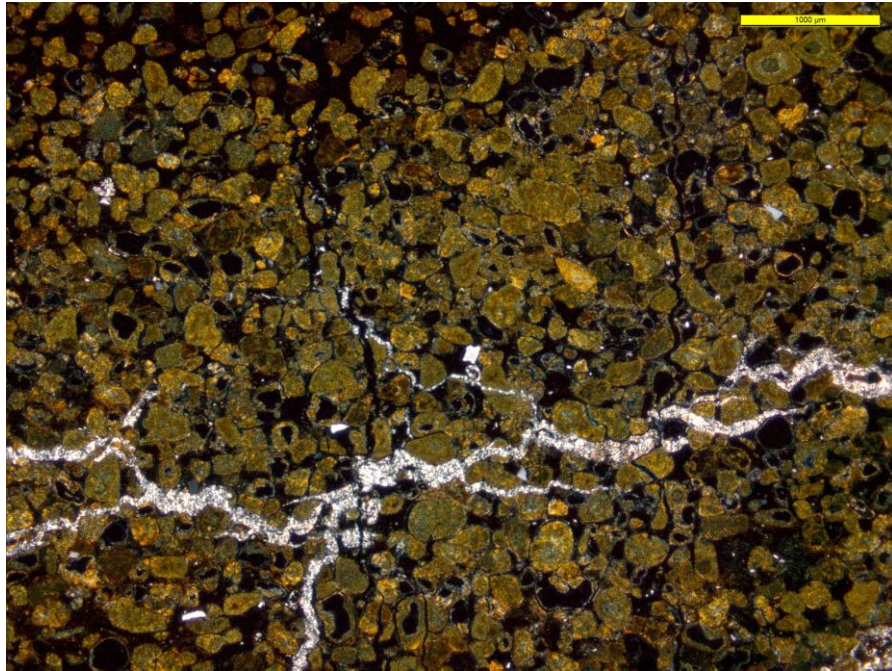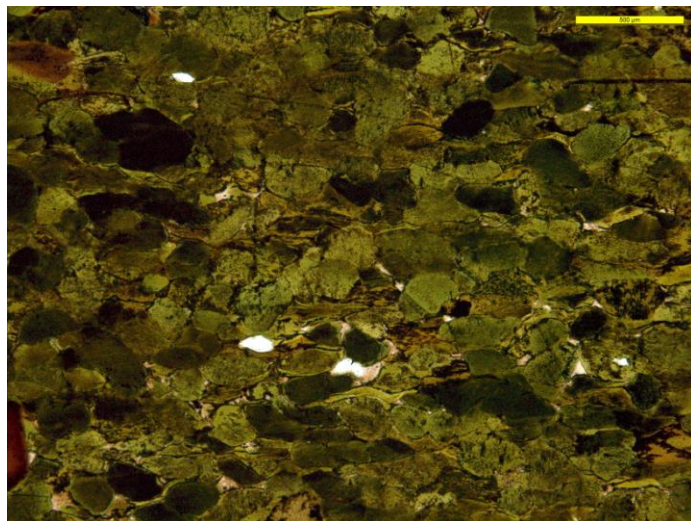Fig. 6.17: Thin-section picture of the mine sample in PPL, overview picture of the glauconitic sandstone.
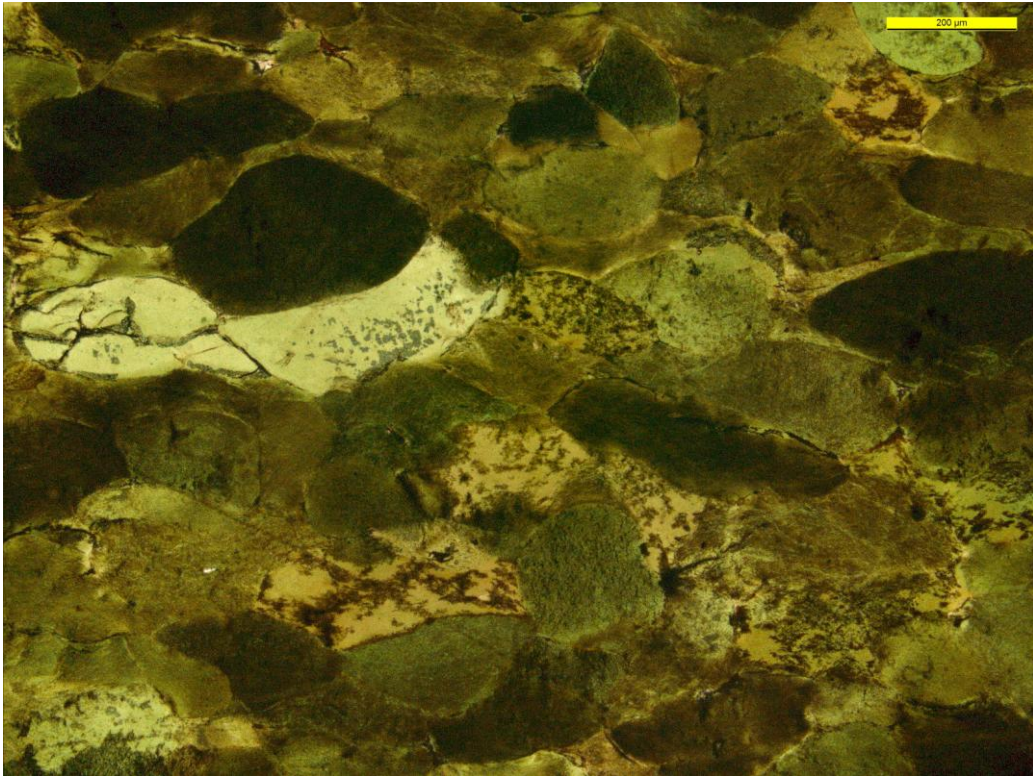
Fig. 6.18: Thin-section picture of glauconite grains of the mine sample, note compaction of grains (PPL).
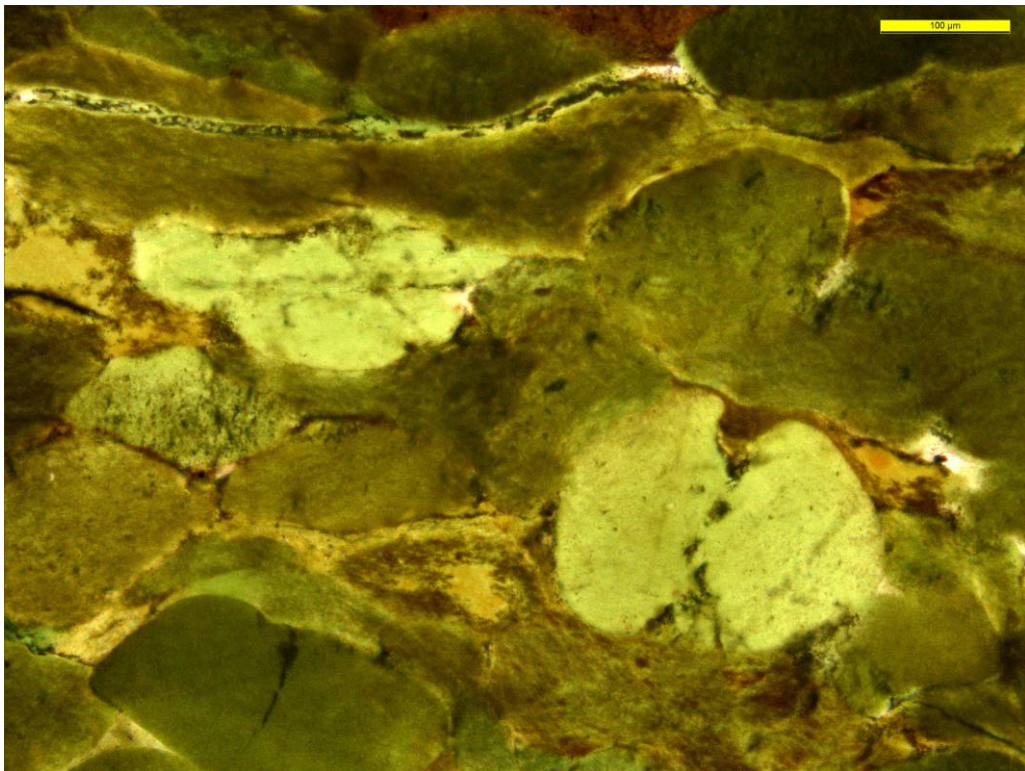
Fig. 6.19: Thin-section picture in PPL of the mine sample, note the light green, cracked glauconite grain.
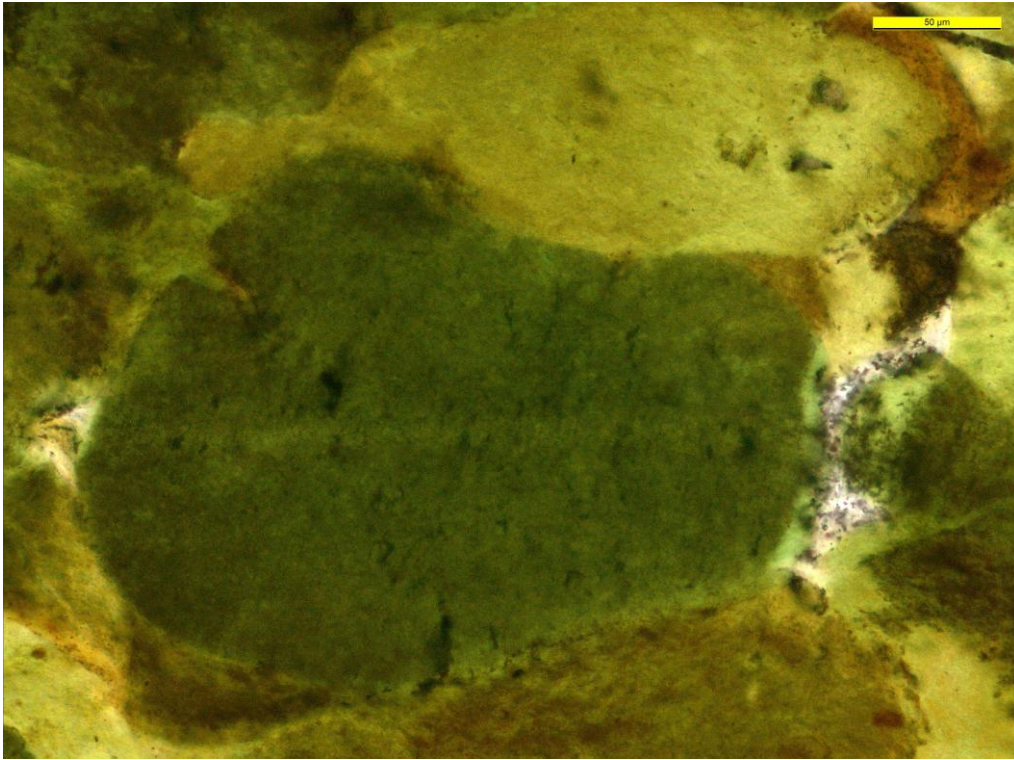
Fig. 6.20: Thin-section picture of a dark green glauconite grain (PPL), mine sample.
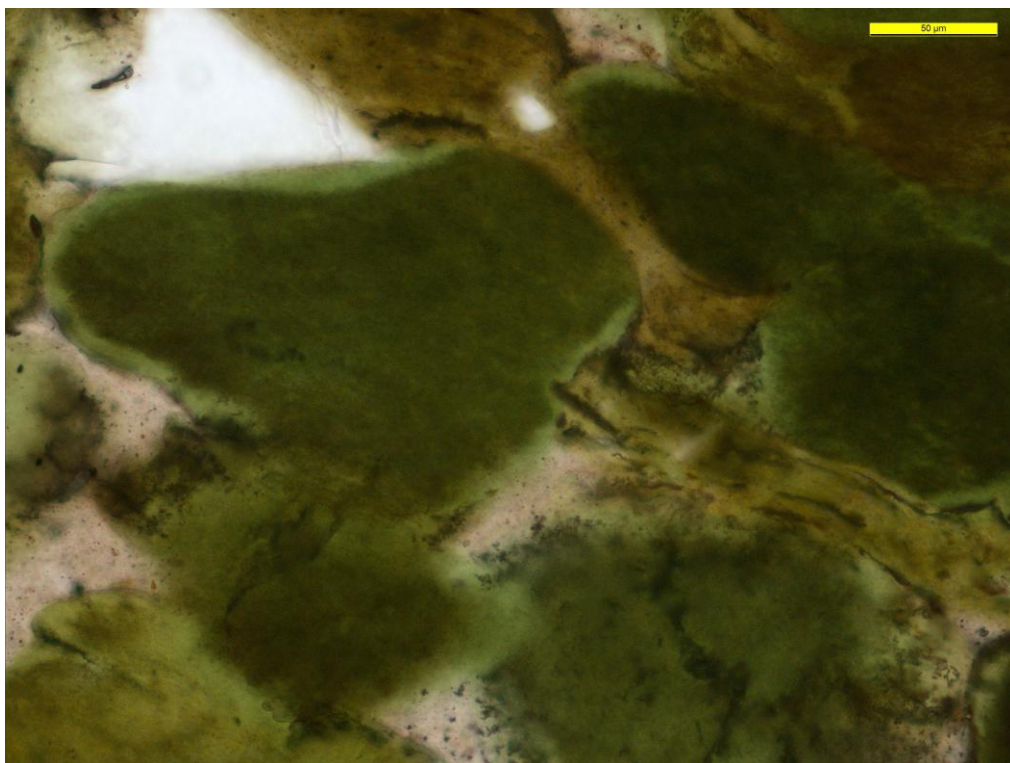
Fig. 6.21: Thin-section picture of zonated glauconite grains of the mine sample, the outermost rim of the grains is much lighter than the centre (PPL).

6.3. Chemical composition

6.3.1. Chemical composition of the bulk samples

Geochemical analyses of the bulk samples AT 31 to AT 36 (layer 16 of profile ATM), the mine sample and ATM 0 to ATM 16 (profile ATM) were carried out.

The obtained data are listed in Tables 6.1, 6.2 and 6.3. The analyses of samples AT 31 to AT 36 and the mine sample gave the following minimum to maximum contents: 40.35 - 60.76% SiO_2, 6.41 – 8.72% Al_2O_3, 21.29 – 43.17% Fe_2O_3, 2.58 – 3.93% MgO, 2.76 – 6.19% K_2O, 0.05 – 3.2% CaO, 0.37 – 1.81% P_2O_5 and 0.03 – 0.88% SO_3.

Table 6.1: XRF analyses of bulk glauconitic sandstones and one subsurface sample (mine).

sample	AT 31	AT 32	AT 33	AT 34	AT 35	AT 36	mine
SiO_2%	40.35	54.03	54.30	60.76	59.95	53.51	55.61
Al_2O_3%	6.41	8.72	7.48	7.20	6.74	6.50	7.86
Fe_2O_3%	43.17	23.46	25.78	21.29	24.52	30.53	22.39
Mn_3O_4%	0.12	0.01	0.02	0.01	0.01	0.01	0.01
MgO%	2.58	3.86	3.93	3.63	3.47	2.75	3.04
CaO%	2.89	2.73	1.78	0.55	0.05	0.08	3.2
Na_2O%	0.08	0.23	0.17	0.09	0.13	0.27	0.25
K_2O%	2.76	5.28	5.50	4.79	4.56	5.15	6.19
P_2O_5%	1.53	0.95	0.67	1.14	0.37	0.68	1.81
SO_3%	0.42	0.88	0.52	0.44	0.29	0.51	0.03
TiO_2%	0.16	0.14	0.16	0.20	0.21	0.24	0.11
Total %	100.63	100.42	100.45	100.24	100.42	100.37	100.70

The glauconitic sandstones from different layers of profile ATM vary in their SiO_2 contents between 51.21% and 64.22%, 6.01% to 9.70% in their Al_2O_3 contents and 14.83% to 21.27% in their Fe_2O_3 contents. Tables 6.2 and 6.3 show the contents of eleven major oxides and trace element contents. The higher CaO (8.72%) and P_2O_5 (3.61%) contents of sample ATM 4 indicate intercalation with phosphorites. The following Table 6.3 shows the chemical composition of black shales and black shales

intercalated with glauconite and the chemical composition of phosphorite (32.11% P_2O_5) and claystone (76.64% SiO_2) of profile ATM. The analyzed black shales are poor in CaO, K_2O, Na_2O, but rich in SiO_2 and Al_2O_3.

Table 6.2: XRF analyses of bulk glauconitic sandstones from different layers of profile ATM (Fig. 6.2).

	glauconitic sandstones			
sample	ATM 2	ATM 3	ATM 4	ATM 12
SiO_2%	58.20	59.56	51.21	64.22
Al_2O_3%	9.70	9.46	6.01	9.32
Fe_2O_3%	19.96	17.99	21.27	14.83
Mn_3O_4%	0.04	0.02	0.21	0.01
MgO%	3.91	4.02	5.23	3.57
CaO%	2.44	2.91	8.72	1.92
Na_2O%	0.13	0.11	0.17	0.17
K_2O%	4.17	3.93	3.66	4.01
P_2O_5%	1.58	1.85	3.61	1.67
SO_3%	0.11	0.25	0.32	0.45
TiO_2%	0.38	0.33	0.21	0.37
Total %	100.75	100.58	100.80	100.65

Table 6.3: XRF analyses of black shales, black shales with glauconite, phosphorites and claystone from profile ATM (Fig. 6.2).

sample	black shales			black shales with glauconite		phosphorite	claystone
	ATM 0	ATM 5	ATM 10	ATM 1	ATM 6	ATM 11	ATM 14
SiO_2%	65.89	69.89	60.24	55.45	56.49	7.01	76.64
Al_2O_3%	22.56	16.23	16.01	11.98	10.13	0.45	13.53
Fe_2O_3%	5.23	5.72	12.65	21.03	20.31	5.02	3.78
Mn_3O_4%	0.01	0.00	0.02	0.22	0.01	0.02	0.01
MgO%	3.61	4.40	3.49	4.69	4.45	0.85	0.99
CaO%	0.16	0.04	2.03	2.83	2.91	50.31	0.45
Na_2O%	0.12	0.10	0.27	0.10	0.19	0.83	0.27
K_2O%	1.25	1.64	1.92	2.37	3.79	0.11	2.54
P_2O_5%	0.28	0.07	0.42	1.01	0.90	32.11	0.45
SO_3%	0.04	1.00	2.08	0.19	0.80	2.84	0.04
TiO_2%	1.17	1.08	0.87	0.49	0.40	0.02	1.34
Total %	100.53	100.30	100.15	100.54	100.55	99.89	100.38

It is important to bear in mind that the bulk analysis of a sample, even purified, is likely to be a mixture of initial substrates and authigenic glauconitic materials (Odin & Matter, 1981).

6.3.2. Chemical composition and structural formulae of glauconite grains

Electron microprobe analysis was carried out on six glauconitic sandstone samples AT 31 to AT 36 and the mine sample. Seven morphologically different grains of each sample were analyzed. The major elements (in %) were measured in the centre and the outer rim of the glauconite grains. A noticeable variation in the geochemical composition of the glauconite grains is evident from the microprobe results. Figures 6.22 and 6.23 show glauconite grains chosen for measuring the chemical composition.
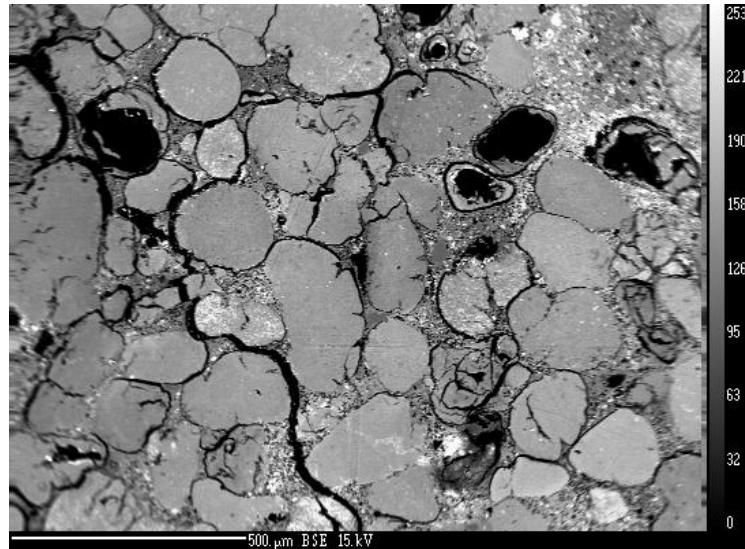
Fig. 6.22: BSE (Back-scattered electron) image of sample AT 31.
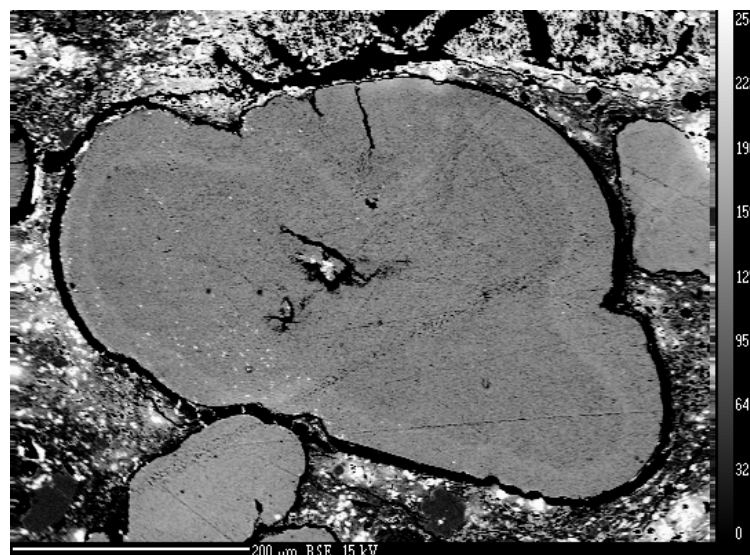
Fig. 6.23: BSE image of a zonated glauconite grain, AT 31.

The analyses show, as expected, that the glauconite grains vary in composition across the grain.

Generally, samples AT 34, AT 35 and AT 36 from the upper part of the glauconite layer show lower K_2O values than AT 31 to AT 33 from the lower part. The silica content ranges between 48.15 – 52.65% SiO_2 for samples AT 31 and AT 32. Samples AT 33 to AT 36 show higher silica contents between 50.63 – 64.66% SiO_2. These high SiO_2

values can be explained by quartz impurities in the glauconite grains. Intermediate silica contents of 48.30 – 53.22% are found in the mine sample.

The aluminum-content of the glauconite grains varies between 5.28 and 11.69% Al_2O_3. The results are in good agreement with published aluminum contents obtained by Odin & Matter (1981). Generally, the measured glauconite grains of samples AT 31, AT 32 and AT 33 exhibit higher values of Al_2O_3 in the outer rim than in the centre.

The iron-content of samples AT 31 to AT 33 varies from 16.35 to 24.28% Fe_2O_3. The iron-contents of the mine sample vary within a similar range (16.58 – 22.10% Fe_2O_3). AT 34 to AT 36 have lower iron values of 6.10 - 17.52% Fe_2O_3. The Fe_2O_3 content of the glauconite grains increases from sample sample AT 36 (top of layer 16) to AT 31 (base of layer 16).

The percentage of magnesium is constant between 2.11 and 3.72% MgO.

Potassium is the most variable cation found in glauconitic minerals (Odin & Matter, 1981). For samples AT 31 to AT 33 the potassium content varies between 4.44 and 6.91% K_2O. The content of potassium of AT 34 to AT 36 ranges between 1.57 and 5.23% K_2O. Generally, there is an increase of potassium within layer 16 from the top to the bottom. The mine sample has potassium contents between 5.89 and 7.24% K_2O.

The content of sulfur decreases within layer 16 from the top (0.58 – 3.06% SO_2) to the bottom (0.35 – 0.83% SO_2). The sulfur contents of the mine sample are very low between 0.024 and 0.130% SO_2.

Zonation in glauconite grains in back-scattered images of the mine sample are caused by the Fe and K contents.

The crystal-chemical structural formulae of the different glauconite grains were calculated using the Marshall-Method (Marshall, 1949). The formulae of 2:1-phyllosilicates were calculated assuming an ideal structure with 22 negative charges of ten oxygen and two hydroxyl-groups (Köster, 1977). An example of a calculated, simplified structural formula for glauconite is:

$$(K_{0.52} Na_{0.01} Ca_{0.01}) (Al_{0.42} Fe_{1.28} Mg_{0.38}) (Si_{3.62} Al_{0.38}) O_{10} (OH)_2$$
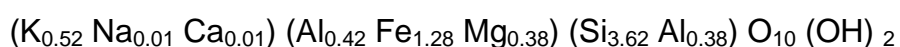
The high proportion of K is related to the marine origin of glauconite. Iron contributes more than half of the octahedral charge (Odin & Matter, 1981).

The mean chemical composition of glauconite is presented in Table 5.4 in the appendix together with the calculations of the structural formulae of all the samples.

The relationships of the calculated main elements in octahedral- and interlayer-position were plotted in xy-diagrams. The major chemical variation in the octahedral sheet of glauconite is the ratio of Al to Fe^{3+}. Figs. 6.24, 6.26, 6.27 and 6.28 show that Al in octahedral sites is proportional to Fe in octahedral sites. Al decreases as Fe^{3+} increases and the percentage of expandable layers decreases (Weaver & Pollard, 1973; Thompson & Hower, 1975). This shows the progressive substitution of Fe for octahedral Al. Fig. 6.25 and Fig. 6.29 show the negative correlation between Al in octahedral and K in interlayer-position. The amount of K in the interlayer position of glauconite increases systematically with a decrease of Al in the octahedral sites. Hower (1961) and Strickler and Ferrell (1990) reported that an increase in the number of K atoms is related to an increase in the degree of burial diagenesis and a decrease of expandable layers.
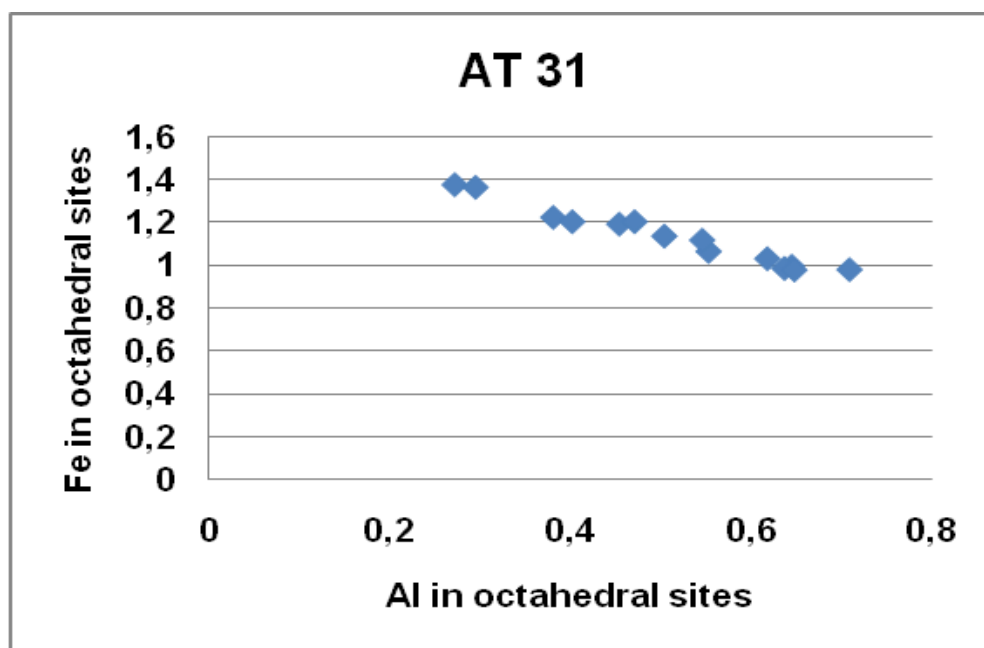
Fig. 6.24: Relationship between Al and Fe in octahedral sites, sample AT 31.
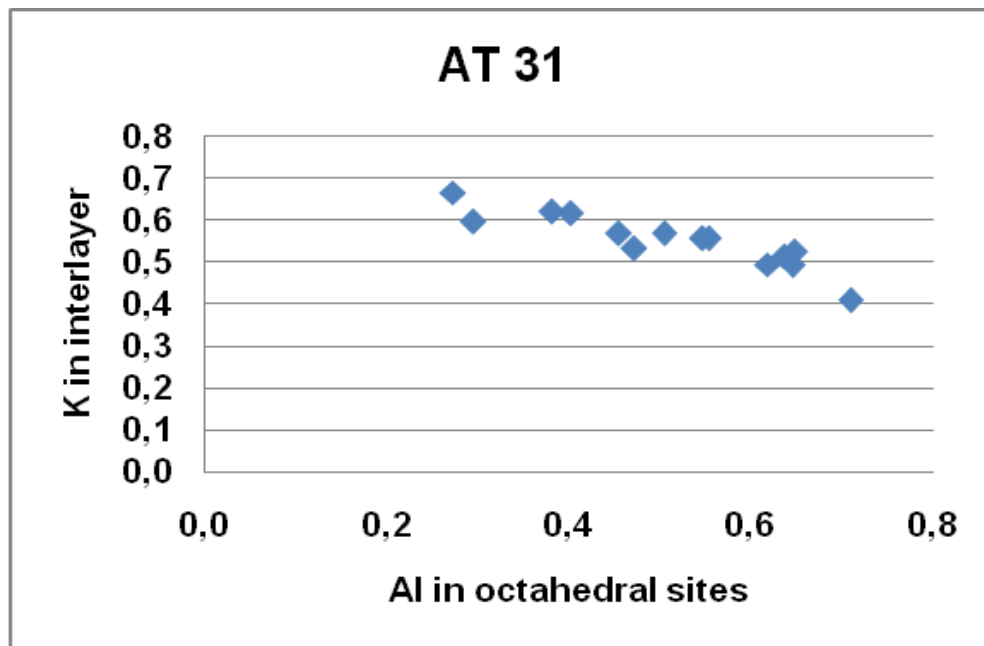
Fig. 6.25: Relationship between Al in octahedral sites and K in interlayer-position, sample AT 31.
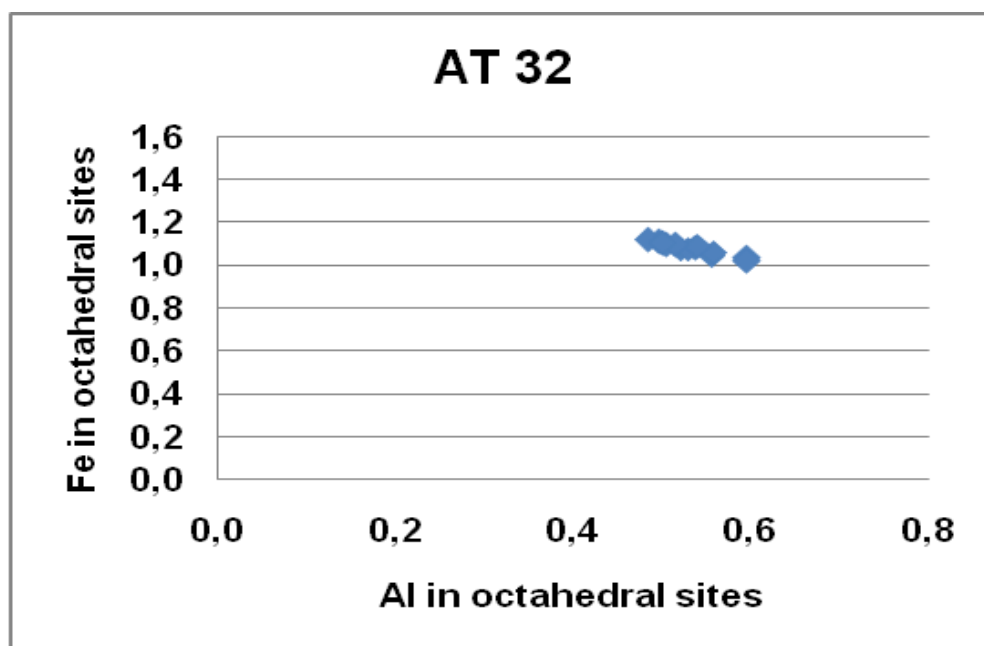
Fig. 6.26: Relationship between Al and Fe in octahedral sites, sample AT 32.
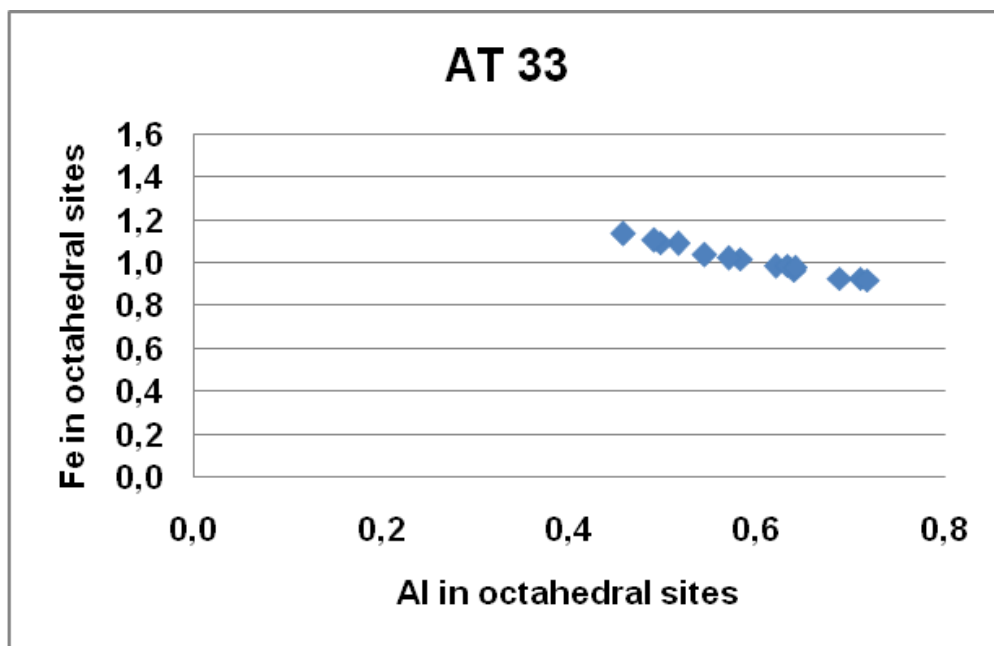
Fig. 6.27: Relationship between Al and Fe in octahedral sites, sample AT 33.
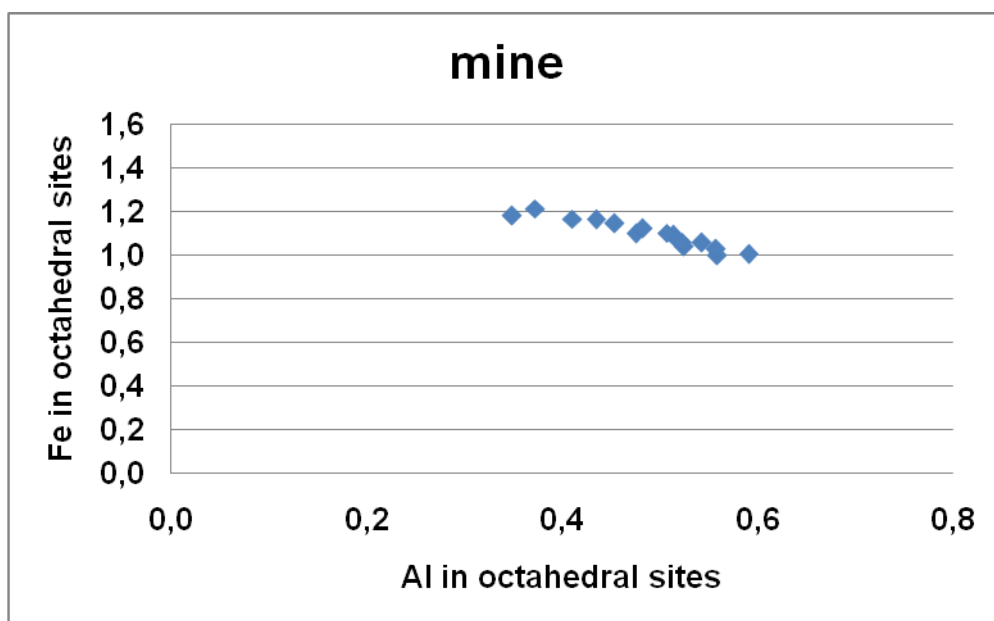
Fig. 6.28: Relationship between Al in octahedral sites and Fe in octahedral sites of the mine sample.
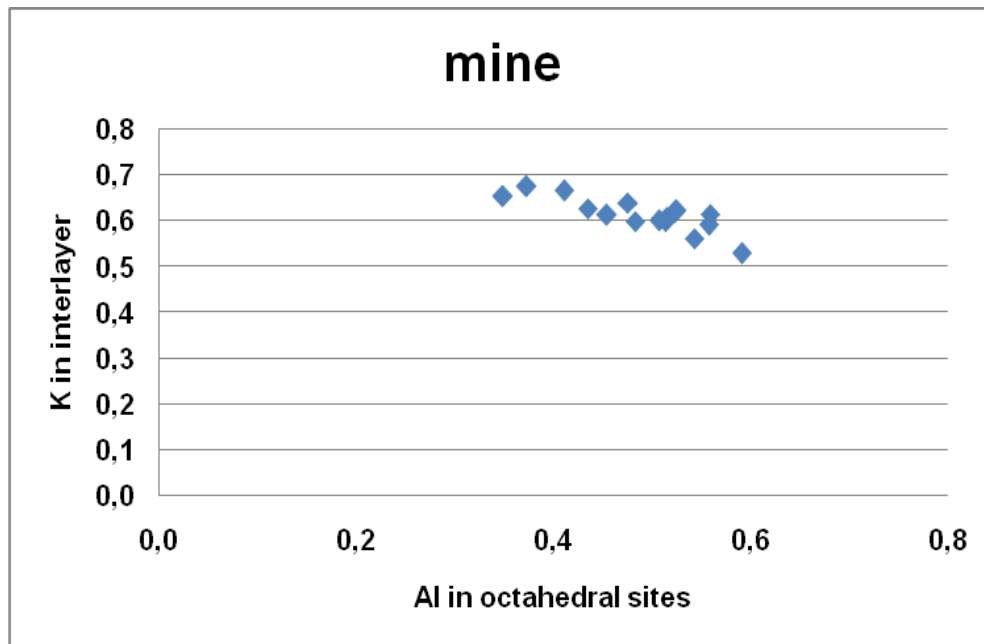
Fig. 6.29: Relationship between Al in octahedral sites and K in the interlayer of the mine sample.

Fourteen analytical points in the core and outer rim of glauconite grains in samples AT 31 to AT 36 were measured. Fig. 6.30 to Fig. 6.33 show positive correlations between K_2O and Fe_2O_3. AT 34 to AT 36 show better correlations than AT 31 to AT 33.
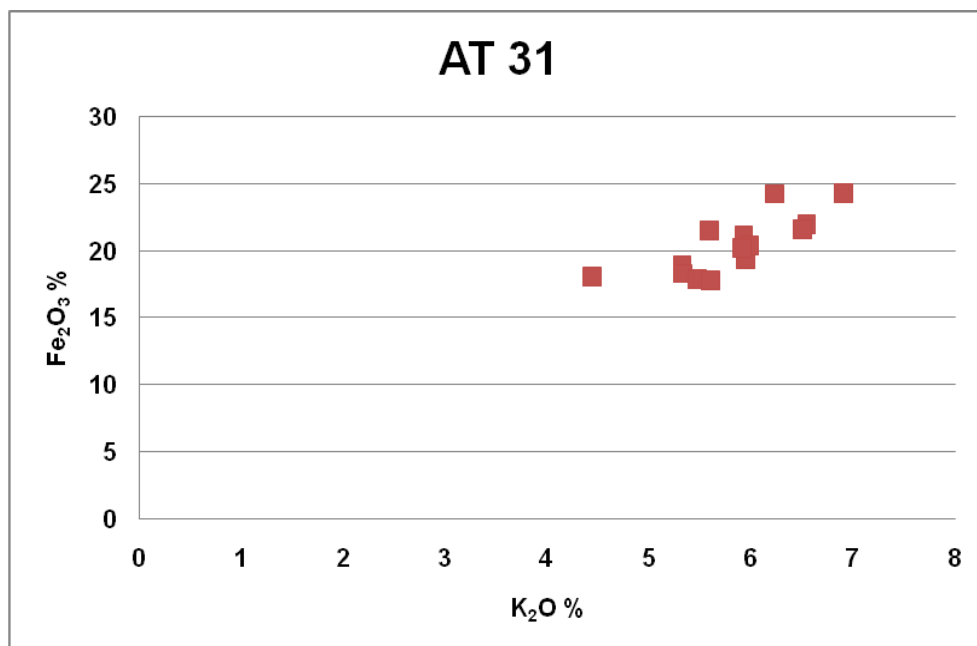
Fig. 6.30: Relationship between K_2O and Fe_2O_3 of sample AT 31.
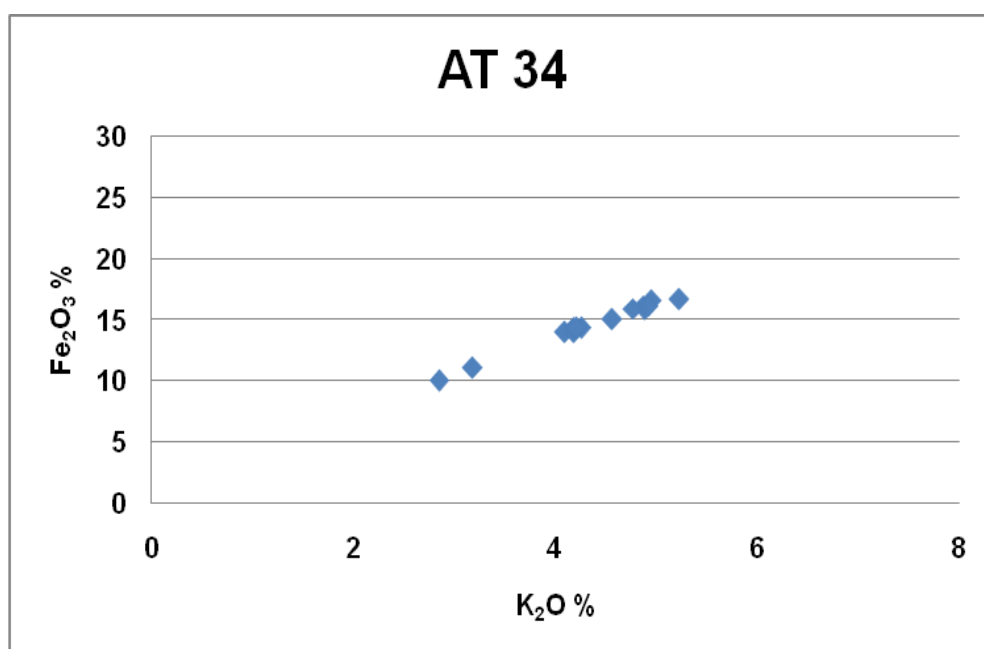
Fig. 6.31: Relationship between K_2O and Fe_2O_3 of sample AT 34.
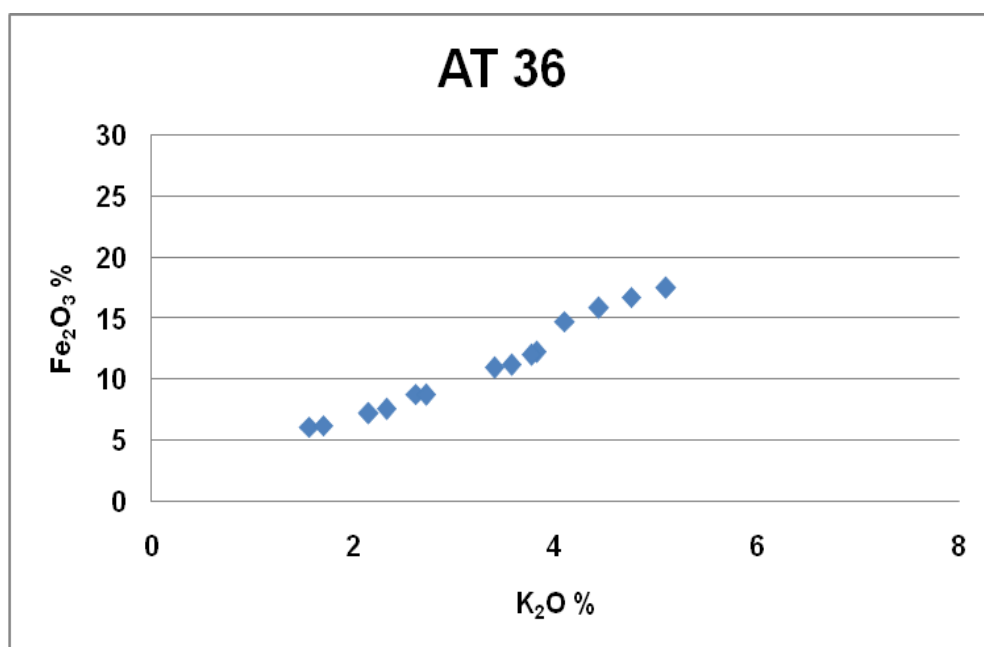
Fig. 6.32: Relationship between K_2O and Fe_2O_3 of sample AT 36.
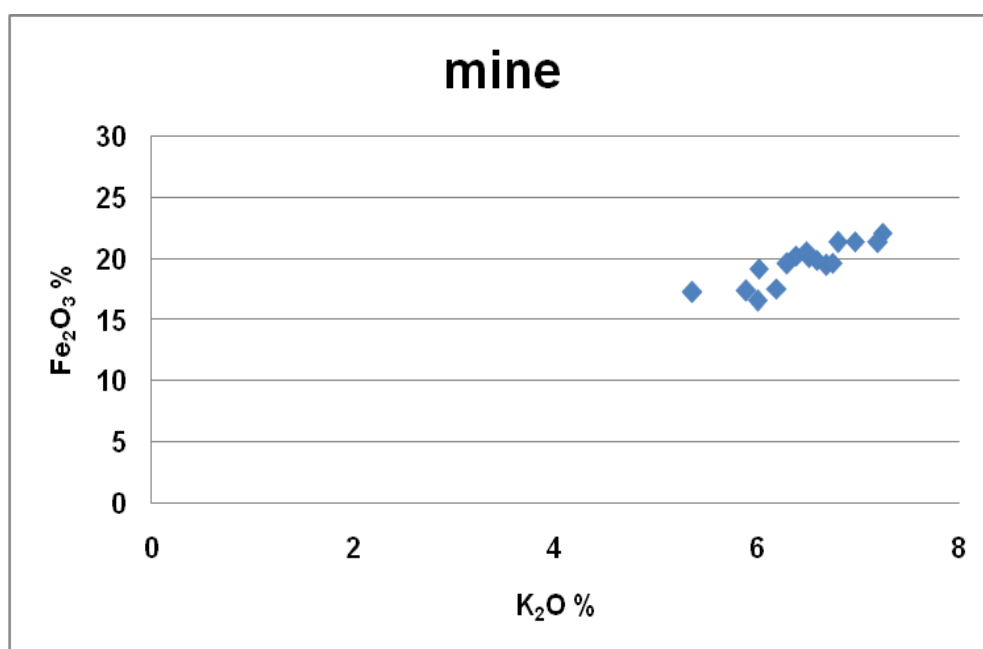
Fig. 6.33: Relationship between K_2O and Fe_2O_3 of the mine sample.

Additional, the charges of the tetrahedral-, octahedral- and interlayer were calculated and plotted in a charge distribution diagram (after Köster, 1977, Fig. 6.34).

The charge-plot of samples AT 31 to AT 36 shows a noticeable trend from the illite-(glauconite-) to the montmorillonite (smectite) field. Most of the samples plot between the smectite field and the illite- respectively glauconite field, indicating mixed-layer minerals. There are two exceptions of sample AT 31, which plot in the illite field. Data of the mine sample plot exactly in the glauconite field. Samples AT 34 to AT 36 plot in the montmorillonite field.

Generally, tetrahedral charges increase from sample AT 36 to AT 31 while octahedral charges decrease from AT 36 to AT 31.
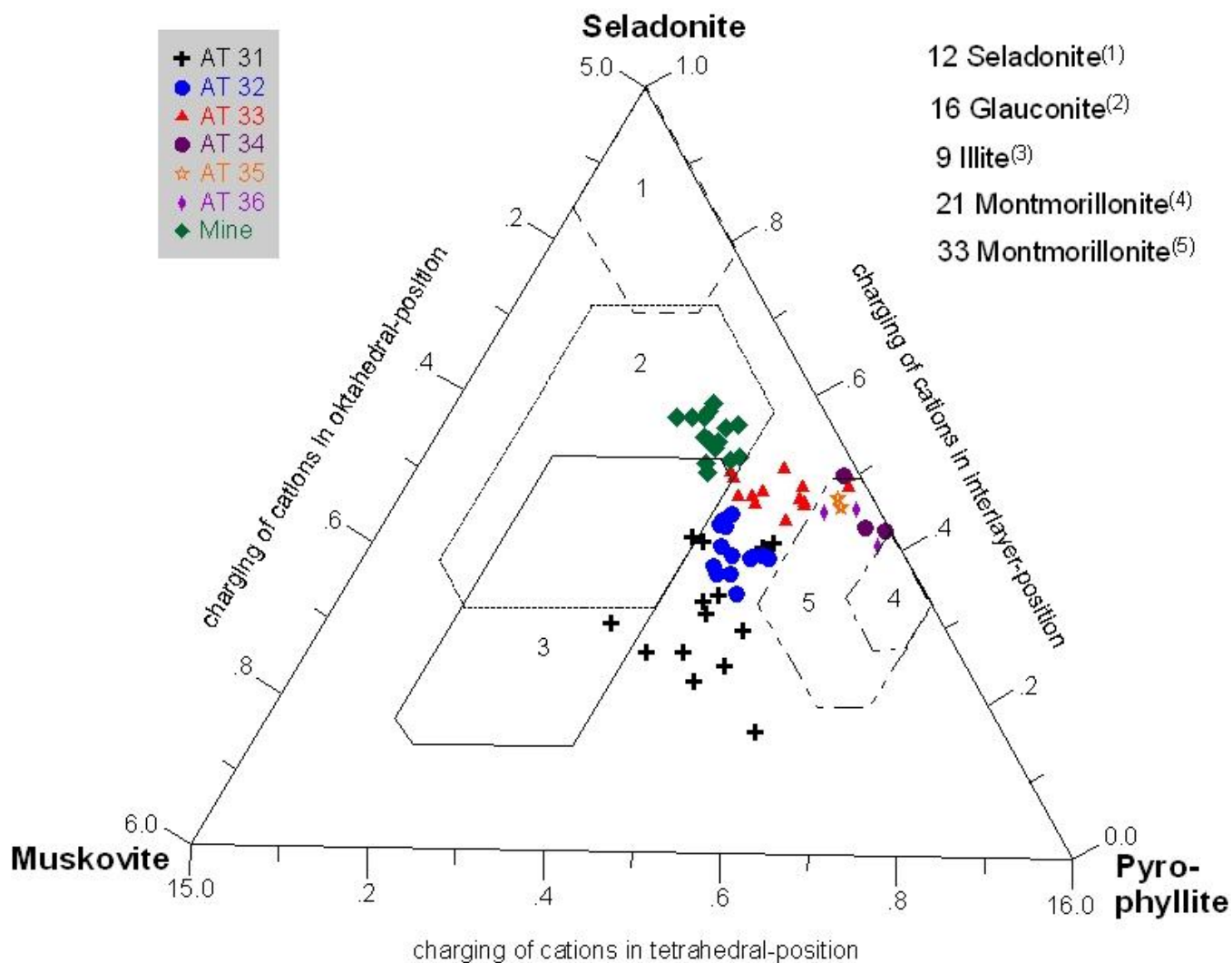
Fig. 6.34: Ternary diagram with end members celadonite, muskovite and pyrophyllite (modified from Köster, 1977).

6.4. Mineralogical composition of bulk samples and clay fraction

6.4.1. Mineralogy of bulk samples

X-ray diffraction patterns of the bulk samples showed, besides clay minerals, the presence of quartz, anhydrite and gypsum. AT 31 also contains hematite and a not clearly identified phosphate-phase (Fig. 6.35). AT 32 to AT 36 also show the mineral jarosite in the diffractograms. Diffractograms of the bulk sample AT 32 are given in the appendix, Figure 6.51.
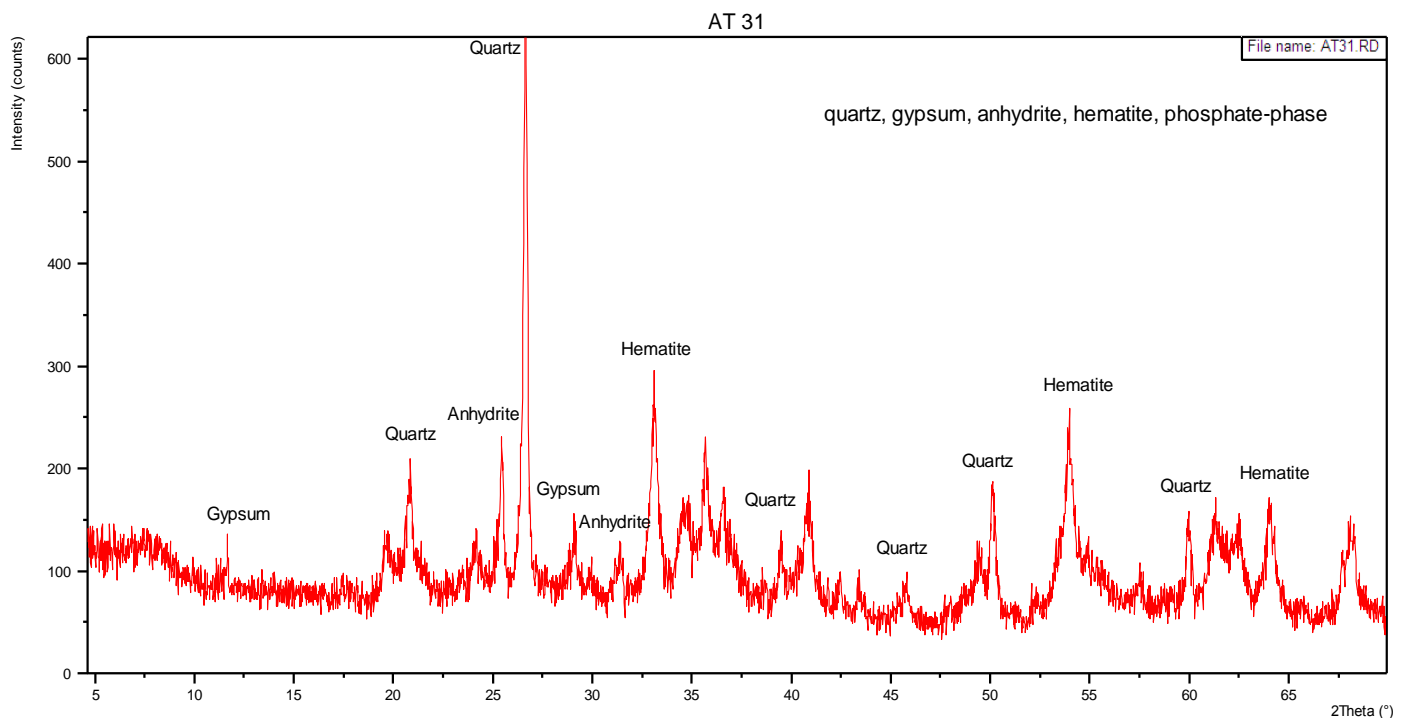
Fig. 6.35: X-ray diffraction pattern of sample AT 31.

6.4.2. Mineralogy of clay fraction

The mineralogical analysis was carried out on samples AT 31 to AT 36 and on the mine sample, which provided detailed informations about the composition of the clay fractions (<2 µm). Based on the X-ray diffraction patterns, it is difficult to establish which peak can be assigned to the matrix and which one to the authigenic grains.

A selection of the obtained diffractograms is shown in Figs. 6.36 and 6.37. Based on the data, the studied clay fractions of samples AT 31 to AT 36 can be described as randomly and ordered interstratified illite(glauconite)/smectite mixed-layers with different contents of illite and smectite. R0 and R1 illite/smectite mixed-layer types were found in the diffractograms. The diffractogram of the mine sample shows a R1 illite(glauconite)/smectite type with about 80% illite layers (Fig. 6.37). AT 31 to AT 36 contains less illite in illite(glauconite)/smectite mixed-layers (Brindley & Brown, 1980). The diffractogram of sample AT 31 (Fig. 6.36) shows a randomly interstratified (R0) illite(glauconite)/smectite mixed-layer with 52% illite layers. The diffractograms of the clay fractions of samples AT 32 to AT 36 are given in the appendix Fig. 6.52 to Fig. 6.56.
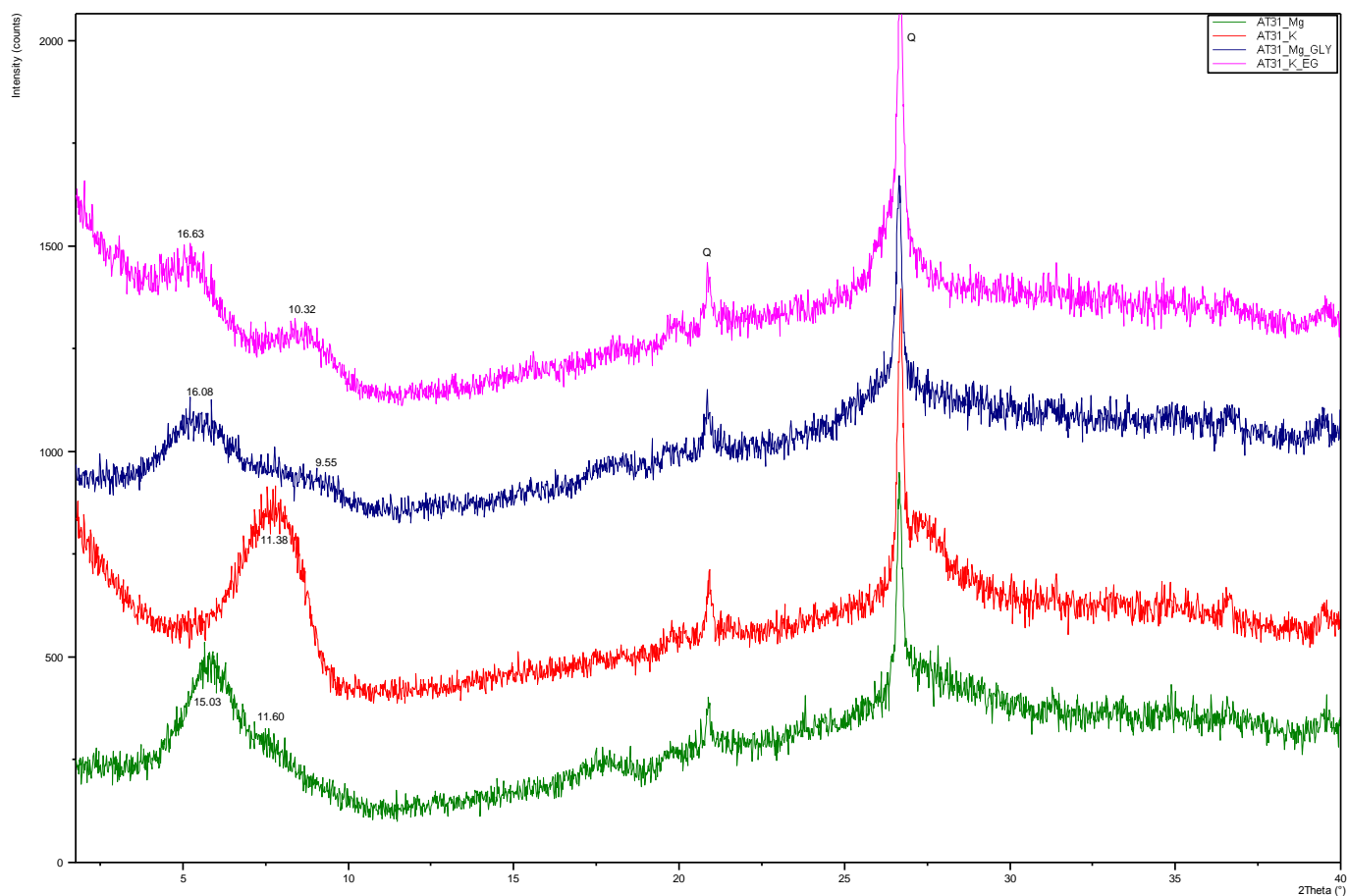
Fig. 6.36: X-ray diffraction patterns of the clay fraction of sample AT 31. Sample is saturated with magnesium (Mg), magnesium plus glycerol (Mg_GLY), potassium (K) and potassium plus ethylenglycol (K_EG); inserted values are d-spacings in Å
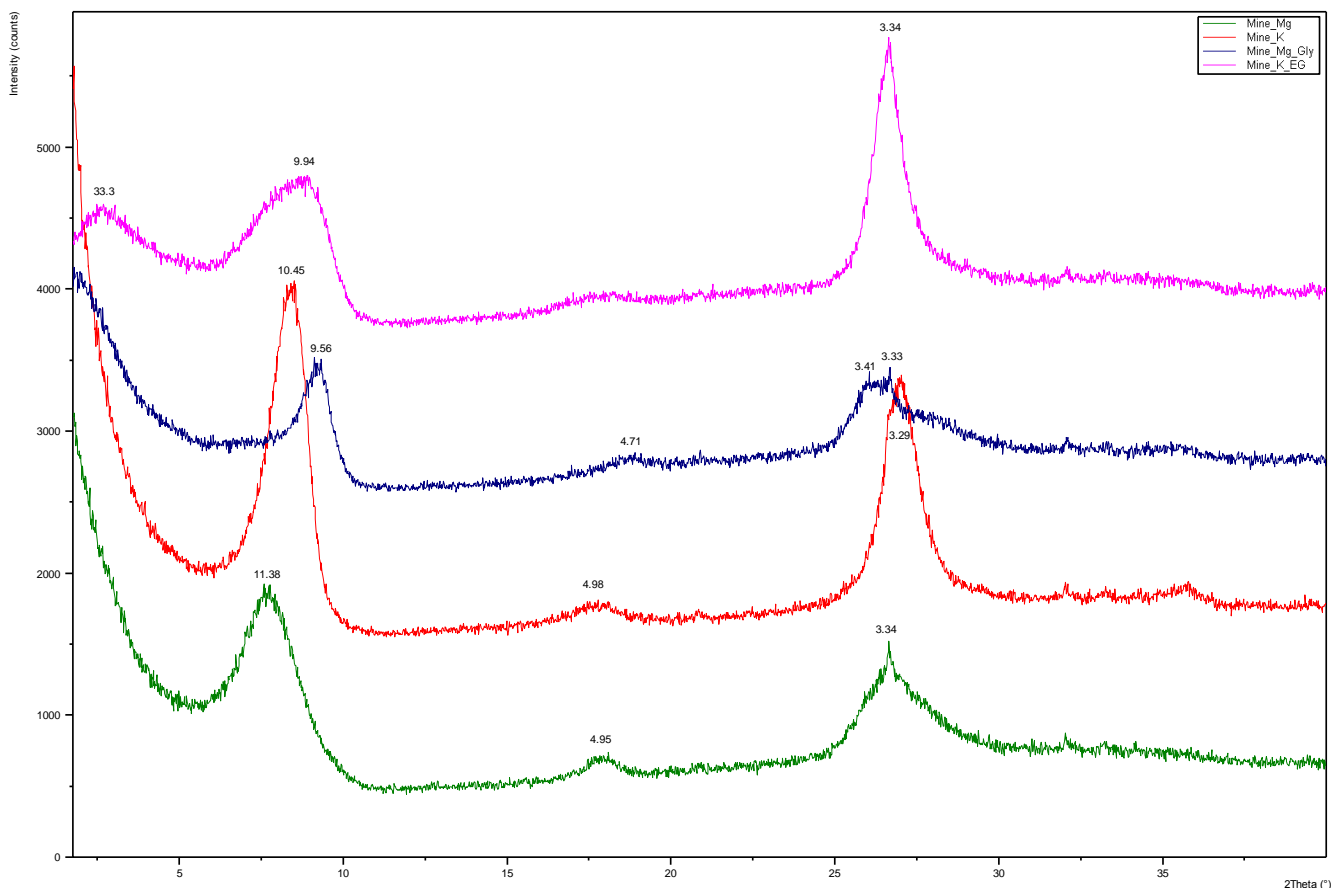
Fig. 6.37: X-ray diffraction patterns of the clay fraction of the mine sample. Sample is saturated with magnesium (Mg), magnesium plus glycerol (Mg_GLY), potassium (K) and potassium plus ethylenglycol (K_EG); inserted values are d-spacings in Å

6.5. Morphology of glauconite grains

SEM images of the glauconitic sandstones generally show round and oval glauconite grains in a clayey matrix. The surfaces of the grains show a rosette morphology- the crystal habit of glauconite/smectite mixed-layer minerals (Fig. 6.38B). Precise identification of the mixed layer mineral is based on XRD and EMP analysis. Grains of samples AT 33, AT 34, AT 35 and AT 36 are associated with cubic respectively framboidal very small (~1 µm) pyrite crystals on the surface and in the fractures of the grains (Fig. 6.40A, Fig. 6.44B, Fig. 6.45 and Fig. 6.46). AT 35 and AT 36 show pyrite as pore filling cement between the glauconite grains and the matrix (Fig. 6.41C, Fig. 6.44A, Fig. 6.45 and Fig. 6.46). Assemblages of octahedral pyrite crystals are often found in shrinkage structures but in total, pyrite occurs as minor constituent. AT 31 shows

chlorite growing on the glauconite surface (Fig. 6.38C). SEM images of samples AT 32 and AT 35 show also crystals of gypsum (Fig. 6.39A and Fig. 6.41B). The mine sample shows no pyrite crystals or pyrite as cement (Figs. 6.48 - 6.50).

A

B

C
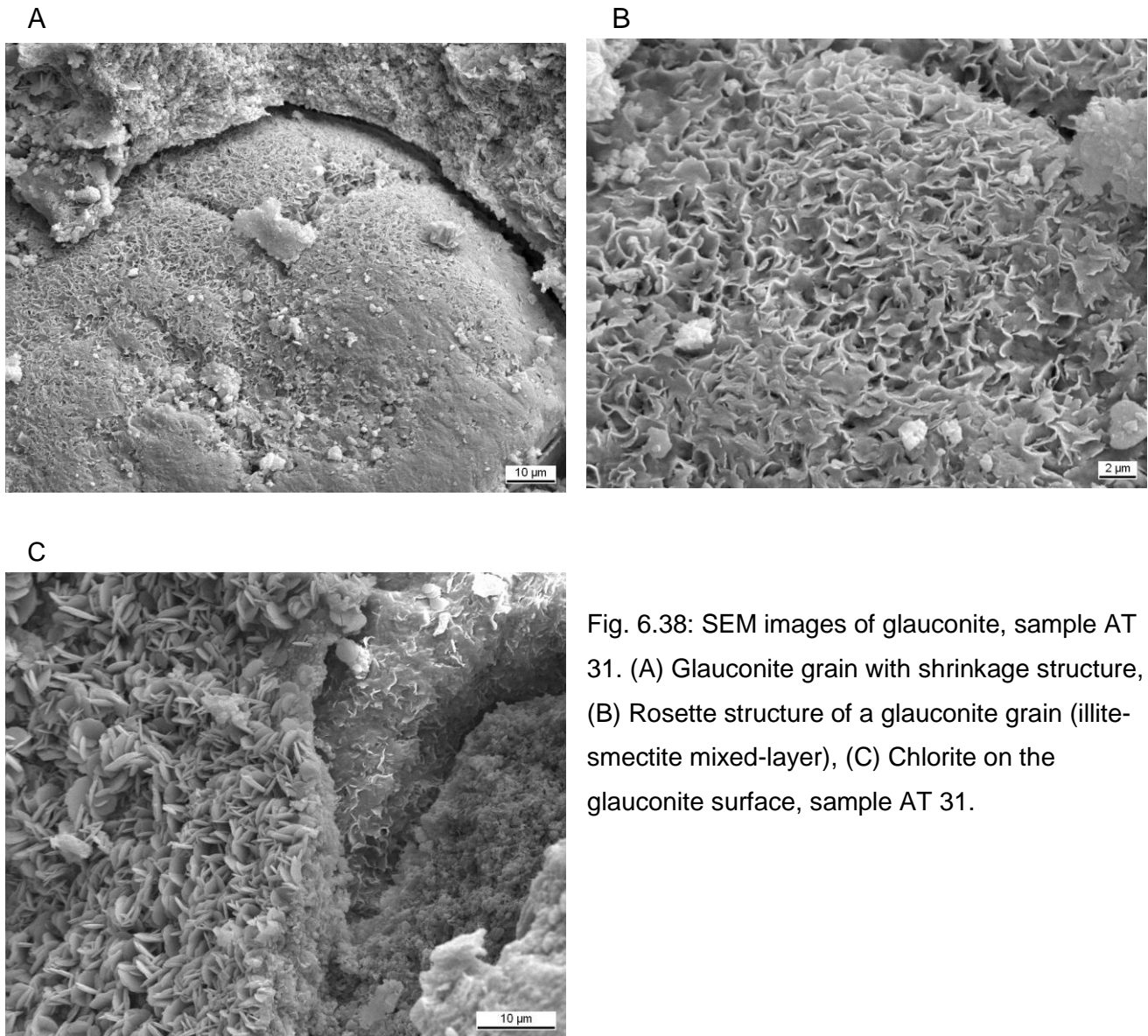
Fig. 6.38: SEM images of glauconite, sample AT 31. (A) Glauconite grain with shrinkage structure, (B) Rosette structure of a glauconite grain (illite-smectite mixed-layer), (C) Chlorite on the glauconite surface, sample AT 31.
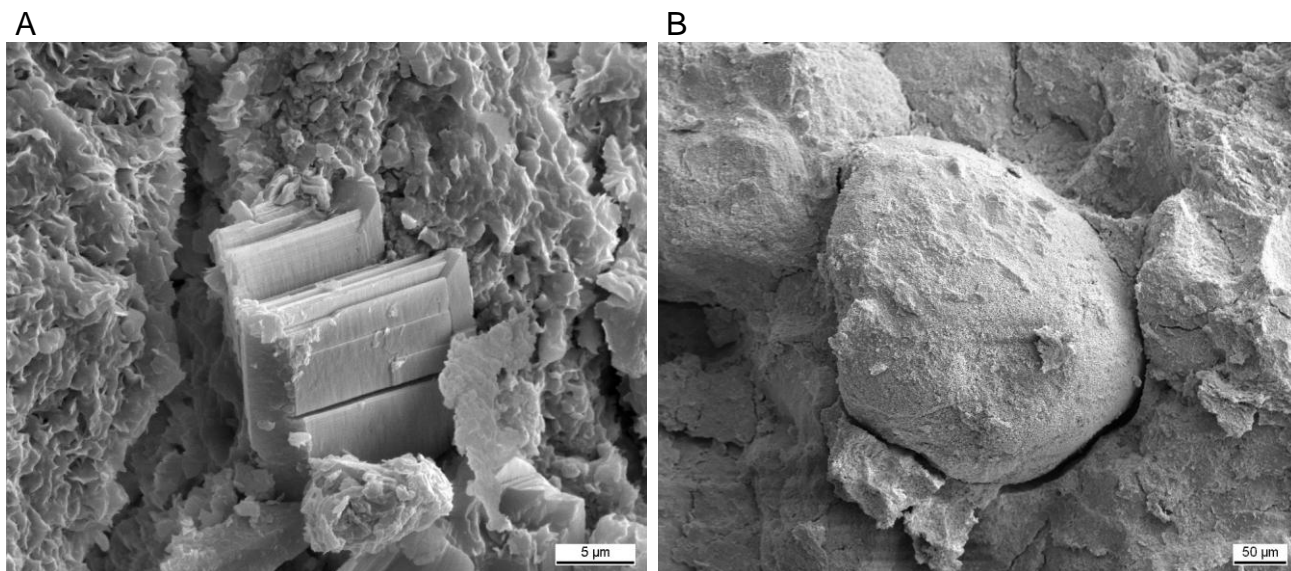
Fig. 6.39: (A) Gypsum/anhydrite-crystal on glauconite surface, AT 32, (B) Glauconite showing smooth rounded surface, sample AT 33.
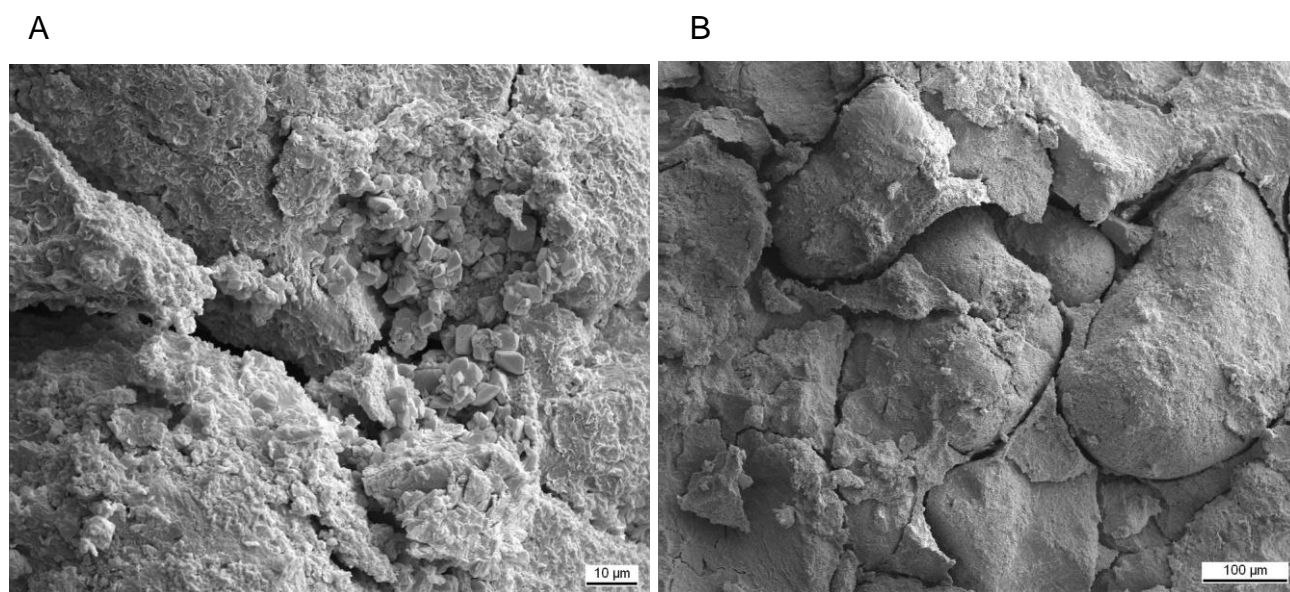
Fig. 6.40: (A) Blocky, sparry pore filling pyrite between authigenic glauconite grains, (B) Glauconite grains in clayey groundmass with shrinkage structures, sample AT 34.

A
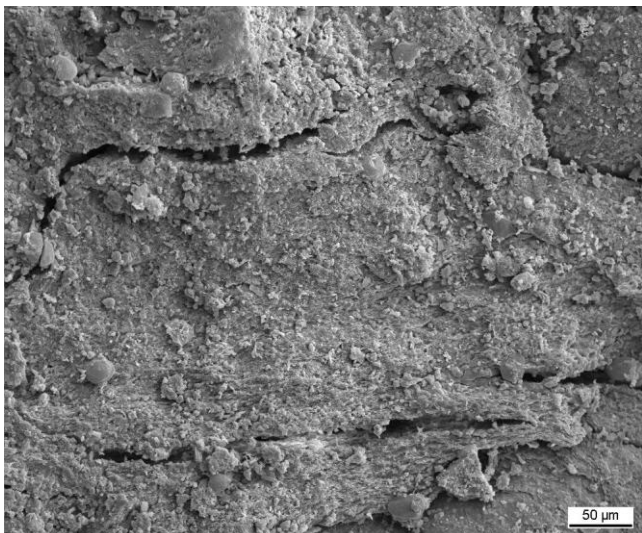
B
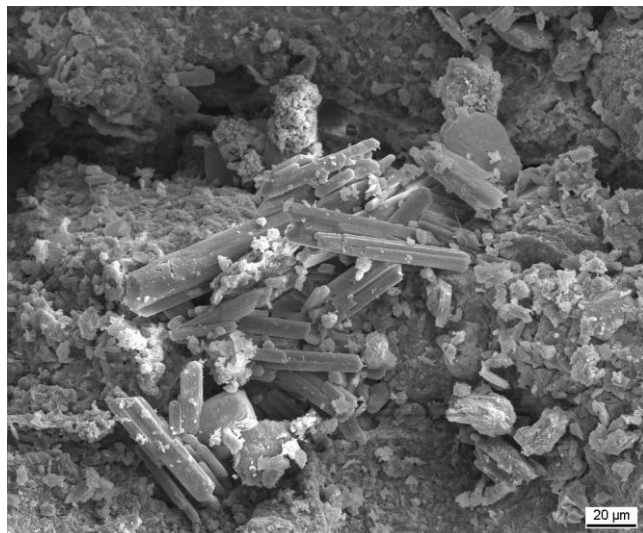
C
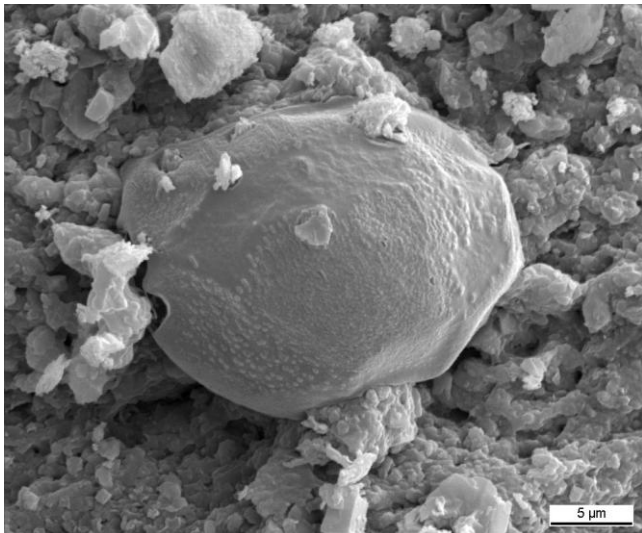
Fig. 6.41: (A) Cross-section of a glauconite grain. (B) Gypsum laths on glauconite surface (C) Pyrite cement covering the surface of glauconite grain, sample AT 35

EDX analysis show that Si, Al, Fe and K are the major constituents of glauconite grains (Fig. 6. 42). Figs. 6.43 and 6.47 show the chemical composition of pyrite (Fe,S) respectively gypsum/anhydrite (Ca,S) measured with EDX.
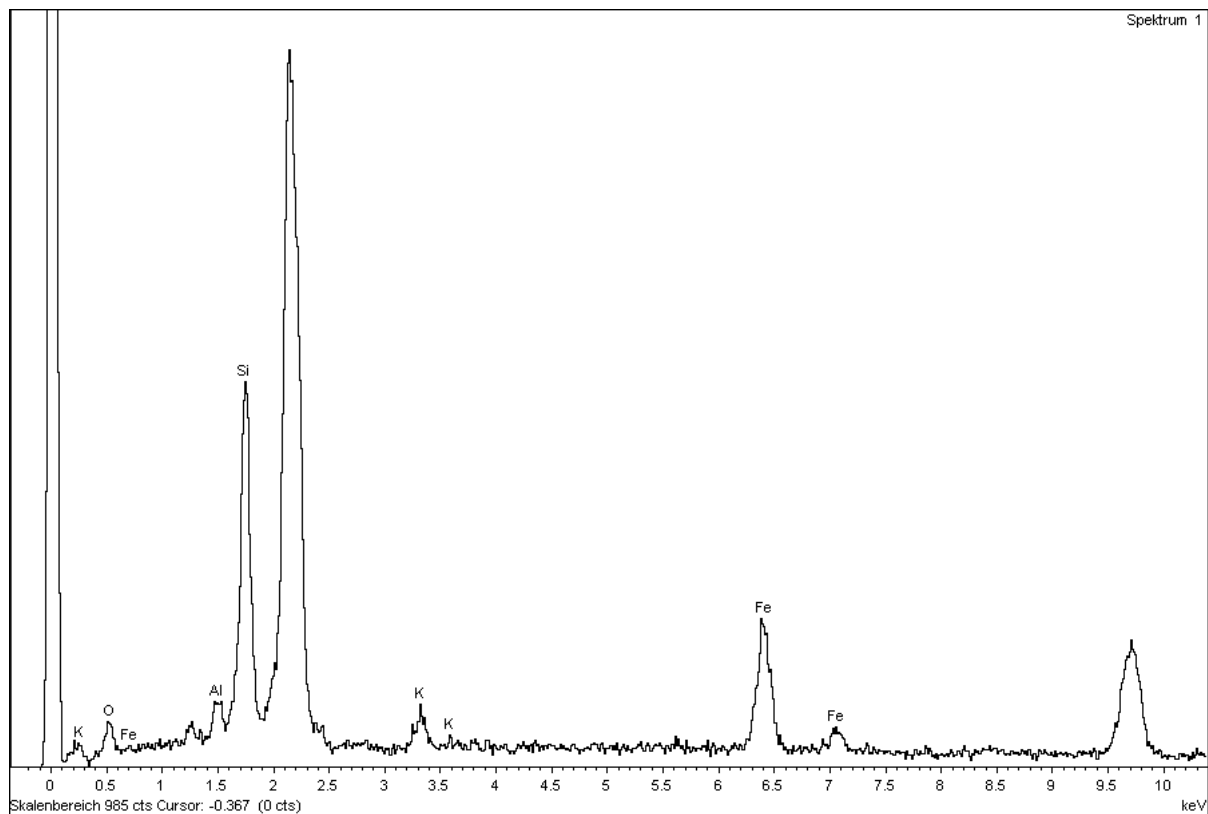
Fig. 6.42: EDX chemical analysis of a glauconite grain, sample AT 36.
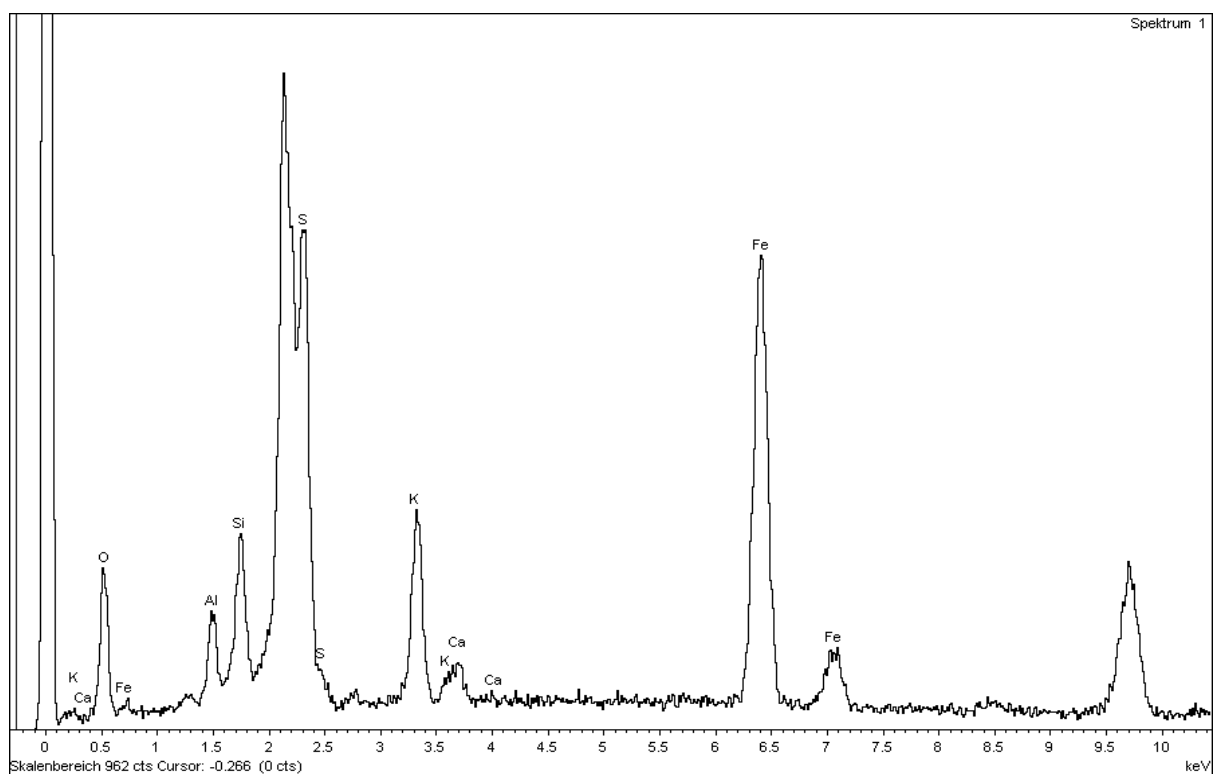
Fig. 6.43: EDX chemical analysis of a glauconite grain with pyrite, sample AT 35.
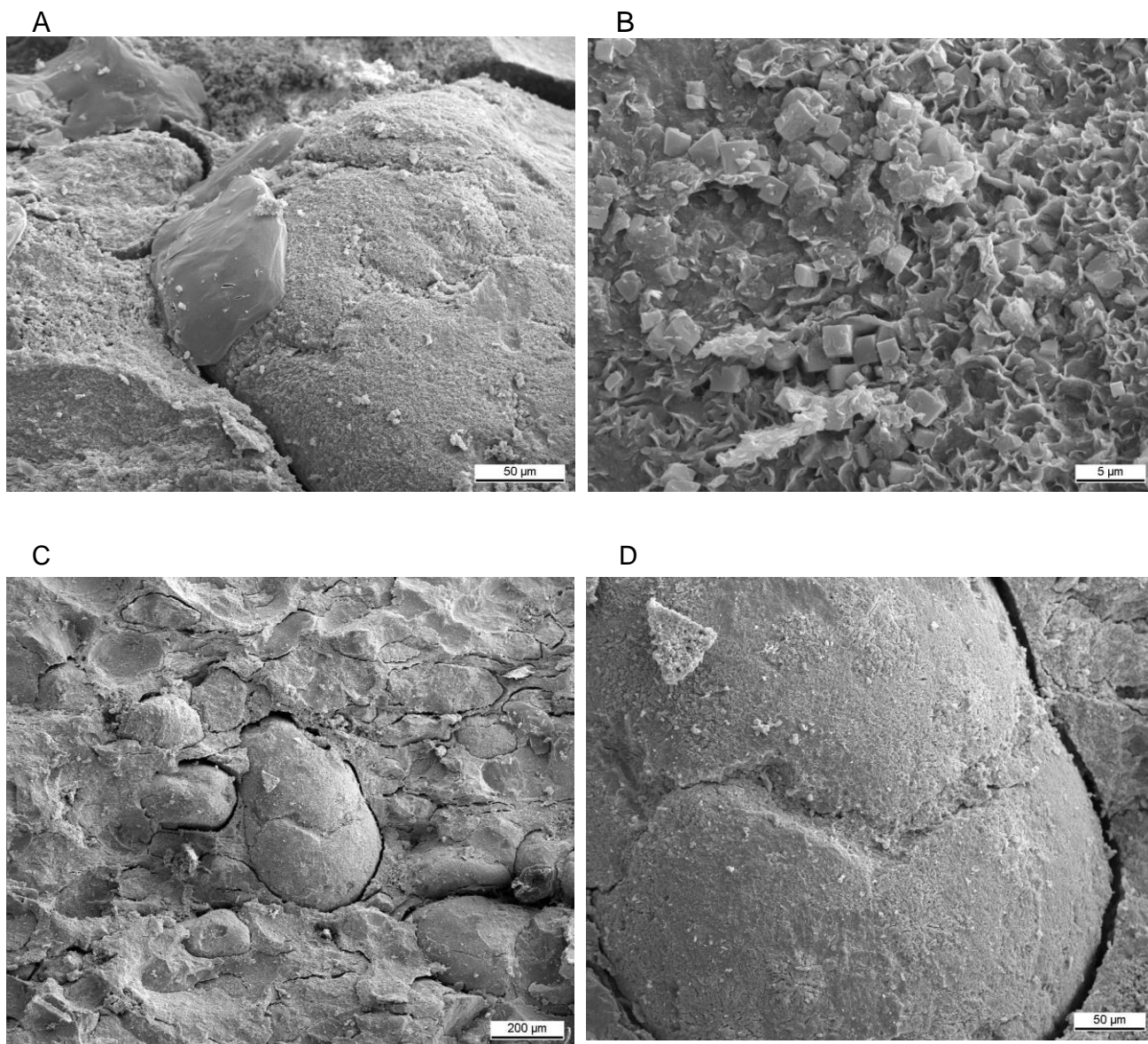
Fig. 6.44: (A) Flat pyrite growing on the glauconite surface filling the shrinkage structure between the grain and the matrix. (B) Euhedral pyrite growing on glauconite surface. (C) Glauconite in clayey matrix. (D) Fractured glauconite grain with shrinkage structure, sample AT 36.
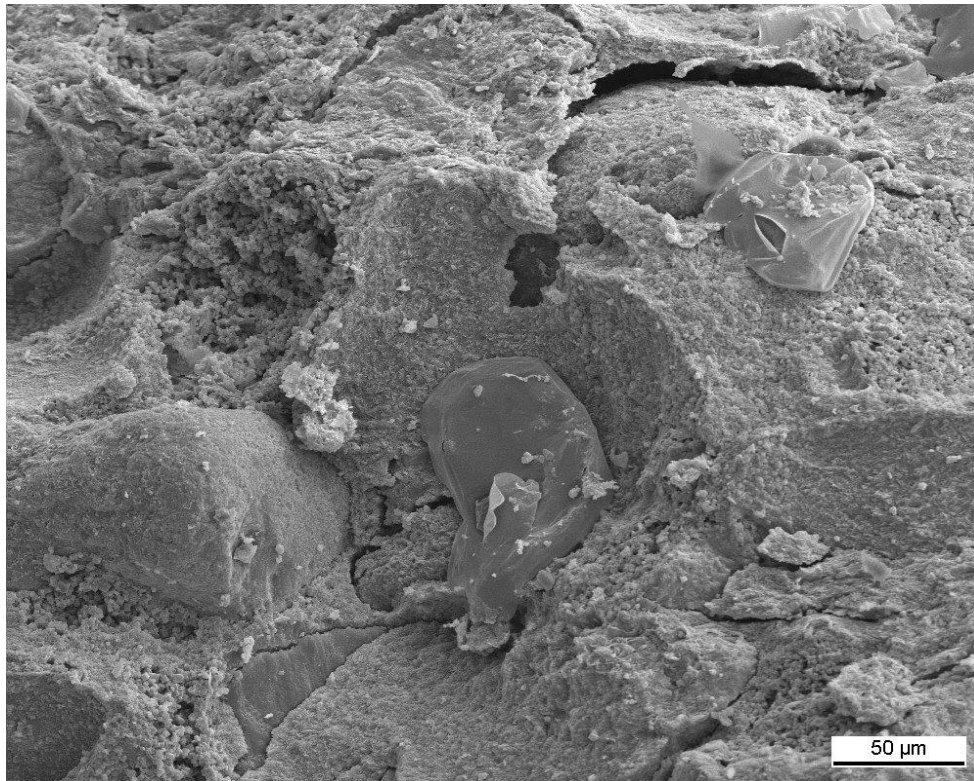
Fig. 6.45: Pyrite cement which precipitated in shrinkage structure between clayey matrix and glauconite grain, sample AT 36.
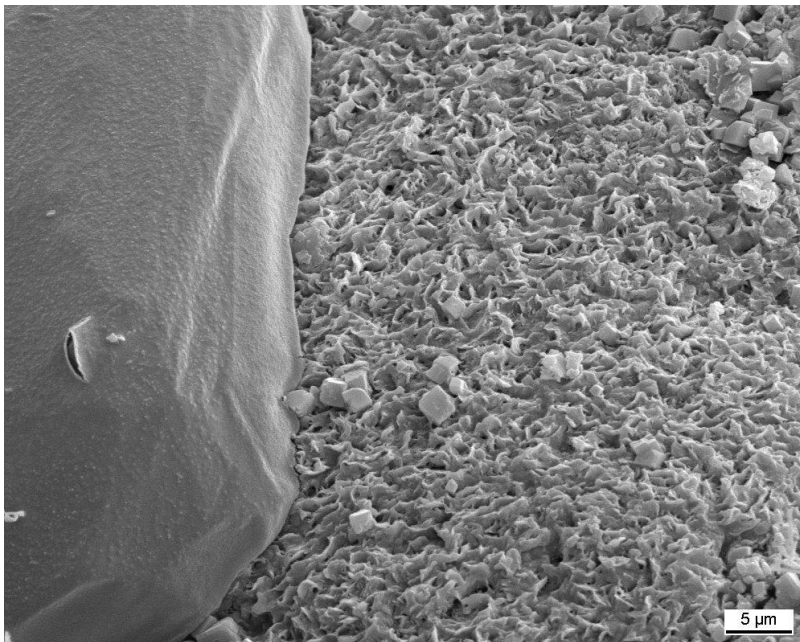
Fig. 6.46: Pyrite cement overgrowth of glauconite grain with cubic pyrite on glauconite surface, sample AT 36.
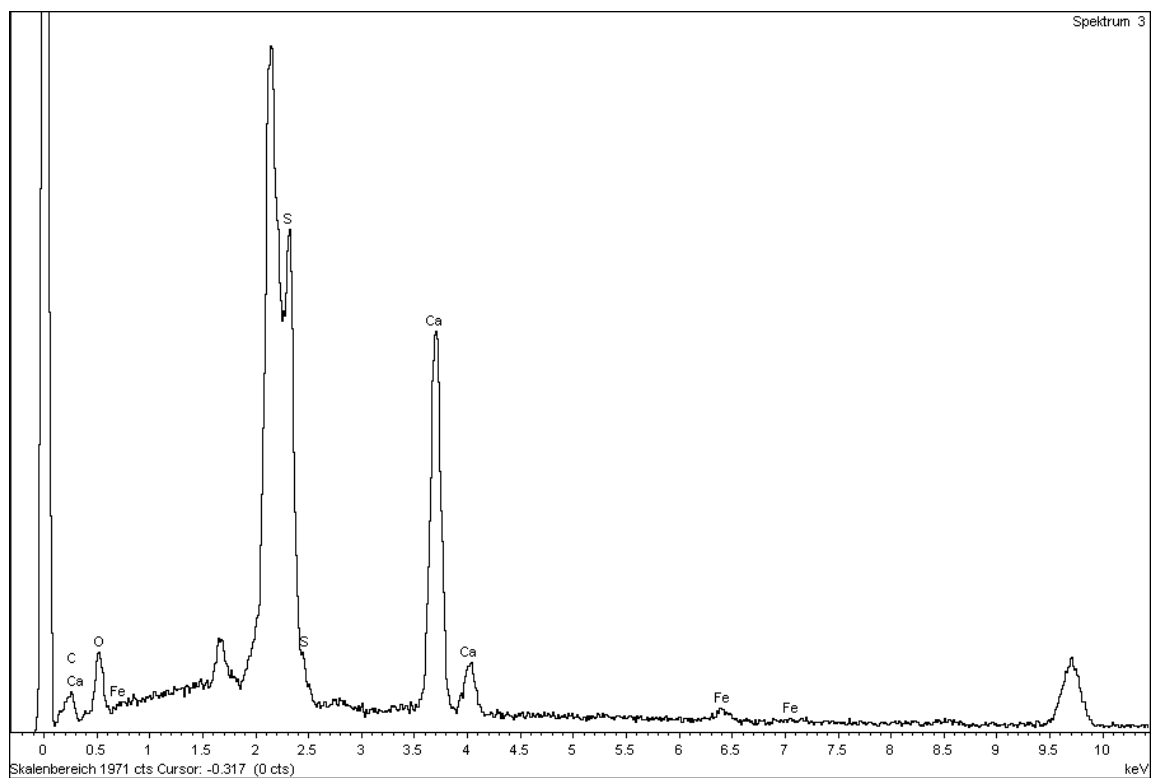
Fig. 6.47: EDX chemical analysis of gypsum/anhydrite, sample AT 35.
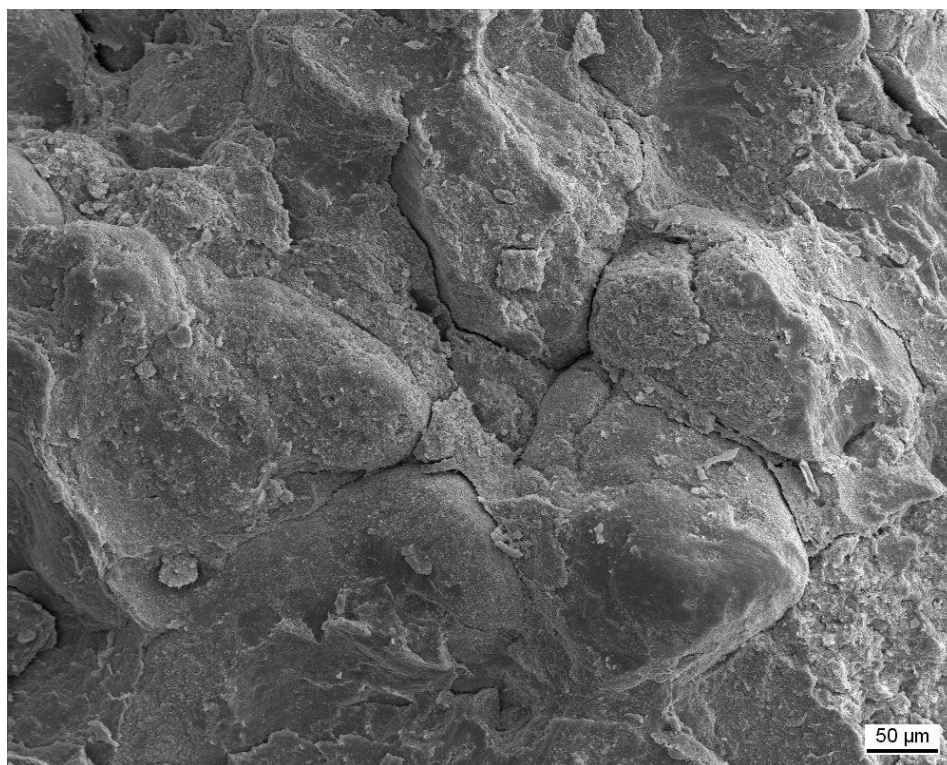
Fig. 6.48: Glauconite grains in a clayey matrix, sample mine.
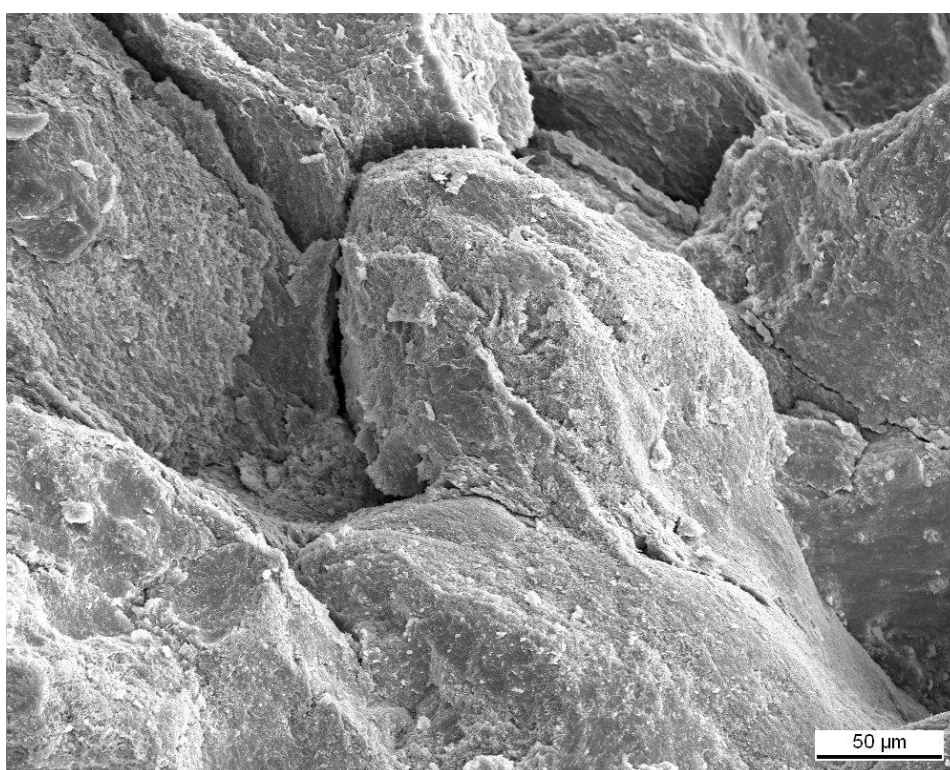
Fig. 6.49: Clayey matrix covers glauconite grains, sample mine.
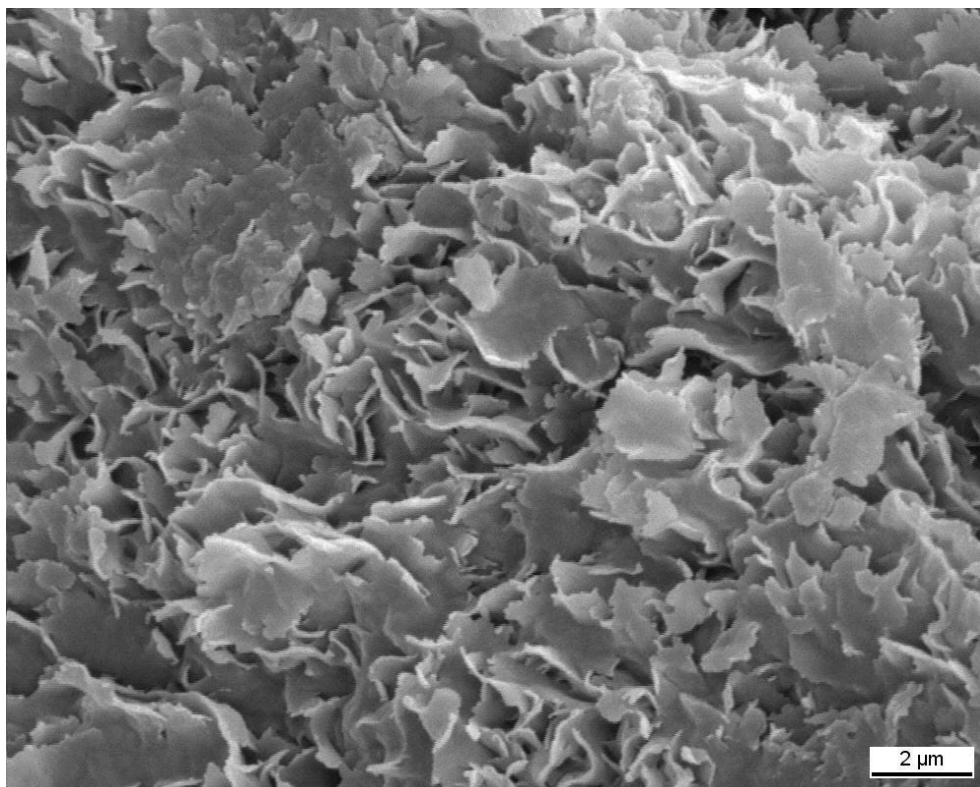
Fig. 6.50: SEM image showing the automorphic (rosette) habit of a illite/smectite mixed-layer of a glauconite grain, sample mine.

7. Discussion

7.1. Interpretation and comparison of glauconites (layer 16 - mine)

7.1.1. Chemical and mineralogical variations within layer 16

The glauconite grains of samples AT 31 to AT 36 vary in color and in their chemical composition (see chapter 6.3.).
AT 31 to AT 33 show light green to dark green and yellowish glauconite grains. The glauconite grains of samples AT 34 to AT 36 are greenish to brownish in color.

The amount of Al in glauconite decreases from the top to the base and shows a progressive substitution of Fe for octahedral Al. The content of Fe atoms decreases from an average of 1.13 Fe atoms in glauconite grains of sample AT 31 to an average of 0.63 Fe atoms in sample AT 36. The contents of Al in octahedral sites increases from an average of 0.51 Al atoms in sample AT 31 to an average of 0.64 Al atoms in sample AT 36.

K and Fe contents increase within layer 16 from the the top (AT 36) to the base (AT 31). In contrast, sulfur decreases from the top (AT 36) to the base (AT 31) within layer 16. The downward increase of K and Fe in the glauconite grains within the layer can be interpreted to have been caused by percolating waters, which leached ions only at the top of the layer. An exact interpretation for the higher sulfur content at the top of the layer is impossible, but might be explained by longer residence time at the sediment-water interface resulting in increased pyrite precipitation. Percolating waters lead to a breakdown of pyrite, Fe-ions were leached out and S was incorporated into the glauconite grains

The positive correlation between K_2O and Fe_2O_3 and the high contents of aluminimum indicate the diagenetic deformation of illite-smectite clay minerals and the evolving character of Fe_2O_3 which was incorporated with the K_2O in the smectite structure of glauconite (Bornhold and Giresse, 1985; Rundberg, 1989 & Amorosi, 1997). The positive correlation between K_2O and Fe_2O_3 of the weathered glauconite grains has to be considered from the opposite direction.

The presence of pyrite on the glauconite surface indicates that at times the glauconite was subjected to a reducing micro-environment. Pyrite is present in the surface

samples, but not in the un-altered mine sample. Giresse and Wiewióra (2001) suggest that formation of pyrite begins when easily reduced Fe species are available for sulfidation. The Fe is incorporated either in the silicate or the sulfide phases (Meunier & El Albani, 2007). Gaudin et al. (2005) have shown that framboidal pyrite is formed first in such microenvironments. The silicate phase cannot incorporate iron when sulfide is present; it forms when the sulfide is oxidized.

Gypsum and anhydrite form as a result of surface alteration. Sulfur is incorporated in the gypsum/anhydrite-crystals because of pyrite leaching. The secondary minerals gypsum and anhydrite in the surface samples are an indicator of weathering. The presence of Fe-oxides, hydroxides (AT 31) and jarosite (AT 32, AT 36) also indicates weathering processes.

Thin-section analyses show that the external boundaries of the glauconite become fuzzy and a greenish alteroplasma forms. The latter becomes increasingly red as weathering intensifies.

7.1.2. Comparison surface – subsurface glauconite

Glauconite is one of the most sensitive indicators of low sedimentation rates in marine environments (El-Hassan & Tichy, 2000). The maturity of glauconite predominantly reflects the time of residence of the green grains at the sea bed before burial (Odin & Matter, 1981). The morphology of the glauconitic grains is a good indicator for their maturity (ref). The alteration of the glauconite grains at surface prevents an exact determination of their maturity. The morphology and the K content of the surface grains do not correlate. Grains showing a morphology which would indicate an evolved stage (Odin & Matter, 1981), contain less K than expected for this stage of evolution. This can be interpreted as clear weathering effect. The fresh mine sample was not affected by weathering, so the evolution stage indicated by grain morphology and the potassium content show a good correlation. In general, the glauconite grains of the mine sample show an evolved stage of evolution. This gives an estimated time of duration of evolution of about 10^4 to 10^5 years for the mine sample (based on comparison with Odin & Matter, 1981).

The glauconite grains of the mine sample have a more intensive color compared to the surface samples. The grains of the mine sample are light to dark green in color. Surface samples AT 31 to AT 36 show greenish, yellowish to brownish glauconite grains.

Under the microscope, in plane polarized light, different shades of green are observed ranging from pale green, yellowish and brownish to dark green. The yellowish to brownish glauconite grains of samples AT 31 to AT 36 indicate weathering, while the intense green colors of the mine sample represents fresh, unweathered grains.

Macroscopically, the mine sample is finer-grained than the surface samples. The grains of the mine sample are more compacted and show a preferred orientation. In addition the mine sample contains less matrix than the surface samples. The grains of the subsurface sample contain less color-zonated grains than the ones of the outcrop.

X-ray diffraction demonstrates that the unweathered mine sample consists of illite (glauconite)/ smectite mixed-layer minerals richer in illite layers (80%) than the surface samples AT 31 to AT 36 (52%). Electron microprobe analyses show, that the fresh mine sample contains higher amounts of K and Fe than weathered samples. Potassium is leached out from the rock by percolating waters while the Fe leaves the phyllosilicates to precipitate as an independent Fe-phase (oxyhydroxides) (Meunier, 2004). The escape of K from the crystal lattice leads to the formation of smectite.

Investigations of glauconite grains with the scanning electron microscope at high magnifications reveal that the grains have different habits, like cracked habits, and that the grain surfaces show typical structures of illite(glauconite)/smectite mixed-layers. Odin & Matter, 1981 describe these structures as boxwork and rosette structures of evolved glauconite, which do not show any traces of the initial substrate.

Because of their morphology, their mineralogy and the sedimentary environment the glauconites can be interpreted to be autochthonous. Amorosi (1997) suggested that the autochthonous glauconite is generally concentrated within comparatively thin (less than 1- 3m) deposits. The glaucony of Abu Tartur occurs as granular facies.

Glauconitization also had an influence on the chemical evolution of the formation water because K, Fe and some Mg were extracted from the pore water and/or the surrounding sediments and Al was added as glauconitization progressed (Lee et al., 2002). Iron is the key element in the glauconitization process. It is supplied to the sea by rivers as detrital iron and by volcanic processes as true juvenile iron (Odin & Matter, 1981).

Meunier (2004) described the weathering of glauconite as a progressive transformation into illite/smectite mixed-layers and eventually into smectites.

The data from thin-section analyses, electron microprobe analyses and X-ray diffraction show strong evidence that the weathering sequence is opposite to that of the sediment glauconitization (Hower, 1961; Velde, 1976).

The formation of glauconite is thus a reversible process at earth surface conditions (Meunier, 2004).

7.2. Depositional environment

During the Late Cretaceous, Egypt was located near the palaeo-equator and experienced warm, wet and tropical to subtropical conditions characterized by low seasonality contrasts and predominately chemical weathering. A shallow sea covered the Western Desert of Egypt (Tantawy et al., 2001).

A predictive depositional model for the Campanian- Maastrichtian deposits of the Duwi Formation in Abu Tartur will be discussed in the following:

Two depositional environments can be interpreted based on sedimentary architecture and structures

 1) a deeper-water hemipelagic environment, where phosphorites and organic carbon-rich shales were deposited and

2) a shallower, prograding higher energy shelf environment with glauconite.

From a sequence stratigraphic perspective:

1) was deposited during the transgressive systems tract and the early highstand systems tract while

2) was deposited during the remaining highstand systems tract and a lowstand prograding wedge (Glenn & Arthur, 1990)

Principally, deposition is controlled by the rate of change of relative sea level.

The formation of glauconite is controlled by the availability of Fe and K and the balance between detrital influx and winnowing. Its high variabilty is a result of the replacement of mineralogically different initial substrates by authigenic minerals.,A semi-confined microenvironment within a physical substrate is necessary for the formation of glauconite (Odin & Matter, 1981).
Both, phosphate and glauconite require slightly reducing conditions and decomposition of organic matter. Slow deposition of phosphate and glauconite in condensed sections is common and is often associated with sea level rise (Compton, 1989). Phosphate pellets and nodules are both syn- and post-glauconite formation.

The phosphorites of Egypt were deposited during the transgression of the Tethyan Sea, and form a 100 -150 km wide belt stretching from the Red Sea in the east into the Western Desert (Ahmed & Kurzweil, 2002).

Supersaturation of pore waters with P and Ca is necessary for the formation of phosphorite. The analyzed phosphorite shows contents of 32.11% P_2O_5 and 50.31% CaO. P is rare in the oceanic environment with an average of only 70 ppm in both, organic and inorganic forms. Surface water is further depleted of inorganic P by phytoplankton activity (Phillip, 1986). P-enriched waters are mainly introduced to the shelf and slope through upwelling, this increases the concentration of P in surface waters and, as a result, phytoplankton activity. P is incorporated into the sediment through the introduction of phytoplankton remains, which through decomposition result in the accumulation and concentration of inorganic phosphate in oxygen-poor sediments. Summarising, phosphate accumulations predominately occur in areas of upwelling currents. Today they are often located along the western margins of continents. The optimum water depth for phosphate formation is from 30 – 200 m (Phillip, 1986; Parrish et al., 2001; Coles et al., 2002).

But upwelling is not necessarily the only source of P in shallow marine settings.A fluvial source for P has been reported in literature (Glenn & Arthur, 1990). Evidence from a variety of sources suggests that the continental hinterland to the south in Egypt and possibly much of North Africa was deeply weathered and that the region during late Campanian – Maastrichtian times was humid and supplied abundant fluvial input to the basin (Glenn & Arthur, 1990).

Three possible mechanisms for P inputs are known from literature: 1) an upwelling regime (Phillip, 1986), 2) skeletal material (phosphatized or primary fish debris and 3) fluvial input to the basin (Glenn & Arthur, 1990).

The second possibility is strongly suggested as the main mechanism for the phosphorites of Abu Tartur because of an enrichment of fish bones in a phosphorite layer.

8. Conclusions

Glauconite and phosphorite bearing Upper Cretaceous sediments of the Abu Tartur Plateau, Egypt, have been studied to get information about the facies and mechanisms of glauconite formation. The sediments represent a sediment starved heterogenous sequence of shallow-marine epicontinental deposits.

By combining sedimentological data two main depositional environments can be interpreted:

(1) a deep-water hemipelagic environment accompanying maximum transgression and
(2) a shallower higher energy shelf environment.

Deposition of the studied profile ATM is controlled by a long-term transgressive phase and several higher order sea-level fluctuations.

XRD analyses of the clay fraction of the six outcrop samples and the subsurface mine sample show that the grains consist of ordered and randomly interstratified illite (glauconite)/smectite mixed-layers, with more illite layers (80 %) in the mine sample.
The charge distribution diagram muscovite-pyrophyllite-celadonite shows a clear trend from smectitic glauconite to illitic glauconite, the mine sample plots exactly in the field for glauconite.
Surface samples are too weathered for an exact determination of maturity. The morphology and the K content of the mine sample indicate an evolved stage of glauconite evolution.
All these features show that the surface samples are strongly altered by weathering and that glauconite progressively transforms into iron-rich illte/smectite mixed layers and then into smectites.
For any valid chemical and mineralogical characterization of glauconite at surface, these weathering effects have to be taken into consideration.

Acknowledgments

References

AHMED, E. A. & KURZWEIL, J. (2002): Sedimentological, mineralogical and geochemical characteristics of Upper Cretaceous Egyptian phosphorites with special reference to the microbial role in phosphogenesis. Aspects of Cretaceous Stratigraphy and Paleobiogeography, Band 15, 11-34, Wien (Österreichischen Akademie der Wissenschaften).

AMOROSI, A. (1995): Glauconite and sequence stratigraphy: a conceptual framework of distribution in siliciclastic sequences. Journal of Sedimentary Research B65, 419-425.

AMOROSI, A. (1997): Detecting Compositional, Spatial and Temporal Attributes of Glauconite: a Tool for Provenance Research, Sedim. Geol., 109, 135-153.

AWAD, G. H. & GHOBRIAL, M. G. (1965): Zonal stratigraphy of the Kharga Oasis: Cairo, Egypt Geol. Survey Paper, 34, 77p.

BAUDIN, F. (1995): Depositional controls on Mesozoic source rocks in the Tethys. In: Huc, A.-Y. (Ed.), Paleogeography, Paleoclimate, and Source Rocks. AAPG Studies in Geology, 40, 191-211.

BORNHOLD, B. D. & GIRESSE, P. (1985): Glauconitic Sediments on the Continental Shelf of Vancouver Island, British Columbia, Canada J. Sediment. Petrol, 55, 653-664.

BRINDLEY, G. W. & BROWN, G. (1980): Crystal structures of clay minerals and their X-ray identification. Mineralogical society, London.

BURST, J. F. (1958a): „Glauconite pellets": their mineral nature and applications to stratigraphic interpretations. Bull. Am. Ass. Petrol. Geol, 42, 310-337.

BURST, J. F. (1958b): Mineral heterogeneity in glauconite pellets. Am. Mineral, 43, 481-497.

CAYEUX, L. (1916): Indruduction à létude pétrograhique des roches sédimentaires. (Glauconie, pp. 241-252). Imprimerie Nationale, Paris, 524pp.

CHAMLEY, H. (1989): Ferriferous Clay Granules and Facies. 213-234, Clay Sedimentology, Berlin (Springer).

COLES, S. K. P., WRIGHT, C. I. SINCLAIR, D. A. & VAN DEN BOSSCHE, P. (2002): The potential for environmentally sound development of marine deposits of potassic and phosphatic minerals offshore, Southern Africa. Marine Georesources & Geotechnology, 20, 2, 87-110.

COMPTON, M. S. (1989): Morphology and geochemistry of glauconite from the Te Kuiti Group, South Auckland region, New Zealand. Unpublished MSc Thesis, University of Waikato.

CONDIE, K. G. (1975): Plate tectonics and crustal evolution. New York, Pergamon, 346p.

EHLMANN, A., HULINGS, N. & GLOVER, E. (1963): Stages of glauconite formation in modern foraminiferal sediments. J. Sedim. Petrol, 33, 87-96.

EL-HASSAN, M. A. & TICHY, G. (2000): Geochemistry and Origin of Glauconite of the El-Gedida Mines and Baharya Formation (Early Cenomanian), Baharya Oasis, Western Desert, Egypt. Geochemistry International, Vol. 38, No. 4, 374-387.

GAUDIN, A., BUATIER, M. D., BEAUFORT, D., PETIT, S., GRAUBY, O. and DECARREAU, A. (2005): Characterization and origin of Fe3+-montmorillonite in deep-water calcareous sediments (Pacific Ocean, Costa Rica margin). Clay Mineral., 53, 452-465.

GEPTNER, A. R. & IVANOVSKAYA, T. A. (1998): Biochemogenic genesis of the glauconite – nontronite series minerals in present-day sediments of the Pacific Ocean. Lithology and Mineral Recources, 33, 6, 503-517.

GEPTNER, A. R. & IVANOVSKAYA, T. A. (2000): Glauconite from lower cretaceous marine terrigenous rocks of England: A concept of biochemogenic origin. Lithology and Mineral Resources, 35, 5, 434-444.

GEPTNER, A. R., IVANOVSKAYA, T. A. & USHATINSKAYA, G. T. (1994): Biochemical origin of layered silicates with a glauconite-illite composition (Cambrien of north Verkhayan'e). Lithology and Mineral Resources, 29, 1, 64-74.

GIRESSE, P., LAMBOY, M. & ODIN, G. S. (1980): Evolution géométrique des supports de glauconitisation; application à la reconstitution du paléoenvironement. Oceanol. Acta, 3, 251-260.

GIRESSE, P. & WIEWIÓRA, A. (2001): Stratigraphic condensed deposition and diagenetic evolution of green clay minerals in deep water sediments on the Ivory Coast – Ghana Ridge. Marine Geology, 179, 51-70.

GLENN, C. R. & ARTHUR, M. A. (1990): Anatomy and origin of a Cretaceous phosphorites-greensand giant, Egypt. Sedimentology, 37, 123-154.

HASSAN, M. A. & EL-SHALL, H. (2004): Glauconitic clay of El Gidida, Egypt: evaluation and surface modification. Applied Clay Science, 27, 219-222.

HENDRIKS, F., LUGER, P., KALLENBACH, H. & SCHROEDER, J. H. (1984): Stratigraphical and sedimentological framework of the Kharga-Sinn El-Kaddab stretch (western and southern part of the Nile Basin), Western Desert, Egypt. Berliner geowiss. Abh. (A), 50, 117-151.

HERMINA, M. H. (1967): Geology of the northwestern approaches of Kharga: Cairo, Egypt Geol. Survey Paper 44, 88p.

HERMINA, M. H., GHOBRIAL, M. G. & ISSAWI, B. (1961): The geology of the Dakhla area: Cairo, Egypt Geol. Survey Mineral Resources Dept., 33p.

HOWER, J. (1961): Some factors concerning the nature and the origin of glauconite. Am. Mine, 46, 313-334.

IRELAND, B. J., CURTIS, C. D. & WHITEMAN, J. A. (1983): Compositional variation within some glauconites and illites and implications for their stability and origins. Sedimentology, 30, 769-786.

ISSAWI, B. (1972): Review of Upper Cretaceous-Lower Tertiary Stratigraphy in Central and Southern Egypt. The American Association of Petroleum Geologists Bulletin, 56, 8, 1448-1463.

KLEMME, H. D. (1958): Regional geology of circum-Mediterranean region: Am. Assoc. Petroleum Geologists Bull., 42, 477-512.

KLITZSCH, E. (1986): Plate tectonics and cantonal geology in Northeast Africa (Egypt, Sudan). Geologische Rundschau 75, 3, 755-768.

KLITZSCH, E., HARMS, J. C., LEJAL-NICOL, A. & LIST, F. K. (1979): Major subdivisions and depositional environments of Nubia strata, southwestern Egypt. Bull. Am. Ass. Petrol. Geol., 63, 967-974.

KÖSTER, H. M. (1977): Die Berechnung kristallchemischer Strukturformeln von 2:1-Schichtsilikaten unter der Berücksichtigung der gemessenen Zwischenschichtladungen und Kationenumtauschkapazitäten, sowie die Darstellung der Ladungsverteilung in der Struktur mittels Dreieckskoordinaten. Clay Minerals, 12, 45.

LE PICHON, X., FRANCHETEAU, J. & BONNIN, J. (1976): Plate tectonics. New York, Elsevier, 241p.

LEE, C. H., CHOI, S.-W. & SUH, M. (2002): High iron glauconite from the continental shelf of the Yellow Sea off the southwestern Korean Peninsula. Journal of Asian Earth Sciences, 20, 507-515.

LÜNING, S., KOLONIC, S., BELHADJ, E. M., BELHADJ, Z., COTA, L., Baric, G., & WAGNER, T. (2004): Integrated depositional model for the Cenomanian-Turonian organic-rich strata in North Africa. Earth-Science Reviews, 64, 51-117.

MANSOUR, H. H. & KHALLAF, A. F. (1979): Application of textural characteristics for depositional environment interpretation of the Upper Cretaceous-Paleocene east of Idfu-Sibaiya, Nile Valley. Ann. Geol. Surv. Egypt, 9, 471-497.

MANSOUR, H. H., YOUSSEF, M. M. & EL YOUNSI, A. R. (1979): Petrology and sedimentology of the Upper Cretaceous, Paleocene succession northwest of Kharga Oasis, Egypt. Ann. Geol. Surv. Egypt, 9, 471-497.

MARSHALL, C. E. (1949): The structural interpretation of chemical analyses of the clay minerals. In: The colloid chemistry of the silicate minerals. New York: Academic Press, 159p.

MARSHALL-NEILLA, G. & RUFFELL, A. (2004): Authigenic phosphate nodules (Late Cretaceous, Northern Ireland) as condensed succession microarchives Cretaceous Research, 25, 439-452.

MEUNIER, A. (2004): Clays. 83- 327, Berlin (Springer).

MEUNIER, A. & EL ALBANI, A. (2007): The glauconite - Fe-illite - Fe-smectite problem: a critical review. Terra Nova, 19, 95-104.

MILLOT, G. (1964): Géologie des argiles. Masson Publ., Paris, 499pp.

NAKKADY, S. E. (1951): Stratigraphical study of the Mahamid district: Cairo, Egypt, Alexandria Univ. Faculty Sci. Bull., 1, 17-43.

NOTHOLT, A. J. G. (1985): Phosphorite resources in the Mediterranean (Tethyan) Phosphogenetic Province: A progress report. Sci Géol. Mém., 77, 9-21.

ODIN, G. S. (1975): De glauconiarum: Constitutione, origine, aetateque. Thèse d'Etat, Université Pierre et Marie Curie, Paris.

ODIN, G. S. (1988): Green Marine Clays. 22 - 441, Oxford (Elsevier).

ODIN, G. S. & FULLAGAR, P. D. (1988): Geological significance of the glauconite facies. In Odin, G. S. Green Marine Clays. 295-332, Amsterdam (Elsevier).

ODIN, G. S. & LÉTOLLE, R. (1980): Glauconitization and phosphatization environments: A tentative comparison. In Y. K. Bentor (Edit.). Marine Phosphorites. Soc. Econ. Pal. Min. Spec. Publ., 29, 227-237.

ODIN, G. S. & MATTER, A. (1981): De glauconiarum origine. Sedimentology, 28, 611-641.

OYARZUN, R., DOBLAS, M., LÓPEZ-RUIZ, J. & CEBRIÁ, J. M. (1997): Opening of the central Atlantic and asymmetric mantle upwelling phenomena: implications for long-lived magmatism in western North Africa and Europe. Geology, 25, 727-730.

PARRISH, J. T., DROSER, M. L. & BOTTJER, D. J. (2001): A Triassic upwelling zone: The Shublik formation, Arctic Alaska, USA. Journal of Sedimentary Research, Vol. 71, No.2, 272-285.

PHILLIP, D. M. (1986): Continental slope dredging from the southern flank of the Hokianga Terrace, West Coast, North Island, New Zealand. Unpublished MSc Thesis, University of Auckland.

PORRENGA, D. H. (1967): Glauconite and chamosite as depth indicators in the marine environment. Mar. Geol., 5, 495-501.

ROBINSON, V. D. & ENGEL, M. H. (1993): Characterization of the source horizons within the late cretaceous transgressiv sequence of Egypt. AAPG Studies in Geology, 37, 101-117.

RUNDBERG, Y. (1989): Tertiary Sedimentary History and Basin Evolution of the Norwegian North Sea between 60 and 62N an Integrated Approach, Unpublished Ph. D. Thesis, Unic. Trondheim, Norway.

SAID, R. (1962): The Geology of Egypt. Amsterdam-New York (Elsevier).

SCHLANGER, S. O. & JENKYNS, H. C. (1976): Cretaceous oceanic anoxic events-causes and consequences. Geol. Mijnbouw, 55, 179-184.

SCHRANK, E. (1984): Organic-geochemical and palynological studies of a Dakhla Shale profile (Upper Cretaceous) in Southeast-Egypt, Part A: Succession of microfloras and depositional environment. – Berliner geowiss. Abh. A 50, 189-207.

SEDIEK, K. N. & AMER, A. M. (2001): Sedimentological and technological studies of Abu Tartur Black Shales, Western Desert, Egypt. Physicochemical Problems of Mineral Processing, 35, 141-152.

SMITH, A. G., Hurley, A. M. & Briden, J. C. (1982): Paläokontinentale Weltkarten des Phanerozoikums, Stuttgart, F. Enke Verlag, 102p.

SOLIMAN, M. A., HABIB, M. E. & AHMED, E. A. (1986): Sedimentologic and tectonic evolution of the Upper Cretaceous-Lower Tertiary succession at Wadi Qena, Egypt. Sediment. Geol., 46, 111-133.

STRICKLER, M. E. & FERRELL Jr., R. E. (1990): Fe substitution for Al in glauconite with increasing diagenesis in the First Wilcox sandstone (lower Eocene), Livingston Parish, Louisiana. Clays Clay Miner. 38, 69-76.

TANTAWY, A. A., KELLER, G., ADATTE, T., STINNESBECK, W., KASSAB A. & SCHULTE P. (2001): Maastrichtian to Paleocene depositional environment of the Dakhla Formation, Western Desert, Egypt: sedimentology, mineralogy, and integrated micro- and macrofossil biostratigraphies. Cretaceous Research, 22, 795-827.

THOMPSON, G. R. & HOWER, J. (1975): The mineralogy of glauconite. Clays Clay Miner. 23, 289-300.

TRIPLEHORN, D. M. (1966): Morphology, internal structure and origin of glauconite pellets. Sedimentology, 6, 247-266.

TRIPLEHORN, D. M. (1967): Morphology, internal structure and origin of glauconite pellets, A Reply. Sedimentology, 8, 169-171.

VAN HOUTEN, F. B., BHATTACHARYYA, D. P. & MANSOUR, S. E. I. (1984): Cretaceous Nubia Formation and correlative deposits, eastern Egypt: Major regressive-transgressive complex. Bull. Geol. Soc. Am., 95, 397-405.

VELDE, B. (1976): The chemical evolution of glauconite pellets as seen by microprobe determinations. Mineralogical Magazine and Journal of the Mineralogical Society, 40, 315, 753-760.

WARD, W. C. & MCDONALD, K. C. (1979): Nubia Formation of central eastern Desert, Egypt-Major subdivisions and depositional setting. Bull. Am. Ass. Petrol. Geol., 63, 975-983.

WASSEF, A. S. (1977): On the results of geological investigations and ore reserves calculations of Abu Tartur phosphorite deposits. Ann. geol. Surv. Egypt, 9, 1-60.

WEAVER, C. E. & POLLARD, L. D. (1973): The chemistry of clay minerals. Elsevier, Amsterdam 213pp.

Appendix

(Fig. 6.51 – 6.56: XRD-diffractograms, Tab. 6.4: Electron microprobe data and calculations)
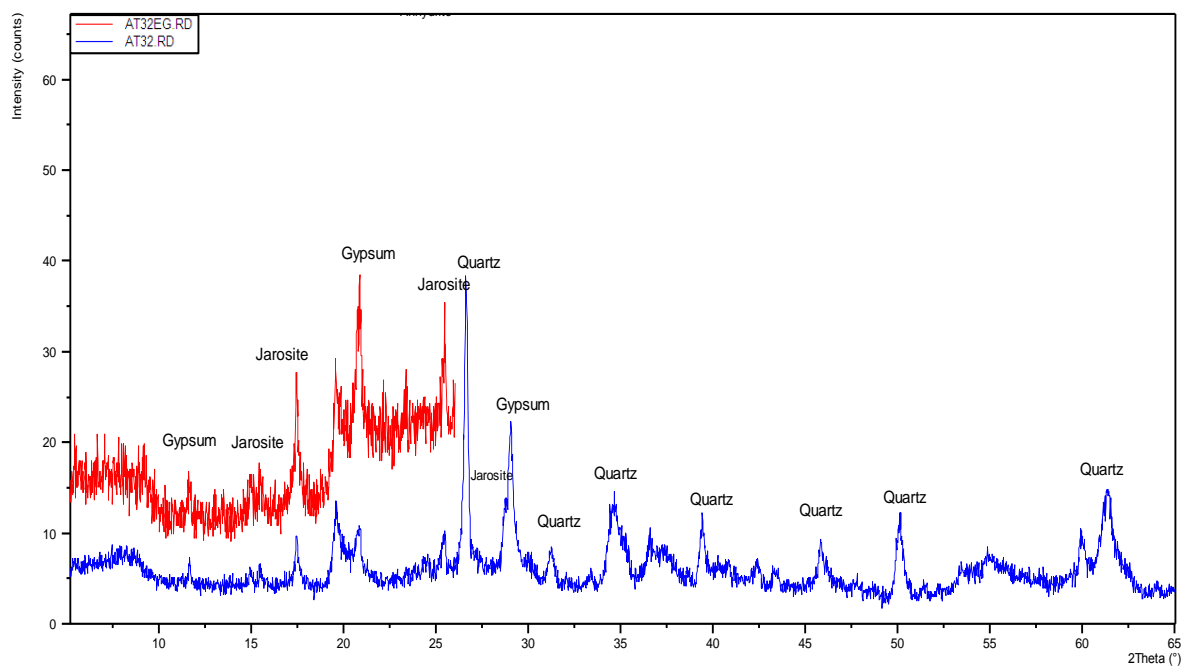
Fig. 6.51: X-ray diffraction patterns of bulk sample AT 32. Sample is un-saturated and saturated with ethylenglycol (EG).
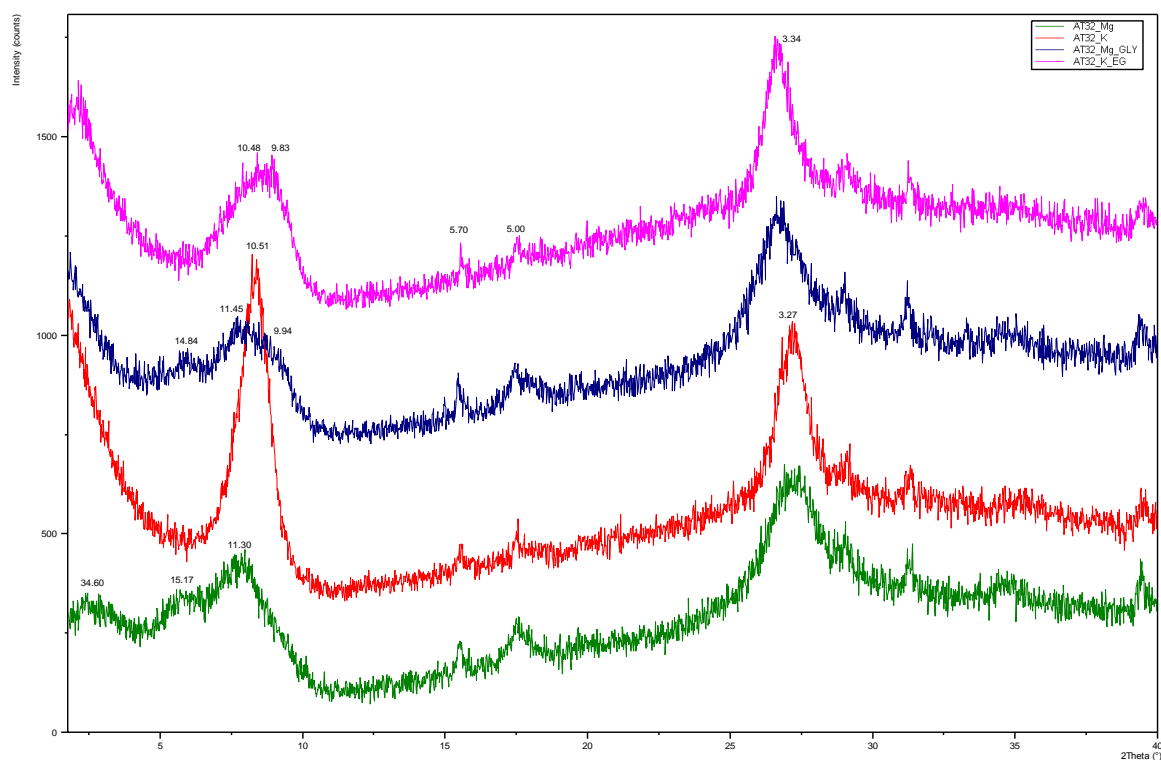
Fig. 6.52: X-ray diffraction patterns of the clay fraction of sample AT 32. Sample is saturated with magnesium (Mg), magnesium plus glycerol (Mg_GLY), potassium (K) and potassium plus ethylenglycol (K_EG); inserted values are d-spacings in Å.
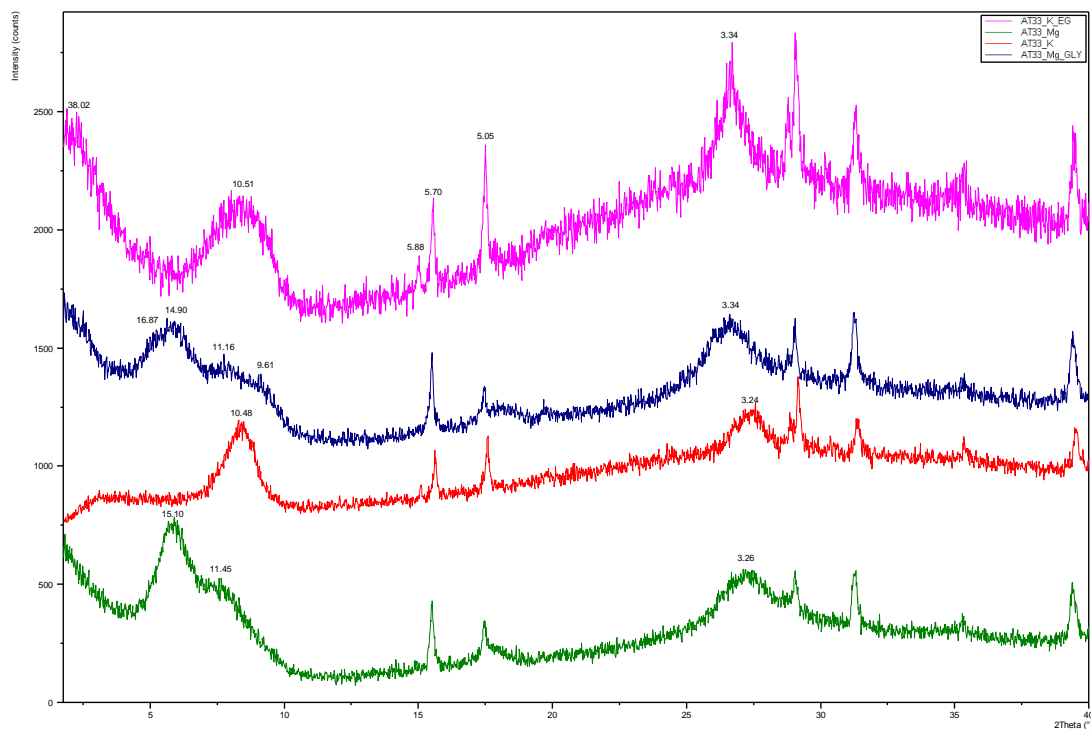
Fig. 6.53: X-ray diffraction patterns of the clay fraction of sample AT 33. Sample is saturated with magnesium (Mg), magnesium plus glycerol (Mg_GLY), potassium (K) and potassium plus ethylenglycol (K_EG); inserted values are d-spacings in Å.
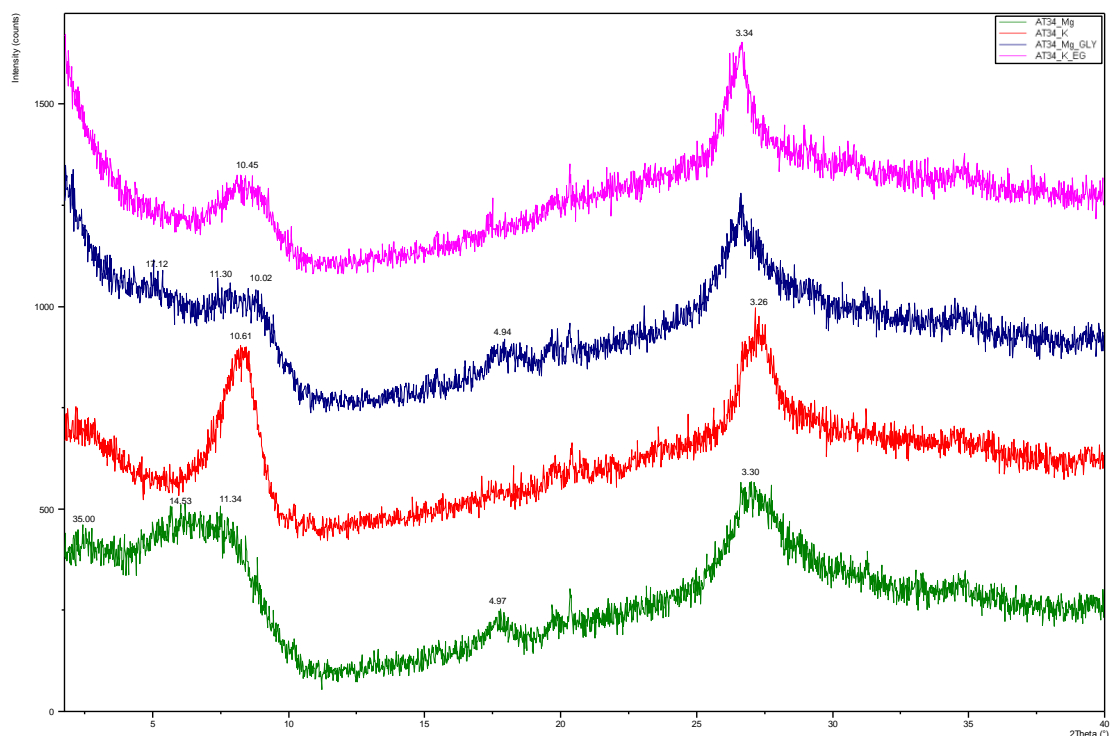
Fig. 6.54: X-ray diffraction patterns of the clay fraction of sample AT 34. Sample is saturated with magnesium (Mg), magnesium plus glycerol (Mg_GLY), potassium (K) and potassium plus ethylenglycol (K_EG); inserted values are d-spacings in Å.
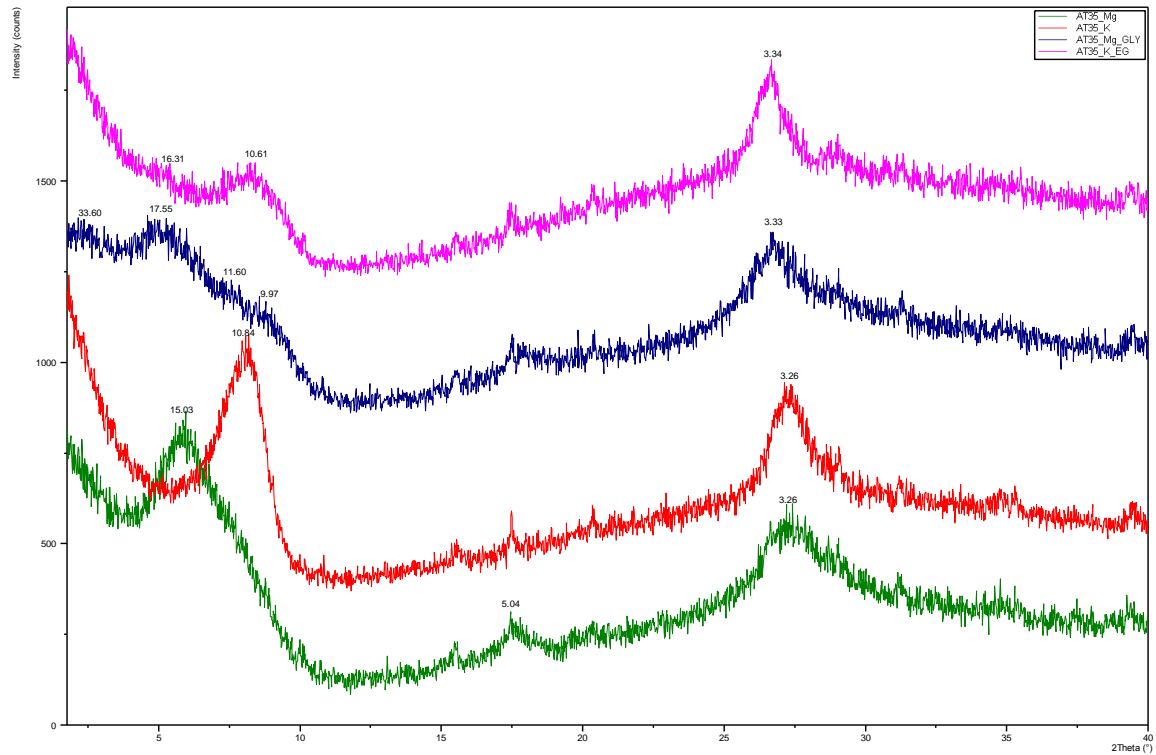
Fig. 6.55: X-ray diffraction patterns of the clay fraction of sample AT 35. Sample is saturated with magnesium (Mg), magnesium plus glycerol (Mg_GLY), potassium (K) and potassium plus ethylenglycol (K_EG); inserted values are d-spacings in Å.
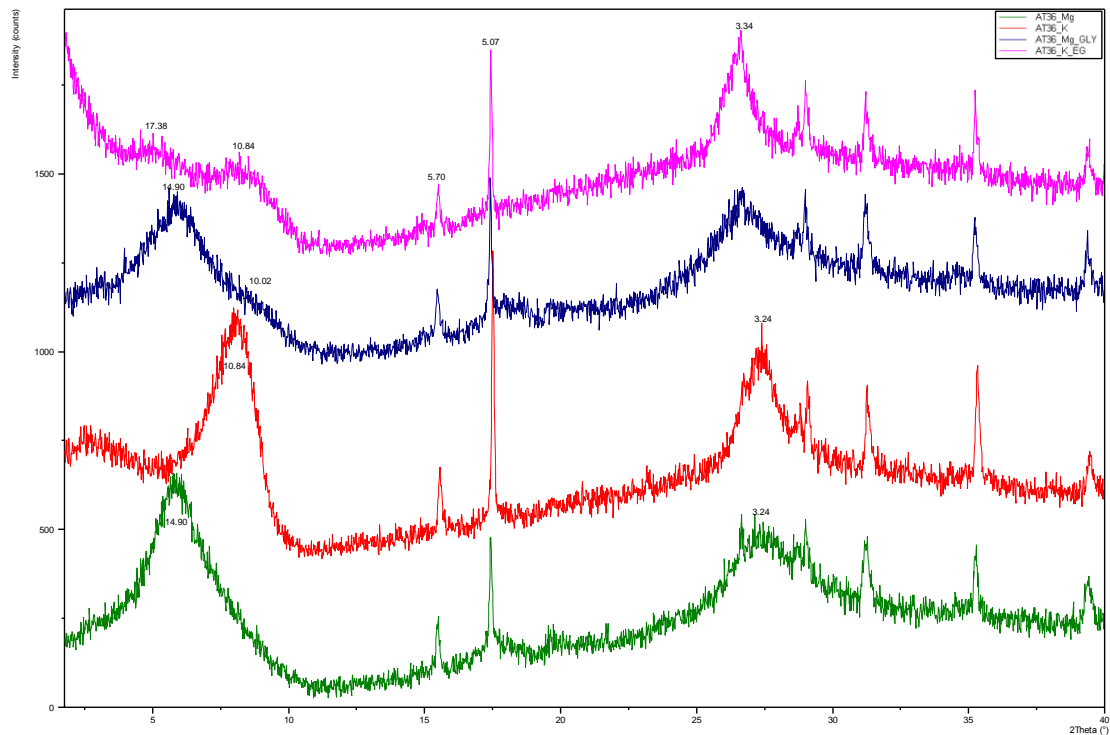
Fig. 6.56: X-ray diffraction patterns of the clay fraction of sample AT 36. Sample is saturated with magnesium (Mg), magnesium plus glycerol (Mg_GLY), potassium (K) and potassium plus ethylenglycol (K_EG); inserted values are d-spacings in Å.

Tab. 6.4: Electron microprobe data from respective seven glauconite grains of samples AT 31 to AT 36

Representative chemical composition (wt%) and structural formulae of glauconite AT 31 from the Abu Tartur mine.

	AT 31 core 1	AT 31 outer rim 1	AT 31 core 2	AT 31 outer rim 2	AT 31 core 3	AT 31 outer rim 3	AT 31 core 4	AT 31 outer rim 4	AT 31 core 5	AT 31 outer rim 5	AT 31 core 6	AT 31 outer rim 6	AT 31 core 7	AT 31 outer rim 7
SiO_2	49.761	49.451	51.505	51.293	50.481	50.208	50.903	51.056	52.049	51.577	48.152	48.685	52.647	52.591
Al_2O_3	8.125	9.026	9.215	10.494	8.759	9.982	7.040	7.185	10.339	11.691	7.337	7.403	9.020	9.344
Fe_2O_3	21.097	21.483	19.386	18.877	20.380	20.224	21.961	21.605	18.294	18.065	24.280	24.207	17.881	17.777
MnO	0.002	0.019	0.006	0.028	0.017	0.008	0.013	0.031	0.039	0.017	0.013	0.024	0.006	0.006
MgO	3.330	3.377	3.702	3.718	3.377	3.405	3.490	3.500	3.614	3.581	3.374	3.414	3.293	3.294
CaO	0.048	0.069	0.110	0.127	0.110	0.111	0.122	0.066	0.159	0.190	0.061	0.128	0.202	0.194
Na_2O	0.016	0.028	0.027	0.041	0.036	0.033	0.030	0.018	0.045	0.031	0.022	0.018	0.033	0.033
K_2O	5.932	5.594	5.950	5.328	5.989	5.919	6.550	6.507	5.335	4.443	6.914	6.233	5.480	5.610
TiO_2	0.040	0.023	0.025	0.056	0.042	0.035	0.039	0.031	0.016	0.037	0.053	0.035	0.043	0.026
SO_2	0.524	0.833	0.674	0.761	0.447	0.513	0.526	0.454	0.452	0.647	0.762	0.805	0.350	0.451
P_2O_5	0.527	0.630	0.407	0.497	0.436	0.563	0.378	0.352	0.421	0.565	0.674	0.666	0.296	0.291
Total	89.400	90.533	91.008	91.222	90.074	90.273	91.052	90.804	90.763	90.844	90.922	91.617	89.248	89.615

Structural formulae based on $O_{10}(OH)_2$

Tetrahedal

Si	3.736	3.680	3.761	3.722	3.740	3.684	3.768	3.777	3.765	3.717	3.622	3.643	3.859	3.844
Al	0.264	0.320	0.239	0.278	0.260	0.316	0.232	0.223	0.235	0.283	0.378	0.357	0.141	0.156
charge	-0.264	-0.320	-0.239	-0.278	-0.260	-0.316	-0.232	-0.223	-0.235	-0.283	-0.378	-0.357	-0.141	-0.156

Octahedral

Al	0.455	0.472	0.554	0.619	0.505	0.547	0.382	0.403	0.646	0.710	0.273	0.296	0.638	0.649
Fe^{3+}	1.192	1.203	1.065	1.031	1.136	1.117	1.223	1.203	0.996	0.980	1.375	1.363	0.986	0.978
Mg	0.373	0.375	0.403	0.402	0.373	0.372	0.385	0.386	0.390	0.385	0.378	0.381	0.360	0.359
charge	-0.313	-0.225	-0.337	-0.246	-0.331	-0.264	-0.415	-0.410	-0.294	-0.160	-0.300	-0.261	-0.408	-0.401

Interlayer

K	0.568	0.531	0.554	0.493	0.566	0.554	0.619	0.614	0.492	0.408	0.664	0.595	0.512	0.523
Na	0.002	0.004	0.004	0.006	0.005	0.005	0.004	0.003	0.006	0.004	0.003	0.003	0.005	0.005
Ca	0.004	0.006	0.009	0.010	0.009	0.009	0.010	0.005	0.012	0.015	0.005	0.010	0.016	0.015
charge	0.578	0.547	0.576	0.519	0.589	0.577	0.643	0.627	0.522	0.442	0.677	0.618	0.549	0.558

Representative chemical composition (wt%) and structural formulae of glauconite AT 32 from the Abu Tartur mine.

	AT 32 core 1	AT 32 outer rim 1	AT 32 core 2	AT 32 outer rim 2	AT 32 core 3	AT 32 outer rim 3	AT 32 core 4	AT 32 outer rim 4	AT 32 core 5	AT 32 outer rim 5	AT 32 core 6	AT 32 outer rim 6	AT 32 core 7	AT 32 outer rim 7
SiO_2	51.288	50.369	49.355	49.723	51.171	49.800	48.544	48.315	51.134	50.323	50.936	51.028	50.600	50.451
Al_2O_3	7.544	7.792	7.575	8.352	7.915	7.860	7.904	8.214	8.580	9.174	7.832	8.769	7.885	7.773
Fe_2O_3	19.685	18.803	19.268	18.151	19.096	18.258	18.825	18.287	19.538	18.284	19.402	18.054	19.271	19.469
MnO	0.010	0.014	0.029	0.018	0.015	0.019	0.012	0.020	0.011	0.015	0.011	0.011	0.007	0.000
MgO	3.556	3.652	3.473	3.533	3.398	3.293	3.517	3.533	3.368	3.429	3.476	3.456	3.283	3.343
CaO	0.191	0.168	0.147	0.158	0.130	0.092	0.113	0.126	0.064	0.153	0.078	0.087	0.074	0.055
Na_2O	0.006	0.020	0.020	0.013	0.007	0.013	0.011	0.023	0.006	0.009	0.040	0.018	0.025	0.038
K_2O	5.565	5.493	5.881	5.739	5.563	5.317	5.859	5.688	5.969	5.518	6.204	5.740	6.304	6.302
TiO_2	0.045	0.049	0.051	0.036	0.032	0.045	0.092	0.051	0.048	0.063	0.035	0.038	0.031	0.031
SO_2	0.546	0.457	0.343	0.346	0.495	0.401	0.633	0.796	0.521	0.534	0.882	0.817	0.949	1.134
P_2O_5	0.363	0.382	0.423	0.414	0.384	0.357	0.533	0.557	0.410	0.469	0.385	0.409	0.385	0.410
Total	88.813	89.002	88.813	89.002	88.813	89.002	88.813	89.002	88.813	89.002	88.813	89.002	88.813	89.002

Structural formulae based on $O_{10}(OH)_2$

Tetrahedal

Si	3.833	3.824	3.797	3.803	3.838	3.843	3.776	3.773	3.790	3.783	3.814	3.822	3.815	3.808
Al	0.167	0.176	0.203	0.197	0.162	0.157	0.224	0.227	0.210	0.217	0.186	0.178	0.185	0.192
charge	-0.167	-0.176	-0.203	-0.197	-0.162	-0.157	-0.224	-0.227	-0.210	-0.217	-0.186	-0.178	-0.185	-0.192

Octahedral

Al	0.497	0.521	0.484	0.556	0.538	0.558	0.501	0.529	0.540	0.596	0.505	0.596	0.516	0.500
Fe^{3+}	1.107	1.074	1.116	1.045	1.078	1.060	1.102	1.075	1.090	1.034	1.093	1.018	1.093	1.106
Mg	0.376	0.413	0.398	0.403	0.380	0.379	0.408	0.411	0.372	0.384	0.388	0.386	0.369	0.376
charge	-0.436	-0.389	-0.404	-0.391	-0.392	-0.388	-0.375	-0.366	-0.366	-0.342	-0.430	-0.386	-0.435	-0.430

Interlayer

K	0.607	0.532	0.577	0.560	0.532	0.523	0.581	0.567	0.564	0.529	0.593	0.548	0.606	0.607
Na	0.005	0.003	0.003	0.002	0.001	0.002	0.002	0.003	0.001	0.001	0.006	0.003	0.004	0.005
Ca	0.004	0.014	0.012	0.013	0.010	0.008	0.009	0.011	0.005	0.012	0.006	0.007	0.006	0.004
charge	0.621	0.563	0.604	0.588	0.553	0.541	0.601	0.592	0.575	0.554	0.611	0.565	0.622	0.620

Representative chemical composition (wt%) and structural formulae of glauconite AT 33 from the Abu Tartur mine.

	AT 33 core 1	AT 33 outer rim 1	AT 33 core 2	AT 33 outer rim 2	AT 33 core 3	AT 33 outer rim 3	AT 33 core 4	AT 33 outer rim 4	AT 33 core 5	AT 33 outer rim 5	AT 33 core 6	AT 33 outer rim 6	AT 33 core 7	AT 33 outer rim 7
SiO_2	50.632	50.848	51.624	53.213	51.328	54.315	53.335	55.148	50.964	52.030	52.272	51.638	52.327	52.505
Al_2O_3	6.764	6.585	7.968	8.126	7.964	8.503	8.332	8.610	6.914	7.189	8.282	9.045	7.961	8.355
Fe_2O_3	19.819	18.831	16.842	17.729	17.218	18.011	16.493	16.906	19.124	19.744	18.290	16.351	18.706	18.516
MnO	0.010	0.017	0.010	0.012	0.001	0.007	0.007	0.006	0.005	0.003	0.009	0.013	0.008	0.004
MgO	3.218	2.928	3.114	3.326	2.979	3.181	2.747	2.750	3.292	3.396	3.379	3.218	3.436	3.475
CaO	0.127	0.189	0.202	0.120	0.169	0.080	0.138	0.095	0.191	0.093	0.148	0.194	0.169	0.083
Na_2O	0.028	0.018	0.022	0.008	0.016	0.015	0.014	0.022	0.016	0.024	0.011	0.013	0.021	0.029
K_2O	6.311	5.618	5.344	5.652	5.245	5.751	5.018	5.310	5.767	6.212	6.033	5.381	6.556	6.447
TiO_2	0.043	0.038	0.031	0.036	0.039	0.062	0.038	0.053	0.049	0.039	0.054	0.034	0.048	0.050
SO_2	1.105	0.325	0.346	1.205	0.265	0.670	0.355	0.891	0.466	1.396	1.007	0.355	0.700	1.089
P_2O_5	0.389	0.402	0.428	0.465	0.394	0.391	0.416	0.440	0.377	0.389	0.426	0.402	0.356	0.373
Total	88.444	85.798	85.930	89.892	85.619	90.986	86.891	90.231	87.166	90.515	89.910	86.645	90.288	90.927

Structural formulae based on $O_{10}(OH)_2$

Tetrahedal

Si	3.852	3.918	3.926	3.915	3.917	3.918	3.978	3.985	3.878	3.862	3.862	3.886	3.854	3.848
Al	0.148	0.082	0.074	0.085	0.083	0.082	0.022	0.015	0.122	0.138	0.138	0.114	0.146	0.152
charge	-0.148	-0.082	-0.074	-0.085	-0.083	-0.082	-0.022	-0.015	-0.122	-0.138	-0.138	-0.114	-0.146	-0.152

Octahedral

Al	0.458	0.516	0.640	0.620	0.633	0.641	0.710	0.718	0.498	0.491	0.583	0.688	0.545	0.570
Fe^{3+}	1.135	1.092	0.964	0.982	0.989	0.978	0.926	0.919	1.095	1.103	1.017	0.926	1.037	1.021
Mg	0.365	0.336	0.353	0.365	0.339	0.342	0.305	0.296	0.373	0.376	0.372	0.361	0.377	0.380
charge	-0.491	-0.504	-0.482	-0.464	-0.456	-0.459	-0.482	-0.497	-0.475	-0.466	-0.456	-0.436	-0.500	-0.467

Interlayer

K	0.613	0.552	0.519	0.530	0.511	0.529	0.477	0.490	0.560	0.588	0.569	0.517	0.616	0.603
Na	0.004	0.003	0.003	0.001	0.002	0.002	0.002	0.003	0.002	0.003	0.002	0.002	0.003	0.004
Ca	0.010	0.016	0.016	0.009	0.014	0.006	0.011	0.007	0.016	0.007	0.012	0.016	0.013	0.006
charge	0.637	0.587	0.554	0.549	0.541	0.543	0.501	0.507	0.594	0.605	0.595	0.551	0.645	0.619

Representative chemical composition (wt%) and structural formulae of glauconite AT 34 from the Abu Tartur mine.

	AT 34 core 1	AT 34 outer rim 1	AT 34 core 2	AT 34 outer rim 2	AT 34 core 3	AT 34 outer rim 3	AT 34 core 4	AT 34 outer rim 4	AT 34 core 5	AT 34 outer rim 5	AT 34 core 6	AT 34 outer rim 6	AT 34 core 7	AT 34 outer rim 7
SiO_2	52.382	51.644	54.970	53.614	53.517	54.670	52.579	54.428	52.135	54.419	54.203	55.538	61.922	62.808
Al_2O_3	7.611	9.184	10.071	9.059	6.369	6.190	7.161	5.955	6.503	7.839	7.402	8.457	5.575	6.734
Fe_2O_3	15.038	14.014	14.359	13.975	16.599	16.150	16.713	15.853	15.913	16.160	14.415	14.324	10.044	11.082
MnO	0.012	0.015	0.011	0.005	0.021	0.021	0.017	0.012	0.023	0.014	0.002	0.008	0.020	0.018
MgO	2.903	3.136	3.033	2.892	3.619	3.391	3.477	2.764	3.043	3.554	2.811	3.424	2.114	2.812
CaO	0.306	0.312	0.212	0.308	0.036	0.021	0.047	0.287	0.208	0.049	0.223	0.020	0.154	0.045
Na_2O	0.010	0.014	0.014	0.021	0.013	0.028	0.010	0.018	0.021	0.018	0.021	0.006	0.019	0.012
K_2O	4.564	4.093	4.256	4.183	4.954	4.878	5.228	4.881	4.773	4.920	4.182	4.211	2.851	3.186
TiO_2	0.046	0.029	0.044	0.042	0.041	0.038	0.028	0.040	0.025	0.033	0.040	0.037	0.032	0.059
SO_2	0.148	0.230	0.318	0.441	2.728	2.743	2.075	0.185	0.294	1.866	0.421	2.630	0.263	1.720
P_2O_5	0.273	0.262	0.308	0.286	0.306	0.334	0.260	0.245	0.262	0.292	0.287	0.295	0.263	0.295
Total	83.294	82.933	87.593	84.824	88.201	88.461	87.593	84.665	83.200	89.163	84.007	88.950	83.256	88.770

Structural formulae based on $O_{10}(OH)_2$

Tetrahedal

Si	4.036	3.973	3.993	4.030	4.402	4.098	3.981	4.133	4.051	4.005	4.115	4.072	4.535	4.419
Al		0.027	0.007				0.019							
charge	0.144	-0.027	-0.007	0.120	1.608	0.392	-0.019	0.532	0.204	0.020	0.460	0.288	2.140	1.676

Octahedral

Al	0.691	0.806	0.855	0.802	0.567	0.547	0.620	0.533	0.596	0.680	0.662	0.731	0.481	0.558
Fe^{3+}	0.872	0.811	0.784	0.790	0.943	0.911	0.952	0.906	0.930	0.895	0.824	0.790	0.553	0.587
Mg	0.333	0.360	0.328	0.324	0.407	0.379	0.392	0.313	0.352	0.390	0.318	0.374	0.231	0.295
charge	-0.645	-0.429	-0.427	-0.576	-0.656	-0.868	-0.500	-1.057	-0.718	-0.495	-0.906	-0.689	-2.436	-1.975

Interlayer

K	0.449	0.402	0.394	0.401	0.477	0.466	0.505	0.473	0.473	0.462	0.405	0.394	0.266	0.286
Na	0.002	0.002	0.002	0.003	0.002	0.004	0.001	0.003	0.003	0.003	0.003	0.001	0.003	0.002
Ca	0.025	0.026	0.017	0.025	0.003	0.002	0.004	0.023	0.017	0.004	0.018	0.002	0.012	0.003
charge	0.501	0.456	0.430	0.454	0.485	0.474	0.514	0.522	0.510	0.473	0.444	0.399	0.293	0.294

Representative chemical composition (wt%) and structural formulae of glauconite AT 35 from the Abu Tartur mine.

	AT 35 core 1	AT 35 outer rim 1	AT 35 core 2	AT 35 outer rim 2	AT 35 core 3	AT 35 outer rim 3	AT 35 core 4	AT 35 outer rim 4	AT 35 core 5	AT 35 outer rim 5	AT 35 core 6	AT 35 outer rim 6	AT 35 core 7	AT 35 outer rim 7
SiO_2	55.285	54.374	51.959	51.805	54.303	53.235	52.716	53.004	54.421	53.842	56.129	56.245	54.457	55.816
Al_2O_3	6.818	5.958	7.051	6.262	7.926	6.575	7.972	7.783	7.282	6.237	5.618	5.581	6.708	6.758
Fe_2O_3	12.997	13.297	15.732	16.134	14.432	14.793	16.344	16.682	14.464	14.470	13.009	12.983	14.562	15.450
MnO	0.011	0.017	0.009	0.014	0.007	0.011	0.010	0.010	0.008	0.006	0.014	0.024	0.019	0.024
MgO	2.968	2.604	3.388	3.247	3.199	2.999	3.516	3.516	3.054	2.711	2.735	2.936	3.484	3.546
CaO	0.037	0.035	0.051	0.043	0.075	0.046	0.048	0.040	0.063	0.041	0.039	0.022	0.024	0.045
Na_2O	0.009	0.017	0.022	0.037	0.017	0.009	0.014	0.017	0.009	0.015	0.023	0.020	0.015	0.014
K_2O	3.900	3.910	4.875	4.805	4.218	4.332	5.063	5.209	4.224	4.221	3.719	3.748	4.073	4.307
TiO_2	0.052	0.034	0.042	0.045	0.031	0.031	0.048	0.032	0.026	0.033	0.038	0.055	0.032	0.027
SO_2	1.007	0.419	0.830	0.435	0.724	0.386	1.437	1.149	1.133	0.425	0.760	1.161	1.656	2.139
P_2O_5	0.315	0.281	0.314	0.313	0.345	0.240	0.303	0.311	0.240	0.236	0.272	0.291	0.281	0.496
Total	83.399	80.945	84.272	83.139	85.276	82.656	87.470	87.750	84.922	82.236	82.355	83.064	85.310	88.621

Structural formulae based on $O_{10}(OH)_2$

Tetrahedal

Si	4.215	4.250	4.014	4.045	4.078	4.121	3.958	3.960	4.118	4.176	4.306	4.301	4.130	4.117
Al							0.042	0.040						
charge	0.860	1.000	0.056	0.180	0.312	0.484	-0.042	-0.040	0.472	0.704	1.224	1.204	0.520	0.468

Octahedral

Al	0.613	0.549	0.642	0.576	0.702	0.600	0.663	0.645	0.649	0.570	0.508	0.503	0.600	0.587
Fe^{3+}	0.746	0.782	0.915	0.948	0.816	0.862	0.923	0.938	0.824	0.844	0.751	0.747	0.831	0.858
Mg	0.337	0.303	0.390	0.378	0.358	0.346	0.393	0.392	0.344	0.313	0.313	0.335	0.394	0.390
charge	-1.249	-1.401	-0.549	-0.672	-0.730	-0.922	-0.456	-0.467	-0.893	-1.132	-1.597	-1.580	-0.919	-0.885

Interlayer

K	0.379	0.390	0.480	0.479	0.404	0.428	0.485	0.497	0.408	0.418	0.364	0.366	0.394	0.405
Na	0.001	0.003	0.003	0.006	0.002	0.001	0.002	0.002	0.001	0.002	0.003	0.003	0.002	0.002
Ca	0.003	0.003	0.004	0.004	0.006	0.004	0.004	0.003	0.005	0.003	0.003	0.002	0.002	0.004
charge	0.386	0.399	0.491	0.493	0.418	0.437	0.495	0.505	0.419	0.426	0.373	0.373	0.400	0.415

Representative chemical composition (wt%) and structural formulae of glauconite AT 36 from the Abu Tartur mine.

	AT 36 core 1	AT 36 outer rim 1	AT 36 core 2	AT 36 outer rim 2	AT 36 core 3	AT 36 outer rim 3	AT 36 core 4	AT 36 outer rim 4	AT 36 core 5	AT 36 outer rim 5	AT 36 core 6	AT 36 outer rim 6	AT 36 core 7	AT 36 outer rim 7
SiO_2	54.767	56.134	53.892	55.413	57.544	57.636	52.571	51.141	63.374	64.662	56.969	56.946	62.345	59.070
Al_2O_3	7.461	6.891	8.465	7.838	7.457	6.715	7.518	6.775	8.842	8.183	6.713	6.816	6.847	7.328
Fe_2O_3	12.237	10.973	15.857	14.754	12.028	11.175	17.517	16.759	6.105	6.263	8.819	8.759	7.226	7.587
MnO	0.010	0.015	0.026	0.012	0.009	0.024	0.010	0.013	0.011	0.000	0.001	0.011	0.020	0.006
MgO	2.983	2.824	3.720	3.396	3.069	3.057	3.569	3.555	2.386	1.914	2.320	2.335	2.275	2.674
CaO	0.057	0.021	0.045	0.029	0.020	0.039	0.143	0.046	0.184	0.270	0.012	0.021	0.032	0.022
Na_2O	0.021	0.018	0.023	0.024	0.019	0.016	0.016	0.006	0.006	0.011	0.012	0.020	0.008	0.006
K_2O	3.812	3.396	4.432	4.092	3.762	3.567	5.100	4.753	1.567	1.704	2.620	2.722	2.150	2.326
TiO_2	0.043	0.031	0.035	0.029	0.055	0.049	0.041	0.031	0.085	0.042	0.078	0.042	0.034	0.031
SO_2	2.861	1.318	2.047	1.828	2.860	3.064	1.465	1.403	1.394	0.582	1.162	0.848	1.739	1.633
P_2O_5	0.276	0.289	0.282	0.297	0.312	0.266	0.301	0.278	0.279	0.274	0.347	0.358	0.225	0.259
Total	84.527	81.908	88.821	87.712	87.134	85.607	88.252	84.760	84.232	83.901	79.052	78.875	82.900	80.941

Structural formulae based on $O_{10}(OH)_2$

Tetrahedal

Si	4.194	4.310	3.976	4.089	4.252	4.323	3.935	3.974	4.526	4.586	4.447	4.440	4.579	4.476
Al			0.024				0.065	0.026						
charge	0.776	1.240	-0.024	0.356	1.008	1.292	-0.065	-0.026	2.104	2.344	1.788	1.760	2.316	1.904

Octahedral

Al	0.674	0.624	0.712	0.682	0.649	0.594	0.598	0.594	0.744	0.684	0.618	0.626	0.593	0.654
Fe^{3+}	0.706	0.634	0.880	0.819	0.669	0.631	0.987	0.980	0.328	0.334	0.518	0.514	0.399	0.433
Mg	0.341	0.323	0.409	0.374	0.338	0.342	0.398	0.412	0.254	0.202	0.270	0.271	0.249	0.302
charge	-1.178	-1.580	-0.406	-0.749	-1.370	-1.641	-0.449	-0.454	-2.276	-2.542	-2.052	-2.038	-2.526	-2.135

Interlayer

K	0.373	0.333	0.417	0.385	0.355	0.341	0.487	0.471	0.143	0.154	0.261	0.271	0.201	0.225
Na	0.003	0.003	0.003	0.003	0.003	0.002	0.002	0.001	0.001	0.001	0.002	0.003	0.001	0.001
Ca	0.005	0.002	0.004	0.002	0.002	0.003	0.011	0.004	0.014	0.020	0.001	0.002	0.002	0.002
charge	0.386	0.340	0.428	0.392	0.362	0.349	0.511	0.480	0.172	0.195	0.265	0.278	0.206	0.230

Representaive chemical composition (wt%) and structural formulae of glauconite mine from the Abu Tartur mine.

	mine core 1	mine outer rim 1	mine core 2	mine outer rim 2	mine core 3	mine outer rim 3	mine core 4	mine outer rim 4	mine core 5	mine outer rim 5	mine core 6	mine outer rim 6	mine core 7	mine outer rim 7	mine core 8	mine outer rim 8
SiO2	52,391	51,649	53,072	51,167	52,943	51,486	53,000	52,908	49,023	48,305	53,961	49,560	53,255	51,519	52,725	50,049
Al2O3	6,343	6,405	6,902	6,824	6,598	7,003	8,078	8,007	7,050	7,203	7,630	7,180	7,303	7,429	7,892	7,859
Fe2O3	22,108	21,403	21,370	20,266	21,385	19,513	20,154	19,930	17,563	16,589	19,653	17,408	20,611	19,616	19,223	17,295
MnO	0,020	0,027	0,002	0,012	0,017	0,009	0,003	0,001	0,001	0,000	0,008	0,006	0,009	0,015	0,011	0,006
MgO	3,059	3,080	3,029	2,923	3,182	3,139	3,133	3,166	3,052	3,044	3,195	2,893	2,957	2,853	3,089	2,978
CaO	0,397	1,732	0,404	0,455	0,349	0,415	0,432	0,412	0,487	0,513	0,351	0,418	0,479	0,443	0,519	0,668
Na2O	0,034	0,039	0,042	0,017	0,032	0,031	0,030	0,029	0,039	0,047	0,053	0,045	0,037	0,042	0,055	0,037
K2O	7,242	6,969	6,797	6,388	7,194	6,692	6,511	6,593	6,193	6,004	6,750	5,896	6,494	6,298	6,017	5,362
TiO2	0,048	0,074	0,046	0,037	0,030	0,034	0,047	0,079	0,043	0,048	0,037	0,038	0,057	0,043	0,039	0,036
SO2	0,040	0,101	0,047	0,030	0,045	0,024	0,064	0,044	0,045	0,060	0,054	0,036	0,130	0,047	0,069	0,049
P2O5	0,056	0,409	0,044	0,037	0,033	0,029	0,053	0,043	0,024	0,028	0,021	0,029	0,040	0,025	0,044	0,042
Total	91,737	91,886	91,755	88,154	91,807	88,373	91,504	91,211	83,519	81,838	91,712	83,508	91,371	88,327	89,682	84,380

Structural formulae based on $O_{10}(OH)_2$

Tetrahedal

Si	3.827	3.794	3.846	3.849	3.846	3.858	3.827	3.832	3.869	3.878	3.877	3.893	3.859	3.852	3.862	3.874
Al	0.173	0.206	0.154	0.151	0.154	0.142	0.173	0.168	0.131	0.122	0.123	0.107	0.141	0.148	0.138	0.126
charge	-0.173	-0.206	-0.154	-0.151	-0.154	-0.142	-0.173	-0.168	-0.131	-0.122	0.123	-0.107	0.141	-0.148	-0.138	-0.126

Octahedral

Al	0.373	0.349	0.435	0.454	0.411	0.476	0.514	0.516	0.525	0.559	0.523	0.558	0.483	0.507	0.543	0.591
Fe^{3+}	1.215	1.183	1.165	1.147	1.169	1.100	1.095	1.086	1.043	1.002	1.063	1.029	1.124	1.104	1.060	1.007
Mg	0.333	0.337	0.327	0.328	0.345	0.351	0.337	0.342	0.359	0.364	0.342	0.339	0.319	0.318	0.337	0.344
charge	-0.570	-0.730	-0.546	-0.541	-0.570	-0.570	-0.499	-0.510	-0.578	-0.589	0.558	-0.561	0.541	-0.531	-0.517	-0.518

Interlayer

K	0.675	0.653	0.628	0.613	0.667	0.640	0.600	0.609	0.623	0.615	0.619	0.591	0.600	0.601	0.562	0.529
Na	0.005	0.006	0.006	0.002	0.004	0.005	0.004	0.004	0.006	0.007	0.007	0.007	0.005	0.006	0.008	0.005
Ca	0.031	0.136	0.031	0.037	0.027	0.033	0.033	0.032	0.041	0.044	0.027	0.035	0.037	0.035	0.041	0.055
charge	0.742	0.931	0.696	0.689	0.725	0.711	0.670	0.677	0.711	0.710	0.680	0.668	0.679	0.677	0.652	0.644

Curriculum vitae

Persönliche Daten

Name: Brigitte Pestitschek
Geburtsdatum und -ort: 1. November 1985 in Wien
Staatsangehörigkeit: Österreich
Religion: römisch- katholisch
Wohnsitz: Sillerstraße 126, 2231 Strasshof an der Nordbahn
Telefonnr.:   0676 7637650
E-mail: brigitte_1985@yahoo.de

Schulausbildung

1996- 2004:   BRG Gänserndorf
2004:   Reifeprüfung am BRG Gänserndorf

Studium

Oktober 2004:   Beginn des Studiums der Erdwissenschaften an der
                                      Universität Wien
2008:   Abschluss des Bakkalaureatsstudiums mit Auszeichnung
                                      und Beginn des Masterstudiums Erdwissenschaften

Berufserfahrungen

Juli 2003:   Ferialpraktikum Alpine Mayreder Bau GmbH
Sept. 2004:   Ferialpraktikum Anker Snack & Coffee GmbH
Juli 2007:   Ferialpraktikum TPA (Technische Prüfanstalt) Gesellschaft
                                      für Qualitätssicherung und Innovation GmbH
Sept. 2007:   Ferialpraktikum im Geologischen Labor der OMV
                                      Exploration & Production
seit Feb. 2008:   Geringfügig beschäftigt TPA
SS 08 – WS 08/09:   Studienassistentin Universität Wien

Weitere Qualifikationen

Sprachen: Englisch
                                      Französisch, Grundkenntnisse
EDV: MS-Office (Word, Excel etc.)